Skin-friction Drag Reduction by Hairy Surfaces in Turbulent Channel Flow

by

Jae Bok Lee

A dissertation submitted in partial fulfillment
of the requirements for the degree of
Doctor of Philosophy
(Mechanical Engineering)
in The University of Michigan
2023

Doctoral Committee:

Associate Professor Jesse Capecelatro, Co-chair
Associate Professor Eric Johnsen, Co-chair
Professor Krzysztof Fidkowski
Assistant Professor Aaron Towne

Jae Bok (Samuel) Lee
jaebok@umich.edu
ORCID iD: 0000-0002-9113-1633

DEDICATION

To my family.

ACKNOWLEDGMENTS

I sincerely express my gratitude and appreciation to the members of my dissertation committee: Professor Jesse Capecelatro, Professor Eric Johnsen, Professor Aaron Towne, and Professor Krzysztof Fidkowski. Their exceptional teaching in various classes has provided invaluable learning experiences, and their guidance, and insightful suggestions have been pivotal in shaping the content and direction of my dissertation thesis.

I am also thankful to Professor Rayhaneh Akhavan for supervising my research with valuable comments. I would like to express my heartfelt thanks to the dedicated professionals at the Mechanical Engineering Academic Services Offices (ME-ASO), the Michigan Engineering C.A.R.E. Center, the Rackham Resolution Office for their unwavering support and encouragement to get through academic dispute I experienced. Their assistance was instrumental in helping me navigate through the challenges and reach a resolution.

I would also like to express my gratitude to the members of the Korean Presbyterian Church in Ann Arbor, who have been an unwavering source of encouragement for me and my family in all circumstances. I would also like to express sincere appreciation to all my colleagues and friends at the University of Michigan, Sandia National Labs, KAIST, and Hanyang University for their continuous support and valuable feedback on my work. I am grateful for the many enjoyable and informal conversations we have shared over the years. Special thanks to Yifeng, Donghyun, Amirreza for the fruitful discussions and enjoyable time.

I would like to express my sincere gratitude to my family, Hak Soo Lee, Young Sook Han, Jinah Lee, Jungwon Choi, Grace Kim, Tae Hee Kim for their endless support and encouragement. Their presence in my life has been an immense source of strength and motivation. Lastly, I dedicate this dissertation to my beloved wife, Yeojin Jeong. Her unyielding support and countless sacrifices have been the cornerstone of my journey, and I have no doubt that I would not be standing here today without her steadfast support and encouragement.

This study was supported by UMRCP Allocation, NSF XSEDE Allocation TG-CTS070067N, and M. R. Prince Foundation.

TABLE OF CONTENTS

CHAPTER

LIST OF FIGURES

FIGURE

LIST OF TABLES

TABLE

LIST OF ACRONYMS

LB Lattice-Boltzmann

IB Immersed boundary

LES Large-eddy simulation

DNS Direct numerical simulation

DR Drag reduction

MKE Mean kinetic energy

TKE Turbulent kinetic energy

FFT Fast-Fourier transform

ABSTRACT

One notable feature of wall-bounded turbulent flows is high skin-friction drag. Reducing the turbulent skin-friction drag on engineering surfaces such as oil pipelines, aircrafts, or ships, can lead to significant energy savings and reduction in carbon footprint. Hairy surfaces, inspired by seal fur surfaces and bird feathers, have emerged as a promising approach for skin-friction drag reduction. Despite their promise, no study has yet demonstrated the underlying mechanism of skin-friction drag reduction with hairy surfaces. In this study, turbulent skin-friction drag reduction with hairy surfaces and its physical mechanism were investigated by employing direct numerical simulation (DNS) in turbulent channel flow, with hairy surfaces, uniformly distributed on both channel walls. The simulations were conducted using a lattice Boltzmann, immersed boundary (LB-IB) method.

An improved reciprocal interpolation-spreading operations is proposed in order to satisfy the no-slip enforcement on the hairy filaments. The no-slip condition along the hairy filaments was measured by employing the ratio of the velocity of a Lagrangian marker along a hairy filament to the fluid velocity interpolated into that marker. If the ratio is the unity, the no-slip condition is strictly satisfied; in other words, the slip error is indicated by the deviation of this ratio from the unity. In comparison to the previous LB-IB methods that provided the slip error up to $O(1000)\%$, the present LB-IB method ensures better no-slip enforcement on the hairy filaments with the slip error less than $\sim 2\%$. Due to the improved reciprocity of the interpolation-spreading operations, the present LB-IB method successfully accomplishes better numerical accuracy, stability, and robustness compared to the previously suggested LB-IB methods.

A parametric study was performed at a bulk Reynolds number of 7200, corresponding to a friction Reynolds number of approximately 221 in a base turbulent channel flow with smooth, no-slip walls, for various filament parameters such as Cauchy number, filament height-to-spacing ratio, filament height, density ratio between the hairy filament and fluid. When drag reduction was plotted as functions of the individual filament parameters, it did not exhibit consistent trends with respect to each of the filament parameters. However, when plotted against the ratio of the characteristic time scale of the hairy filaments to the time scale of the largest eddies in the base turbulent channel flow, the magnitudes of drag reduction collapsed into a single curve. The maximum drag reduction of 5.4% was obtained at the characteristic time scale ratio of $1.4 - 1.5$.

Another significant achievement of this study is to reveal the underlying mechanism behind skin-friction drag reduction with hairy surfaces. The mechanism was investigated by examining the modulation of intercomponent/interscale energy transfer through budgets of Reynolds stresses, mean/turbulent kinetic energy budgets, and one-dimensional energy spectra. The mechanism can be attributed to the modulation of intercomponent and interscale energy transfer. Specifically, the presence of hairy filaments leads to a decrease in the pressure-strain correlation, which causes an accumulation of turbulence intensity in the streamwise component while reducing it in the cross-streamwise components. Consequently, the energy that would have been distributed from the streamwise component to the spanwise and wall-normal components is transported to wake scale turbulence by hairy filaments, and the transported energy is eventually dissipated within the viscous sublayer. This study is the first DNS research that demonstrates skin-friction drag reduction with hairy surfaces and reveals its underlying physical mechanism.

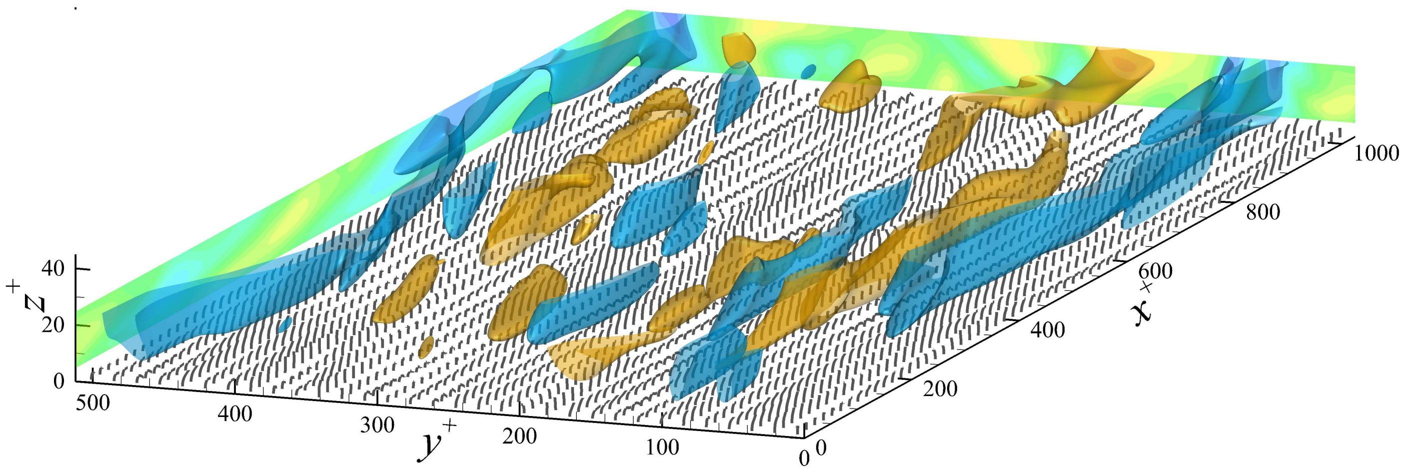

Isosurfaces of the streamwise velocity fluctuations (±4 in wall unit) over hairy surfaces.

CHAPTER 1

Introduction

1.1 Background

1.1.1 Wall-bounded Turbulence

Wall-bounded turbulence refers to the turbulent flow that occurs adjacent to solid surfaces, such as walls or boundaries. A notable feature of wall-bounded turbulence is high frictional drag, primarily generated due to the presence of strong mean shear originating from the no-slip wall. As a result, the flow exhibits distinct structures and patterns at different wall-normal distances from the wall as illustrated in figure 1.1. The dynamics of wall-bounded turbulence are characterized by two regions in the wall-normal direction, according to the relative importance of viscosity (Tennekes & Lumley, 1972): The inner layer and the outer layer. These two regions are further divided into several layers, as depicted in figure 1.2. Very near the wall, the viscous shear stress arising from the velocity gradient and fluid viscosity is important to the dynamics of the flow. The variables are adequately scaled with the friction velocity, $u_\tau \equiv \sqrt{\tau_w/\rho}$, where τ_w is the wall shear stress, ρ is the fluid density and the kinematic fluid viscosity, ν. The viscous-scaled variables are often indicated in wall units, which is denoted by a superscript $+$.

The region corresponding to the wall-normal location within $z^+ \lesssim 5$ is defined as the viscous sublayer, where viscous shear stress predominates over turbulent shear stress. Within the viscous sublayer, the mean velocity varies linearly with the wall-normal location $\bar{U}^+ = z^+$, which

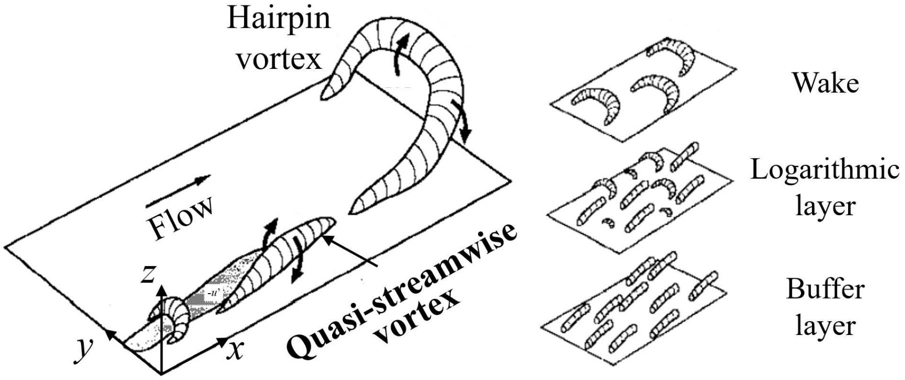

Figure 1.1: Robinson's summary of coherent structures in wall-bounded turbulence (Robinson, 1991).

is often called 'law of the wall'. The upper bar denotes time-averaging. Above the viscous sublayer, the buffer layer extends further away from the wall within $5 \lesssim z^+ \lesssim 30$. Within the buffer layer, both the Reynolds stresses and the viscous stresses are significant. The buffer layer is characterized by an increase in turbulence intensity and the emergence of coherent structures, which arise as a consequence of the self-sustaining near-wall cycle (Jimenez & Moin, 1991; Hamilton *et al.*, 1995; Waleffe, 1997; Jimenez & Pinelli, 1999). The viscous sublayer and the buffer layer fall into the 'near-wall region', as depicted in figure 1.2. A greater distance from the wall falls into the outer layer, where the influence of viscosity becomes negligible. The reference length scale is often assumed to be a value comparable to that of large scale turbulent eddies. In the case of turbulent channel flows, the half channel height (H) serves as the reference length. Asymptotic matching allows for the establishment of a logarithmic profile connecting the inner later and the outer layer (Millikan, 1938),

$$\bar{U}^+ = \frac{1}{\kappa} ln\left(z^+\right) + C, \tag{1.1}$$

where $\kappa \approx 0.41$ is the von Karman constant, and $C \approx 5.5$ is the intercept of the logarithmic layer (or log layer). Over the past, it was commonly believed that the log layer begins at approximately $z^+ \approx 30$ (Tennekes & Lumley, 1972) or $z^+ \approx 50$ (Pope, 2000). However, more recent studies have indicated that the extent of the log layer may depend weakly on the Reynolds number, with a suggested relationship of $z^+ \gtrsim z^+ 3Re_\tau^{-1/2}$ at Re_τ of the order of $O(10^4) - O(10^5)$ (Marusic *et al.*, 2013). Re_τ denotes the friction Reynolds number, $Re_\tau \equiv u_\tau H/\nu$, which represents the ratio between the characteristic length scale of eddies in the outer layer and the viscous length scale. $Re_\tau \equiv u_\tau H/\nu$ is considered in fluid dynamics, particularly in the study of turbulent flows over wall-bounded surfaces, because it is a dimensionless parameter that characterizes the intensity of turbulence and its impact on skin friction drag. By using the friction Reynolds number, researchers can non-dimensionalize the flow and compare different flow conditions across various systems. It provides a universal measure that allows for meaningful comparisons of flow behavior and drag reduction techniques.

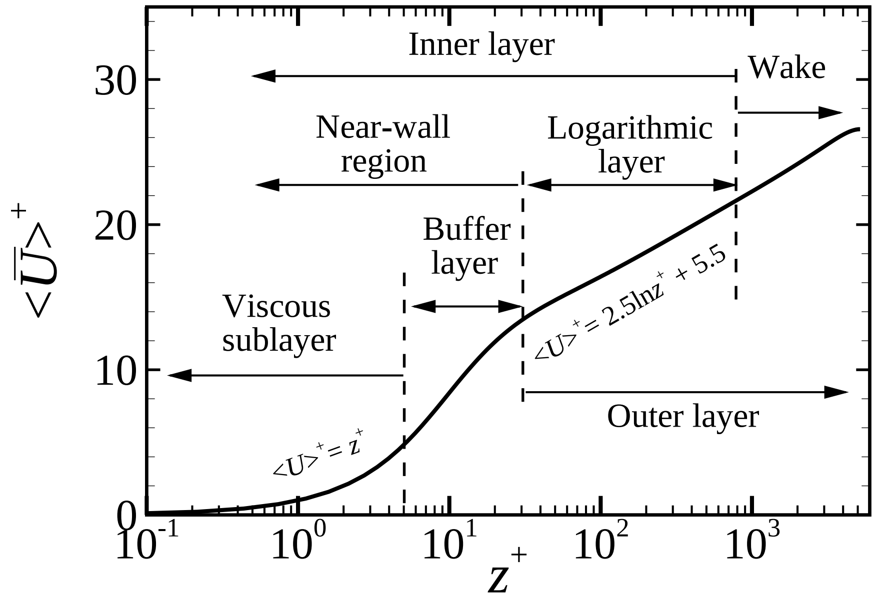

Figure 1.2: Mean streamwise velocity profile showing the inner and outer layers. The black solid line shows DNS data of the turbulent channel flow at $Re_\tau \approx 5200$ (Lee & Moser, 2015).

The understanding of near-wall turbulence is crucial when considering drag reduction strategies. This region is characterized by a self-sustaining cycle driven by coherent structures, namely streaks and quasi-streamwise vortices, as illustrated in figure 1.3. Streaks are longitudinal stripes with positive or negative streamwise velocity fluctuations. These fluctuations show the alternating low-velocity and high-velocity streaks, periodically observed in the spanwise direction. Experimental studies have indicated that the streamwise wavelength of streaks is typically around $\lambda_x^+ \approx 1000$, while their spanwise wavelength is approximately $\lambda_y^+ \approx 100$ (Kim *et al.*, 1971; Smith & Metzler, 1983). The self-sustaining process involves the interaction between streaks and vortices, where vortices redistribute the mean shear, amplifying the streaks' instability, which, in turn, generates new vortices, thus closing the cycle (Waleffe, 1997). The longitudinal vortices drive the displacement of slow fluid away from the wall within the low-velocity streaks, while fluid is pushed towards the wall, creating the high-velocity streaks. This phenomenon leads to an overall increase in the averaged wall shear stress, resulting in an increase in skin-friction (Orlandi & Jimenez, 1994).

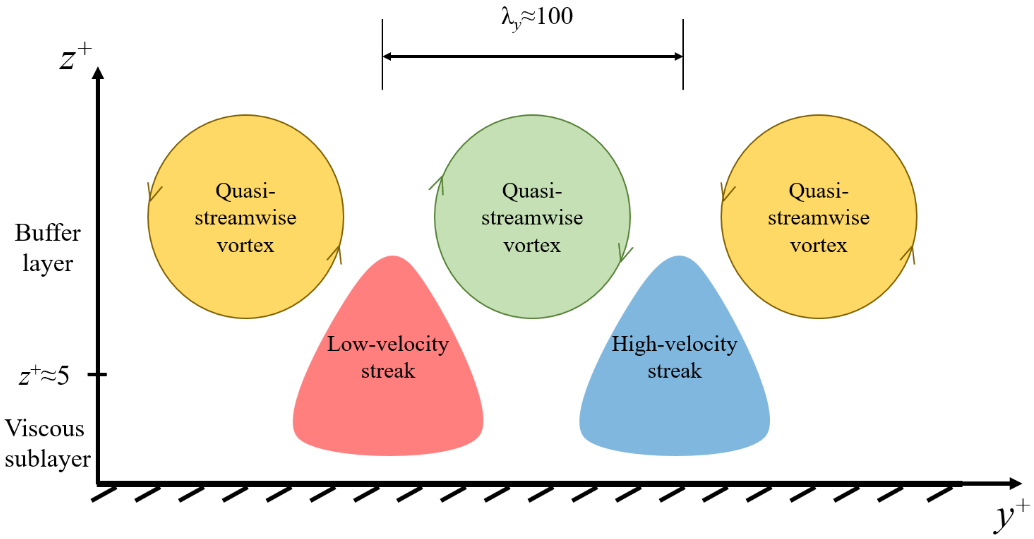

Figure 1.3: Sketch of the near-wall cycle across the spanwise wall normal plane with quasi-streamwise vortices and low- and high-velocity streaks.

1.1.2 Motivation for Skin-friction Drag Reduction (DR)

One notable feature of wall-bounded turbulent flows is a high skin-friction drag. Reducing the turbulent skin-friction drag on engineering surfaces such as oil pipelines, airplanes or ships,

DR methods	Active/passive	DR (%)
Non-surface treatment		
Blow/suction	Active	$\lesssim 25\%$
Spanwise wall-oscillation	Active	$\lesssim 50\%$
Gas/bubble injection	Active and/or passive	$\lesssim 80\%$
Polymer additives	Passive	$\lesssim 80\%$
Surface treatment		
Riblet surfaces	Passive	$\lesssim 10\%$
Permeable substrates	Passive	$\lesssim 20\%$
Superhydrophobic (SH) surfaces	Passive	$\lesssim 75\%$
Compliant surfaces	Passive	$\lesssim 8\%$
Hairy surfaces	Passive	$\lesssim 50\%$

Table 1.1: DR methods with active/passive flow controls: Blowing/suction (Choi *et al.*, 1994), spanwise wall-oscillation (Gatti & Quadrio, 2016), gas/bubble injection (Ceccio, 2010), polymer surfactant/additives (Toms, 1949), riblet surfaces (Bechert *et al.*, 1997a), permeable substrates (Rosti *et al.*, 2018), SH surfaces (Park *et al.*, 2014), compliant surfaces (Fukagata *et al.*, 2008), hairy surfaces (Takata *et al.*, 1996).

can lead to significant energy savings and reduction in carbon footprint. For example, $\sim 30\%$ reduction in turbulent skin-friction drag on ocean ships could result in an annual decrease in fuel consumption of ~ 700 million barrels of oil (McKeon *et al.*, 2013). A mere 1% reduction in skin-friction drag could enable an Airbus A340 to conserve approximately 400 kiloliters of jet fuel, amounting to a savings of approximately $300,000 per year (Kornilov, 2015). The annual fuel cost for all commercial airlines in the United States is about $10 billion—an expenditure that has remained relatively stagnant over the past decades (Hefner, 1988; Bushnell, 1998; Gad-el Hak, 2000). A significant amount of aviation fuel, up to 81% of Air Force energy budgets is required to overcome the drag, and almost half of the total drag comes from the skin-friction drag (Felder *et al.*, 2017). In light of these examples, the skin-friction drag reduction is indispensable to achieve energy savings and reduce the carbon footprint.

In recent years, two major approaches have emerged for mitigating turbulent skin-friction drag: Active and passive flow control techniques. Both approaches have been applied to wall-bounded turbulent flows in order to disturb the near-wall turbulence and its dynamics and thus reduce the skin-friction drag. Table 1.1 presents a comprehensive overview of various DR methods corresponding to both active and passive flow control techniques, along with their reported maximum DR values. Active flow control techniques are mostly represented in conjunction with arrays of sensors and actuators that inject (extract) momentum to (from) the targeting spots (Lin *et al.*, 1955; Choi *et al.*, 1994; Rathnasingham & Breuer, 2003; Diez & Dahm, 2004; Benard & Moreau, 2014) or the spanwise oscillation of wall surfaces to alter the near-wall or outer structures (Jung *et al.*, 1992; Leschziner, 2020; Ricco *et al.*, 2021; Marusic *et al.*, 2021). Unlike active flow control, passive flow control does not rely on external energy sources, making them more advantageous in terms of achieving higher net energy savings. In addition, passive strategies do not require the use of additional arrays of sensors and actuators, simplifying their implementation and reducing maintenance costs. Consequently, passive flow control has emerged as promising approaches for reducing turbulent skin-friction drag to date. Passive flow control is predominantly found in the form of surface treatments. In the following section, further details regarding surface treatments proposed up to date will be discussed.

1.2 Surface Treatments for Skin-friction DR

1.2.1 Drag-reducing Surfaces Inspired by Nature

Surface treatments inspired by the surfaces of living creatures have been proposed to reduce the turbulent skin-friction drag as a passive drag reduction strategy. Nature provides a rich source of inspiration, from the mucus-coated riblet structure of shark skin (Bechert & Bartenwerfer, 1989; Bechert *et al.*, 1997a; Garcia-Mayoral & Jimenez, 2011; Walsh, 1982; Walsh & Lindemann, 1984), to the superhydrophobic (SH) structure of the lotus leaf (Tretheway & Meinhart, 2002; Park *et al.*, 2014), feather structure of birds (Chen *et al.*, 2013), seal fur surfaces (Itoh *et al.*, 2006). A prominent function of these surfaces is the skin-friction DR.

To date, much of the interest in most man-made surfaces has been focused on riblet surfaces over the past several decades. The initial designs of micro-textured surfaces drew inspiration from the rib-like protrusions observed on shark skins, specifically the dermal denticles (Chernyshov & Zayets, 1970). In man-made implementations, the wall boundaries were carpeted with arrays of longitudinal ribs that rectify the turbulent flow in the streamwise direction by hampering the fluctuating cross-flow component. Numerous experimental (Bechert & Bartenwerfer, 1989; Bechert *et al.*, 1997a,b, 2020) and numerical studies (Luchini *et al.*, 1991; Choi *et al.*, 1993; Garcia-Mayoral & Jimenez, 2011; Endrikat *et al.*, 2021) have shown a successful skin-friction drag reduction with a systematic optimization of geometrical features of riblets. The skin-friction DR obtained in laboratory-scale experiments was achieved up to 10% for blade riblets with spanwise rib-spacing of ~ 16 wall unit, riblet height of ~ 8 wall unit, thickness-to-spanwise spacing of 0.5, and DRs were more modest, of $5-7\%$, in full-size applications (Bechert *et al.*, 1997a; Spalart & McLean, 2011).

Recently, anisotropic permeable substrates have been proposed in the pursuit of further improvement in skin-friction DR. Rather than employing isotropic permeable surfaces that resulted in drag increase (Rosti *et al.*, 2015; Kuwata & Suga, 2016), the integration of anisotropic permeable surfaces on the wall provides skin-friction DR that far exceeds the maximum limit obtained from riblets, which is approximately 10%. By modulating the directionality and permeability, it becomes possible to address the limitations observed with riblets. As the size of the riblet surface increases, additional detrimental effects emerge, causing the breakdown of drag reduction performance and eventually enhancing skin-friction drag. This degradation was attributed to the spanwise fluctuation induced toward the surface indentation and the resulting onset of wall-normal transpiration. The degradation appears prominently when the sqaure root of groove area exceeds 11 in wall unit (Garcia-Mayoral & Jimenez, 2011). On the other hand, streamwise-preferential substrates where the flow is rectified into the wall-parallel direction, but hampered in wall-normal direction provided substantial improvements in drag reduction can be achieved (Rosti *et al.*, 2018; Gomez-de Segura & Garcia-Mayoral, 2019), suggesting that the suppression of wall-normal fluctuation was the promising pathway to achieve higher DRs. These studies have shown that the streamwise-preferential substrates provided the skin-friction DR up to $20-25\%$ at $Re_\tau \approx 180$.

Another category of surface treatments that has garnered significant attention is superhydrophobic (SH) surfaces. These surfaces draw inspiration from the water-repellent structure observed on lotus leaves, butterfly wings, water striders, desert beetles, spider webs (Gorb, 2009). A few of these surfaces possess a rough exterior covered with a water-repellent wax, enabling water to effortlessly slide off the surface (Ma & Hill, 2014). By mimicking the structure of natural surfaces, this class of micro-textured surfaces is made of a combination of surface micro-textures and liquid-repelling coatings. In micro-channels with arrays of SH longitudinal micro grooves implemented on both channel walls, experiments have shown DR up to 50% with the spanwise gap spacing between $0.7-4.8$ in wall unit and the spacing-width ratio of 1 (Daniello *et al.*, 2009). Later, DRs of up to 75% have been reported in turbulent boundary layer flows with arrays of SH longitudinal micro grooves of spanwise gap spacing between 0.8 and 1.6 and the spacing-to-width ratio between 1 and 19 (Park *et al.*, 2014).

The skin of dolphins offers an intriguing alternative surface-texture for skin-friction DR (Kramer, 1960, 1962). This unique surface, known as a ‘compliant surface,’ is passively reconfiguring its surface morphology in response to the surrounding fluid flows. Several theoretical and experimental studies (Gad-el-Hak, 2000 and references therein) postulated that compliant surfaces suppressed laminar-turbulent transition effectively and thus mitigate the effects of skin-friction drag. Earlier DNS study (Fukagata *et al.*, 2008) demonstrated that an anisotropic compliant wall with optimized parameter sets successfully provided the skin-friction DR up to 8% in a turbulent channel flow at $Re_\tau \approx 110$.

1.2.2 Limitations of the Existing Drag-reducing Surfaces

Despite the remarkable results from the drag-reducing surface textures discussed earlier such as riblet surfaces, anisotropic permeable substrates, and SH surfaces, their geometrical features are generally fixed in ‘physical unit’. In other words, these surfaces have specific surface topology, which is optimized at a particular friction Reynolds number. However, in real engineering applications involving air, ground, and underwater vehicles, their speed and direction continue to change over time, leading to dynamic variations in the friction Reynolds number and the streamwise direction over the surfaces. Therefore, the surface textures unalterably designed for one friction Reynolds number may perform poorly at a different friction Reynolds number due to the change of the characteristic surface size in wall units.

A growing body of evidence has indicated the drawbacks of these surfaces. With increasing Reynolds number, the riblet surface, characterized by a fixed size in physical units, experiences an increase in its size in wall units. This growth eventually leads to a substantial intrusion of the fluctuating cross-flow component into the surface indentations. Consequently, there is an amplification of the wall-normal momentum flux between the overlying flow and the surface indentations, resulting in an increase in skin-friction (Garcia-Mayoral & Jimenez, 2011). Similarly, the drag-reducing performance represented by the anisotropic permeable substrates was also degraded as the friction Reynolds number increased (Gomez-de Segura & Garcia-Mayoral, 2019). For SH surface, its implementation as a practical method for reducing turbulent skin-friction drag is still limited due to the challenges posed by high shear rates and high pressure fluctuations at higher Reynolds numbers. As Reynolds number increases, the gas pockets trapped in the surface indentations of SH surfaces tend to deplete and get replaced by the working fluid, negating their drag-reducing capabilities. (Zheng *et al.*, 2009; Checco *et al.*, 2014; Samaha *et al.*, 2012).

Moreover, several investigations have raised concerns regarding the use of compliant surfaces for skin-friction DR. Although an earlier study suggested that compliant surfaces could achieve skin-friction DR of up to 8% at a friction Reynolds number of approximately 110 (Fukagata *et al.*, 2008), recent studies have shown that at higher Reynolds numbers, the presence of wall compliance resulted in the generation of large-amplitude waves propagating downstream (Kim & Choi, 2014; Rosti & Brandt, 2017; Xia *et al.*, 2019; Rosti & Brandt, 2020). These waves enhanced the fluid motions and ultimately resulted in an increase in skin-friction rather than its reduction.

Given the limitations posed by the existing drag-reducing surfaces, it is still necessary to explore alternative surface-textures that can address these limitations and provide effective reduction of skin-friction drag. This entails exploring surfaces that adapt to diverse flow conditions by dynamically adjusting their configuration, while also ensuring consistent and reliable skin-friction DR.

1.3 Hairy Surfaces as an Alternative Drag-reducing Surface

1.3.1 Hairy Surfaces Existing as Dynamic Functional Surfaces in Nature

Slender and flexible outgrowths or protrusions are called ‘hairs’. This description is general, valid to any similar structure regardless of its biological origin (Gorb, 2009). Hairy surfaces, characterized by an assembly of these hair-like structures, are widespread in nature and serve multitude functions. At the microscale, hairy surfaces enable water-repellent capabilities, allowing spiders and aquatic insects such as water striders to move on water surfaces and protect their respiratory organs from unwanted water entry (Gorb, 2009; and references therein). In the context of respiratory tract, cilia and flagella, which are contractile hair-like structures, facilitate fluid transport in the mucus layer, thereby preventing the onset of chronic respiratory diseases in human beings (Han & Peskin, 2018; Loiseau *et al.*, 2020). At the macroscale, underwater creatures (e.g. fish, seals) and flying insects utilized their filamentous hairs to sense the velocity field as well as the pressure distribution along the body (Tao & Yo, 2012). Poroelastic surfaces found in owl's wing feathers effectively weaken the generation of aerodynamic noise (Jaworski & Peake, 2013; Clark & Jaworski, 2020). Experimental and numerical studies showed that hairy surfaces coated along cylinders and airfoils effectively suppressed the separation region behind the objects and thus reduced the pressure drag (Favier *et al.*, 2009; Brücker & Weidner, 2014; Hasegawa & Sakaue, 2021; Hasegawa *et al.*, 2022).

Another primary function of hairy surfaces is the skin-friction DR, which is particularly significant in future engineering applications. This can be observed in the fur of aquatic mammals, such as seals (Itoh *et al.*, 2006). The researchers reported that when real seal fur textures were attached to turbulent channel walls, they exhibited a better adaptability compared to riblet surfaces. This adaptability allowed the seal fur textures to provide a greater skin-friction DR across a wider range of Reynolds numbers. Given the significance of hairy surfaces in skin-friction DR, they can be considered as a promising candidate for alternative drag-reducing surfaces. The subsequent sections will delve into a more detailed exploration of the topic, focusing on the role of hairy surfaces in reducing skin-friction drag.

1.3.2 Experimental Studies of Skin-friction DR with Hairy Surfaces

To the knowledge of the author, very few experimental studies could be found in the literature exploring the skin-friction drag reduction using hairy surfaces. Takata *et al.* (1996) investigated turbulent skin-friction drag reduction in pipe flow using a carpet of microfibers implanted on the inside walls of the pipe. The maximum drag reductions of up to approximately 50% were reported with micro-fibers of height $6-8$ wall units, implanted with no preferred orientation. Itoh *et al.* (2006) reported drag reductions of up to 12% using a seal fur surface in turbulent channel flow at $Re_\tau \approx 150$. They observed that the hairs are distributed in streamwise-preferential configuration, with various hair heights ranging from 2 to 18 in wall units. Brücker (2011) carried out experiments in an oil channel, employing a carpet of elastomeric micro-pillars, comprised of sparsely implanted filaments with height of 30 wall units, streamwise and spanwise spacings of 15 and 30 in wall units, respectively. He observed a reduced meandering and stabilization of the near-wall streaks, arguing that this was the signature of the skin-friction drag reduction, although DR remained to be reported. Regarding the results from these experimental studies, a common feature represented by drag-reducing hairy surfaces is that their heights do not exceed the order of $O(10)$ in wall units and their spacings are comparable to their heights. Although these experiments showed that hairy surfaces provided a promise for the skin-friction DR, its underlying mechanism remains to be revealed.

1.3.3 Computational Studies of Turbulent Flows over Hairy Surfaces

Numerical investigations of turbulent flow over hairy surfaces to date have primarily focused on canopy flows, which are encountered in terrestrial and aquatic vegetation (Tschisgale *et al.*, 2021; He *et al.*, 2022; Monti *et al.*, 2023) as illustrated in figure 1.4 (*a*). Previous simulations commonly treated the canopy element as a continuous medium and relied on predefined drag coefficients for the prediction of canopy drag. However, this approach is inadequate when dealing with deformable canopies interacting with turbulent flows. Deformable canopies continuously change their postures and shapes, necessitating dynamic adjustments of the drag coefficients. Consequently, there is a need for an explicit solution that accurately resolves the drag forces acting on deformable canopies.

The immersed boundary (IB) method provides a viable approach for addressing this challenge. The IB method explicitly solves the interaction forces between the solid structures and the fluid by employing interpolation and spreading operations (Peskin, 1972; Roma *et al.*, 1999; Li *et al.*, 2016). By utilizing the IB method, the drag forces exerted on the filaments can be directly obtained without relying on any assumptions on filament drag. Thus, this approach allows for a more accurate representation of the drag experienced by the deformable filaments in the canopy. Furthermore, employing the IB method enables capturing the detailed correlation between the drag force exerted by the hairy filaments and the fluctuating fluid velocity. This correlation provides valuable insights into the transport of turbulent energy associated with the motion of the hairy filaments. Hence, by resolving the interaction forces with IB method, it can be better understood how turbulent kinetic energy is transported and distributed by the hairy filaments throughout the fluid flow.

Recent DNS studies within the IB framework (Monti *et al.*, 2020; Sharma & Garcia-Mayoral, 2020*a*,*b*) provided valuable insights into the interaction between turbulence and filamentous canopies, however, their applications were limited to roughness elements that increase the drag, and much of interests was focused on the mixing layer instabilities appeared in the interface between 'rigid' canopies and their overlying flows. In fact, the rigid canopies acts as a roughness, increasing the drag. To gain more insights into the interaction between realistic canopy elements and turbulent flows, recent numerical studies have been conducted to study turbulent flows over 'flexible' canopies. Wall-resolved large-eddy simulations (LES) carried out by (Tschisgale *et al.*, 2021) investigated the characteristics of coherent structures that appear in the mixing layer and their impacts on the large-scale collective motion of flexible canopy elements, commonly referred to as honami/monami. He *et al.* (2022) conducted spectral analysis of turbulent kinetic energy budgets to further comprehend the underlying mechanism of the interaction between flexible canopy elements and turbulent flow. They observed that the canopy motions are predominantly observed at the monami scale associated with the coherent structures in the mixing layer and the wake scale associated with the interval between adjacent canopy elements. Furthermore, a different DNS study (Monti *et al.*, 2023) revealed that this canopy motion was a fully-passive behavior in response to the surrounding turbulent flows. Although these numerical studies have provided valuable insights into the interaction between hairy filaments and turbulent flows, none of them showed any skin-friction DR. It can be conjectured that the parameter sets given in these computational studies are not beneficial for skin-friction DR. Specifically, the canopy height set in these studies were the order of $O(100) - O(1000)$ in wall units. This range differs significantly from the heights of drag-reducing hairy surfaces observed in the aforementioned experiments where the height of drag-reducing hairy surfaces did not exceed the order

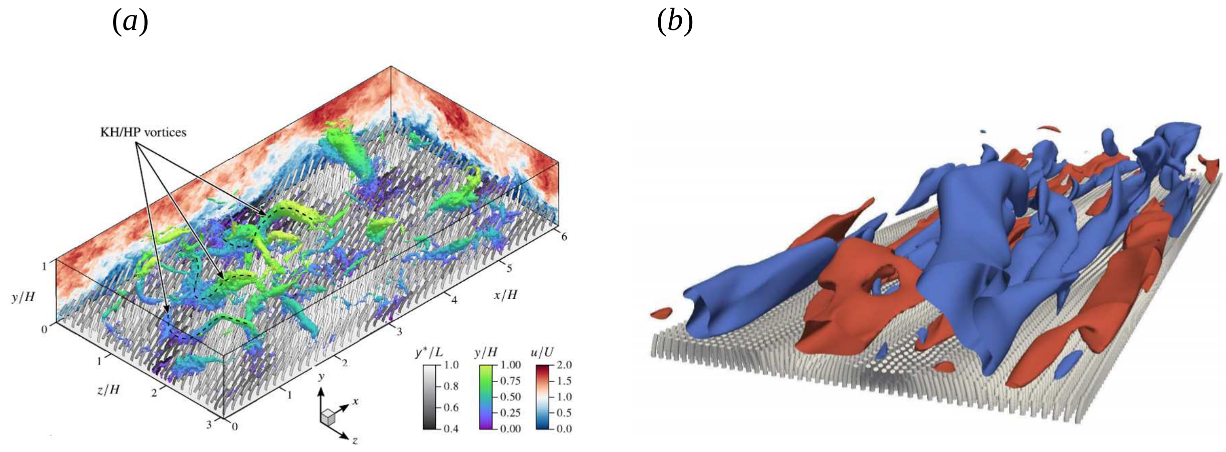

Figure 1.4: Flow structures existing above the hairy surfaces (or canopy). (*a*) Isosurfaces of pressure fluctuation at a value of $p'/(0.5\rho_f U_b^2) = -0.4$ in a turbulent open-channel flow (Tschisgale *et al.*, 2021). (*b*) Isosurfaces of the streamwise velocity fluctuations at a value of $u'^+ = \pm 3$ in a turbulent channel flow confined by two-parallel, no-slip walls (Sundin & Bagheri, 2019).

of $O(10)$ in wall units.

In a separate DNS study conducted by Sundin & Bagheri (2019), the effects of elastic hairy surfaces on turbulent channel flows and their dynamic response to turbulence were investigated at $Re_\tau \approx 180$ as illustrated in figure 1.4 (*b*). In their DNS study, the density ratio ranged from 1 to 800, and the height and diameter of the hairs were fixed to approximately 20 and 2 in wall units, respectively. The hairs were distributed at one side of the channel walls with the uniform-spacing of approximately 8–16 in wall units. Sets of these parameters were determined corresponding to the range of the characteristic time scale of the hairy filaments. The targeted ratio of the characteristic time scale of the hairy filaments to the characteristic time scale of near-wall turbulence varied from 0.21 to 1.5, and accordingly the density ratio and flexibility were adjusted. It is noteworthy that the hairy filaments were relatively stiff, resulting in limited deflection with mean values ranging from 0.48 to 1.28 in wall units. This limited deflection caused the hairy filaments to protrude into the upper near-wall region, and they act as roughness elements and ultimately increase the skin-friction drag. This implies that the significance of flexibility in conjunction with height and spacing is indicative of its pivotal role in the performance of hairy surfaces on skin-friction DR. To this end, a comprehensive parametric investigation is warranted to identify an optimal combination of governing filament parameters, encompassing filament height, spacing, density ratio, and flexibility, the latter typically quantified by the bending rigidity of the hairy filaments.

1.3.4 Plausible Hypotheses Regarding Skin-friction DR with Hairy Surfaces

As can be seen in the literature, none of the numerical simulation studies have been able to reproduce skin-friction DR using hairy surfaces to date, despite the existence of experimental evidence. In the context of skin-friction DR, it can be expected that increasing the height and bending stiffness of the hairy filaments as well as matching their time scale to that of the near-wall turbulence may not be a suitable approach in regards to the failure of achieving skin-friction present in the previous simulation studies (Sundin & Bagheri, 2019; Tschisgale *et al.*, 2021; He *et al.*, 2022; Monti *et al.*, 2023). Instead, a more promising pathway could involve the use of highly flexible filaments, where the characteristic time scale of these filaments is matched to other relevant time scales. Moreover, the underlying mechanism behind the skin-friction DR with hairy surfaces remains to be clarified. One plausible hypothesis for the mechanism of skin-friction drag reduction is that the presence of hairy filaments disrupts the transfer of turbulent energy, which is essential for sustaining turbulence. The hairy filaments could absorb and redirect the energy that would contribute to the sustenance of turbulence, ultimately mitigating the effects of turbulence and thus reducing skin-friction drag. To gain better description of these hypotheses, it would be worthy to analyze the intercomponent/interscale energy transfer and its modulation by the presence of hairy filaments.

1.4 Objectives of the Dissertation

Turbulent skin-friction DR was investigated by direct numerical simulation (DNS) in turbulent channel flow with hairy surfaces, where the one-dimensional hairy filaments are uniformly distributed on both channel walls. A lattice Boltzmann, immersed boundary (LB-IB) method was employed in this study. A direct forcing IB scheme, supported by reciprocal interpolation-spreading of operators, was adopted. The dynamics of the filaments was tracked by solving the dynamic Euler-Bernoulli beam equation. In comparison to the previous studies where the hairy filaments were modeled with two-dimensional plate (Tschisgale *et al.*, 2021; He *et al.*, 2022) or three-dimensional cylindrical bodies (Sundin & Bagheri, 2019), the hairy filaments were modeled as one-dimensional flexible filament in similar to the other studies Monti *et al.* (2019, 2023). Simulations were performed in turbulent channel flows at a bulk Reynolds number of $Re_b \approx 7200$, corresponding to a friction Reynolds number of $Re_\tau \approx 221$ in a base turbulent channel flow with smooth, no-slip walls. The primary objective of the present study is to reproduce a positive turbulent skin-friction DR with hairy surfaces and elucidate its underlying mechanism. To achieve this objective, several sub-objectives are set as below:

- To develop a precise and robust numerical method for simulating fluid-structure interaction within LB-IB framework.
- To verify and validate the proposed numerical method and confirm its superiority over the previously suggested LB-IB methods.
- To conduct a parametric study to investigate the effects of filament parameters, such as filament height, spacings, density ratio between the hairy filaments and fluids, and bending rigidity, on the behavior of hairy filaments and the resulting flow statistics.
- To explore skin-friction DRs in terms of the filament parameters and identify a governing parameter that exhibits a consistent trend of DR.

- To analyze the budget terms of Reynolds stress components to examine the modulation of intercomponent energy transfer in the presence of hairy filaments.
- To investigate the role of the hairy filaments in terms of the interscale energy transfer by analyzing the budget terms of mean kinetic energy and turbulent kinetic energy.
- To gain insights into the overall modulation of interscale energy transfer resulting from the presence of hairy filaments by analyzing one-dimensional spectra of turbulent kinetic energy and Reynolds shear stress.

By addressing these objectives, this study aims to advance the understanding of turbulent skin-friction DR with hairy surfaces and provide valuable insights into its physical mechanisms.

1.5 Organization of the Dissertation

The dissertation is organized as follows. Chapter II provides an overview of the LB method and IB method, as well as their coupling schemes. Subsequently, a precise and rigorous LB-IB method will be proposed and compared to previously suggested LB-IB methods in terms of numerical accuracy, robustness, and stability. The verification and validation of the proposed LB-IB method will be presented. In Chapter III, the characteristics of filament deflections, resulting skin-friction drag reductions, and flow statistics obtained from the parametric study will be discussed. Chapter IV focuses on investigating the underlying mechanism of skin-friction drag reduction with hairy surfaces, specifically analyzing the modulation of intercomponent and interscale energy transfer. Chapter V provides summary and conclusions of this study and suggests the future research directions.

CHAPTER 2

Numerical Methodology

Turbulent skin-friction drag reduction with flexible filamentous surfaces is investigated by direct numerical simulation (DNS) using an immersed boundary-lattice Boltzmann (IB-LB) method. In this method, the dynamics of the fluid flow is described by employing LB method with standard D3Q19, single relaxation time, Guo's forcing function, Bhatnagar-Gross-Krook lattice models (Krüger *et al.*, 2017). The dynamics of elastic, slender hairy filaments can be described by solving the dynamic Euler-Bernoulli beam equation, which balances out the inertia, tension, bending, interaction, and repulsive forces exerted on the hairy filaments (Favier *et al.*, 2014). A direct-forcing IB method combined with the diffusive-interface scheme is adopted to simulate the fluid-flexible structure interaction. The reciprocal interpolation-spreading operations, suggested in the previous study (Pinelli *et al.*, 2010), is improved to achieve better numerical accuracy, instability, and robustness. Throughout all simulations, the mean pressure gradient is dynamically adjusted to keep the bulk Reynolds number constant during the course of the simulations. A mathematical formulation of maintaining the constant flow rate (or constant bulk Reynolds number) is obtained from a control volume analysis over the entire channel with/without the presence of the hairy filaments. Grid embedding is employed to improve the accuracy of the computations from the channel wall up to about 30 wall units above the channel wall for the 'base' turbulent channel flow with smooth, no-slip walls and the filament tips at undeformed (or initial) state for the turbulent channel flow with hairy surfaces, respectively. A two dimensional domain decomposition is applied in parallelization of the IB-LB simulations.

The numerical methods utilized in the present study have been verified and validated through a series of numerical experiments. All of the details in the numerical methods and solution procedures will be discussed in the following sections.

2.1 Fluid Solver

2.1.1 Lattice Boltzmann (LB) Method

LB method is a numerical simulation technique derived from kinetic theory. This method relies on a mesoscopic description of the fluid to compute its mascroscopic behavior. It has gained popularity for simulating incompressible, viscous fluid flows due to its advantages over Navier-Stokes (NS) solver in terms of numerical simplicity and parallelization. Compared to NS solvers, LB method is solving an inherently explicit, linear equation, obviating the numerical difficulties resulting from the nonlinear convective term. In addition, the pressure is calculated in a simpler way, using the equation of state, $p = \rho c^2/3$, where c is the lattice speed, and ρ is the fluid density. This reduces the burden of calculating the pressure gradient, which typically requires intensive computational costs as well as complicated solution procedures for NS solvers. Moreover, LB method reduces the challenge of parallelization due to local nature of its computational stencil. Regarding these advantages, LB method has been the subject of rapid developments in the recent years.

In the numerical simulation of fluid flows, LB method is typically adopted employing single-relaxation-time lattice Boltzmann equation (SRT-LBE). SRT-LBE was initially developed as an improvement over the lattice gas automata in a discrete lattice and time (Frisch *et al.*, 1986; Chen *et al.*, 1992). It was shown later that SRT-LBE can be derived from the continuous Boltzmann equation with an appropriate collision model in discrete phase space and time (He & Luo, 1997*a*). For its basic formulation, LB method tracks the evolution of sets of particle distribution function (or discrete velocity distribution function), $f_i(\boldsymbol{x}, t)$, which represents the density of particles with discrete particle velocity $\boldsymbol{c}_i = (c_{ix}, c_{iy}, c_{iz})$ at a lattice position $\boldsymbol{x}$ and time t. Sets of the discrete particle velocity c_i can be denoted in a D*d*Q*i* model , where *d* is the number of spatial dimensions and *i* is the number of discrete velocity vectors in a lattice. In a three-dimensional simulation of fluid flow, three lattice models are commonly leveraged: D3Q15, D3Q19, and D3Q27. Among these lattice models, D3Q15 model has smaller memory footprint and less computationally demanding procedures, but it uses fewer number of discrete velocity vectors, resulting in less accurate numerical results. On the other hand, D3Q27 provides more accurate results with an increased number of discrete velocity vectors, but requires intensive memory usage. To balance numerical accuracy and memory usage, D3Q19 lattice model has been widely adopted as a reasonable choice. Figure 2.1 shows the lattice arrangements of D3Q19 model. Set of weight factors, w_i and discrete velocity vectors are tabulated for D3Q19 lattice model as can be seen in Table 2.1.

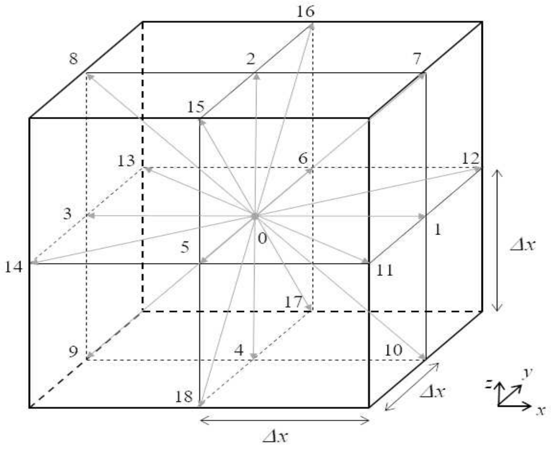

Figure 2.1: Lattice arrangements of D3Q19 model

The LB equation can be obtained by discretizing the Boltzmann equation in lattice velocity space, physical space, and time, which is given as

$$f_i(\mathbf{x} + \mathbf{c}_i, \Delta t) - f_i(\mathbf{x}, \Delta t) = \Omega_{col,i}. \tag{2.1}$$

i	w_i	$\boldsymbol{c}_i$
0	1/3	(0,0,0)
1 —6	1/18	(1,0,0), (0,0,1), (-1,0,0), (0,0,-1), (0,-1,0), (0,1,0)
7 —18	1/36	(1,0,1), (-1,0,1), (-1,0,-1), (1,0,-1), (1,-1,0), (1,1,0), (-1,1,0), (-1,-1,0), (0,-1,1), (0,1,1), (0,1,-1), (0,-1,-1)

Table 2.1: Set of weight factors,w_i, and discrete lattice velocity vectors, $\boldsymbol{c}_i$, of D3Q19.

The particle collisions are modeled by a collision operator, $\Omega_{col,i}$, to describe the redistribution of particles at each site. Bhatnagar-Gross-Krook (BGK) collision operator was introduced to replicate the macroscopic behavior of fluids (Bhatnagar *et al.*, 1954):

$$\Omega_{col,i} = \frac{\Delta t}{\tau}(f_i^{eq} - f_i). \tag{2.2}$$

where τ is the relaxation time towards the local equilibrium. The relaxation time is obtained in relation with the kinematic viscosity of fluids, ν:

$$\frac{\tau}{\Delta t} = \frac{3\nu\Delta t}{\Delta x^2} + 0.5. \tag{2.3}$$

The equilibrium distribution function, f_i^{eq}, is a function of local macroscopic quantities, and can be derived from Taylor series (He & Luo, 1997*a*,*b*) or Hermite polynomial expansion (Shan & He, 1998; Shan *et al.*, 2006) of the Maxwell-Boltzmann distribution,

$$f_i^{eq}(\boldsymbol{x}, t) = w_i\rho\left(1 + \frac{\boldsymbol{c}_i\cdot\boldsymbol{u}}{c_s^2} + \frac{(\boldsymbol{c}_i\cdot\boldsymbol{u})^2}{2c_s^4} - \frac{\boldsymbol{u}\cdot\boldsymbol{u}}{2c_s^2}\right), \tag{2.4}$$

where $\boldsymbol{u}$ is the fluid velocity vector, $\boldsymbol{u}(\boldsymbol{x}, t) = [u(\boldsymbol{x}, t), v(\boldsymbol{x}, t), w(\boldsymbol{x}, t)]$, ρ is the fluid density, $\rho = \rho(\boldsymbol{x}, t)$, and c_s is the speed of sound. With the BGK collision model, the discrete Boltzmann equation (Equation 2.1) can be reformulated as the SRT-LBE,

$$f_i(\boldsymbol{x} + \boldsymbol{c}_i \Delta t, t + \Delta t) - f_i(\boldsymbol{x}, t) = \frac{\Delta t}{\tau} \left(f_i^{eq}(\boldsymbol{x}, t) - f_i(\boldsymbol{x}, t) \right). \tag{2.5}$$

The external forces exerted on the fluids (e.g. mean pressure gradient, interaction force exerted by an immersed solid body) are incorporated into LB equation via an appropriate forcing function. In the presence of the forcing function, SRT-LBE can be rewritten as:

$$f_i(\boldsymbol{x} + \boldsymbol{c}_i \Delta t, t + \Delta t) - f_i(\boldsymbol{x}, t) = \frac{\Delta t}{\tau} (f_i^{eq}(\boldsymbol{x}, t) - f_i(\boldsymbol{x}, t)) + \Delta t G_i. \tag{2.6}$$

Attaining precise predictions of fluid flows depends on the forcing function, G_i, because the mesoscopic description of the forcing function must be appropriately addressed to ensure an exact reproduction of macroscopic fluid behavior. Although several forcing functions have been proposed from a number of previous studies (He *et al.*, 1997; Martys *et al.*, 1998; Luo, 1998, 2000; Buick & Greated, 2000), Chapman-Enskog multiscale analysis demonstrated that the proposed forcing functions failed to reproduce the exact form of the macroscopic equations such as the continuity equation and NS equation (Guo *et al.*, 2002). Later, it was shown that Guo's proposed forcing function ensured the exact macroscopic equations and also held the second order accuracy (Guo *et al.*, 2002; Kang & Hassan, 2011). Due to its better accuracy and robustness, Guo's forcing function has been widely adopted to incorporate the external forces into LB equation, expressed as

$$G_i = \left(1 - \frac{\Delta t}{2\tau}\right) w_i \left(\frac{\boldsymbol{c}_i - \boldsymbol{u}}{c_s^2} + \frac{(\boldsymbol{c}_i \cdot \boldsymbol{u})\boldsymbol{c}_i}{c_s^4} \right) \cdot \boldsymbol{f}_{ext}, \tag{2.7}$$

where $\boldsymbol{f}_{ext}$ is the net external force (per unit volume). For a channel flow with smooth, no-slip walls, the pressure force accounting for the pressure gradient imposed in a channel flow is included in the external force, giving $\boldsymbol{f}_{ext} = \boldsymbol{f}_p$. In the presence of the surface-textured walls, the interaction force is added, giving $\boldsymbol{f}_{ext} = \boldsymbol{f}_p + \boldsymbol{f}_{IB}$.

The solution procedure of LB equation includes two main sub-steps: Collision and streaming steps. More than one particle that arrive at the same point from different directions collide with each other. Particles under the collision process exchange their momentum, then change their velocities according to the collision rule. After the collision, particles propagate and stream into neighboring sites. Their mathematical descriptions are shown as

Collision step (relaxation)

$$f_i^*(\boldsymbol{x},t) = f_i(\boldsymbol{x},t) + \frac{\Delta t}{\tau}(f_i^{eq}(\boldsymbol{x},t) - f_i(\boldsymbol{x},t)) + \Delta t G_i. \tag{2.8}$$

Streaming step (propagation)

$$f_i(\boldsymbol{x} + \boldsymbol{c}_i \Delta t, t + \Delta t) = f_i^*(\boldsymbol{x},t). \tag{2.9}$$

After the collision and streaming steps, the macroscopic fluid density and velocity are calculated by taking the leading moments of the distribution functions,

Macroscopic variables

$$\rho(\boldsymbol{x},t) = \sum_i f_i(\boldsymbol{x},t), \tag{2.10}$$

$$\rho(\boldsymbol{x},t)\boldsymbol{u}^{noF}(\boldsymbol{x},t) = \sum_i \boldsymbol{c}_i f_i(\boldsymbol{x},t), \tag{2.11}$$

$$\boldsymbol{u}(\boldsymbol{x},t) = \boldsymbol{u}^{noF}(\boldsymbol{x},t) + \frac{\Delta t}{2\rho(\boldsymbol{x},t)}\boldsymbol{f}_{ext}(\boldsymbol{x},t). \tag{2.12}$$

where $\boldsymbol{u}^{noF}$ is the fluid velocity with no external forces. In the presence of the pressure force, $\boldsymbol{f}_p$, as well as the net external force, $\boldsymbol{f}_{IB}$, the net external force is expressed by $\boldsymbol{f}_{ext} = \boldsymbol{f}_p + \boldsymbol{f}_{IB}$. With these components, the equation 2.12 can be rewritten in terms of the interaction force,

$$\boldsymbol{f}_{ext}(\boldsymbol{x}, t) = \left[\boldsymbol{f}_p(\boldsymbol{x}, t) + \boldsymbol{f}_{IB}(\boldsymbol{x}, t)\right] = \frac{2}{\Delta t}\left(\rho(\boldsymbol{x}, t)\boldsymbol{u}(\boldsymbol{x}, t) - \rho(\boldsymbol{x}, t)\boldsymbol{u}^{noF}(\boldsymbol{x}, t)\right). \tag{2.13}$$

2.1.2 Physical Constraints of Fluid Flow

Table 2.2 presents the basic predefined parameters utilized in LB simulations. The simulation parameters are normalized by the grid spacing, Δx, the time step, Δt, and the discrete lattice speed, $c = \Delta x/\Delta t$, as often expressed in ‘LB units’. In the solution procedure of LB equation for a channel flow, the bulk Reynolds number Re_b, the half channel height ($H/\Delta x$), and CFL number, which is equivalent to the centerline velocity of the channel, $CFL = U_c/c = U_c\Delta t/\Delta x$ are specified. Then, the calculation of other LB simulation parameters is followed such as the bulk velocity (U_b/c), kinematic viscosity ($\nu\Delta t/\Delta x^2$), relaxation time ($\tau/\Delta t$).

Parameters	Physical domain	Parameters in LB units
Bulk Reynolds number	Re_b	$Re_b = U_bH/\nu = (U_b\Delta t/\Delta x)(H/\Delta x)/(\nu\Delta t/\Delta x^2)$
CFL number	CFL	$CFL = U_c/c = U_c\Delta t/\Delta x$
Half channel height	H	$H/\Delta x$
Kinematic viscosity	ν	$\nu\Delta t/\Delta x^2$
Relaxation time	τ	$\tau/\Delta t$

Table 2.2: Basic parameters of LB simulations.

For example of a laminar channel flow, the first procedure is to set Reynolds number, channel height, and CFL number. The bulk velocity is determined analytically from the correlation between the bulk velocity and the centerline velocity $U_c = \frac{3}{2}U_b$. Once these parameters in LB units are set, the other variables are subsequently calculated in the procedure shown below:

(1) Set Re_b, $H/\Delta x$, CFL

(2) Obtain bulk velocity U_b

$$Re_b = \frac{U_bH}{\nu} = \frac{(U_b/c)(H/\Delta x)}{(\nu\Delta t/\Delta x^2)} \tag{2.14}$$

$$\frac{U_b}{c} = \frac{2U_c}{3c} = \frac{2}{3}(CFL) \tag{2.15}$$

(3) Determin kinematic viscosity and relaxation time

$$\nu \Delta t / \Delta x^2 = \frac{(U_b/c)(H/\Delta x)}{Re_b} = \frac{2(CFL)(H/\Delta x)}{3Re_b} \tag{2.16}$$

$$\tau / \Delta t = \frac{3\Delta t \nu}{\Delta x^2} + 0.5 = \frac{3(U_b/c)(H/\Delta x)}{Re_b} + 0.5 \tag{2.17}$$

However, in contrast to laminar flow, the correlation between U_c and U_b cannot be obtained through analytical procedure for turbulent channel flow. Instead, Dean's correlation (Dean, 1978) can be used to correlate U_c with U_b. Once U_b is determined, the remaining parameters can be subsequently calculated. Furthermore, the parameterization depends on which physical constraint is applied, whether it is a constant pressure gradient (CPG) and a constant flow rate (CFR). The parameterization details for turbulent channel flow under CPG and CFR conditions are further elaborated in the following sections.

2.1.2.1 Constant Pressure Gradient (CPG)

(1) Set Re_b, $H/\Delta x$, CFL

(2) Approximate friction Reynolds number Re_τ

$$C_f = 0.073(2Re_b)^{-1/4} \tag{2.18}$$

$$C_f = \frac{\tau_w}{0.5\rho U_b^2} = \frac{\rho u_\tau^2}{0.5\rho U_b^2} = \frac{2u_\tau^2}{U_b^2} = \frac{2Re_\tau^2}{Re_b^2} \tag{2.19}$$

$$Re_\tau = 0.1751 Re_b^{7/8} \tag{2.20}$$

(3) Determine kinematic viscosity and relaxation time

$$\frac{\nu\Delta t}{\Delta x^2} = \frac{u_\tau H}{Re_\tau}\frac{\Delta t}{\Delta x^2} = \frac{(u_\tau/c)(H/\Delta x)}{Re_\tau} = 0.110(H/\Delta x)(CFL)Re_\tau^{-1.1296} \tag{2.21}$$

$$\frac{\tau}{\Delta t} = \frac{3\nu\Delta t}{\Delta x^2} + 0.5 = \frac{3(u_\tau/c)(H/\Delta x)}{Re_\tau} + 0.5 = 0.330(H/\Delta x)(CFL)Re_\tau^{-1.1296} + 0.5 \tag{2.22}$$

For CPG formulation, the bulk velocity changes in time. The mean bulk velocity is averaged over the sufficient time interval, then the skin-friction coefficient is obtained by $C_f = \frac{2H(dp/dx)}{\rho U_{b,avg}^2}$.

2.1.2.2 Constant Flow Rate (CFR)

(1) Set Re_b, $H/\Delta x$, CFL

(2) Approximate bulk velocity U_b

$$\frac{U_c}{c} = 1.28\frac{U_b}{c}(2Re_b)^{-0.0116} \tag{2.23}$$

which is used to compute the target bulk velocity

$$\frac{U_{b,tar}}{c} = \frac{u_c/c}{1.28}(2Re_b)^{0.0116} \tag{2.24}$$

$$\frac{U_{b,tar}}{c} = \frac{U_c/c}{1.28}(2Re_b)^{0.0116} = \frac{CFL}{1.28}(2Re_b)^{0.0116} \tag{2.25}$$

(3) Determine kinematic viscosity and relaxation time

$$\frac{\nu\Delta t}{\Delta x^2} = \frac{U_b H}{Re_b}\frac{\Delta t}{\Delta x^2} = \frac{(U_b/c)(H/\Delta x)}{Re_b} = \frac{H/\Delta(CFL)}{1.2697Re_b^{0.9884}} \tag{2.26}$$

$$\frac{\tau}{\Delta t} = \frac{3\nu\Delta t}{\Delta x^2} + 0.5 = \frac{3(U_b/c)(H/\Delta x)}{Re_b} + 0.5 = \frac{3(H/\Delta x)(CFL)}{1.2697Re_b^{0.9884}} + 0.5 \tag{2.27}$$

For CFR formulation, the pressure gradient changes in time. The mean pressure gradient is averaged over the sufficient time interval, then the skin-friction coefficient is obtained by $C_f =$

$\frac{2H(dp/dx)_{avg}}{\rho U_{b,tar}^2}$.

2.1.3 Grid-embedding Technique

Grid-embedding technique has been employed to improve the numerical accuracy near the walls, maintaining the computational cost at a reasonable level. In this proposed study, the multi-domain method is adopted due to the benefits from better management of CPU performances and higher memory savings Lagrava *et al.* (2012). The coarser grids are replaced by conformal patches of fine grids near wall region as shown in figure 2.2. The flow quantities such as fluid density, velocity, and kinematic viscosity are continuous across the grids by keeping the lattice speed constant on both grids, $\boldsymbol{c} = \Delta x_c/\Delta t_c = \Delta x_f/\Delta t_f$. The subscripts c and f indicate the coarse and fine grids, respectively. The coarse grid quantities can be scaled to find grid quantities via the grid-embedding ratio, $GR = \Delta x_c/\Delta x_f = \Delta t_c/\Delta t_f$. For the coarse grid, LB equation is advanced from time t to the time $t + \Delta t$. For the fine grid, LB equation is advanced from time $t + \Delta t/GR, t + 2\Delta t/GR, ..., t + \Delta t$. On transition between the coarse and fine grids, the fluid density, velocity and non-equilibrium distribution functions are transferred. The find grid is extended to the second layer of the coarse grid, whereas the coarse grid is extended to $GR + 1$ layer of the fine grid, as shown in figure 2.2(b). Data is directly copied from coarse to fine grids at the corresponding site, while data should be interpolated in order to complete the missing information at the fine grids which are not existing at the corresponding site. For temporal interpolation, the second order Hermite interpolation is adopted between the times $t - \Delta t$ and $t + \Delta t$. For spatial interpolation, the second order bi-cubic interpolation is used. The distribution functions on both grids are reconstructed at the grid interfaces,

$$f_{i,f}(\boldsymbol{x}, t) = f_i^{eq}(\boldsymbol{x}, t) + \frac{\omega_c}{(GR)\omega_f} f_{i,c}^{neq}(\boldsymbol{x}, t), \tag{2.28}$$

$$f_{i,c}(\boldsymbol{x}, t) = f_i^{eq}(\boldsymbol{x}, t) + \frac{(GR)\omega_f}{\omega_c} f_{i,f}^{neq}(\boldsymbol{x}, t), \tag{2.29}$$

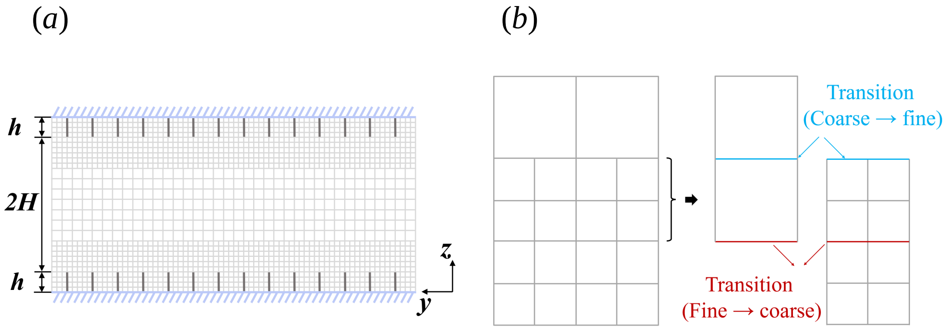

Figure 2.2: (*a*) Schematic of the computational grid in $y-z$ plane, and (*b*) the grid transitions at the grid interface with grid-embedding ratio of $GR=2$.

where ω is the relaxation frequency which corresponds to the inverse of relaxation time, $\omega = \Delta t/\tau$. Note that rescaling $f_i^{eq}(\boldsymbol{x}, t)$ is not necessary since it only depends on fluid density and velocity, which are continuous across the grids. On the other hand, the non-equilibrium part is proportional to the gradient of the velocity, therefore it is necessary to rescale it when transferring it between grids with different resolution Lagrava *et al.* (2012). This rescaling between the grids enables a continuous transition of the fluid quantities at the grid interfaces.

2.2 Solid Solver

2.2.1 Governing Equation of Motion of Deformable/slender Filaments

This section outlines the numerical method employed to solve the governing equation of motion of the hairy filament. As mimicking the mammalian hairs (e.g. seal furs) or bird feather fibers, transverse shear deformation and rotational bending are negligible. Thus, it can be assumed that the motion of the filaments is described by the dynamic Euler-Bernoulli beam equation resulting from the Euler-Bernoulli beam theory rather than the Timoshenko–Ehrenfest beam theory. The equation of motion is derived through the principle of least action, regarding the variational derivative of the action integral of the Lagrangian, $\mathcal{L}$ (Goldstein *et al.*, 2002). The resulting equation is then non-dimensionalized to ensure consistency in the bending rigidity and tension coefficient of the filaments during the parametric study. The dimensionless beam equation is solved with a second-order central difference scheme in both space and time.

The governing equation of motion of the hairy filament can be simply derived by finding a stationary point of the action integral of $\mathcal{L}$ with respect to time. $\mathcal{L}$ is defined by the difference of kinetic energy of a dynamical system from its potential energy. Regarding a hairy filament as a dynamical system, $\mathcal{L}$ can be written as

$$\mathcal{L} = \int_\Gamma \frac{\Delta\rho}{2}\boldsymbol{U}^2 ds - \int_\Gamma \left[K_b \left(\frac{d^2\boldsymbol{X}}{ds^2}\right)^2 + \frac{T}{2}\left(\frac{d\boldsymbol{X}}{ds}\right)^2 \right] ds - \int_\Gamma \boldsymbol{F}_{IBS}\boldsymbol{X} ds + \int_\Gamma \boldsymbol{F}_c \boldsymbol{X} ds, \quad (2.30)$$

where $\Delta\rho \equiv (\rho_s - \rho_f A_0)$ is the linear density difference between the filaments and the surrounding fluid, where ρ_s denotes the linear density of the filament, ρ_f denotes the density of the fluid, and A_0 is the effective cross-sectional area of the filament in its initial, undeformed state. $\boldsymbol{U}(s,t) = d\boldsymbol{X}(s,t)/dt$ is the velocity of the Lagrangian marker. The terms present in the right-hand side represent the kinetic energy, the elastic potential energy, the works done by the forces from the fluid-structure interaction, filament-filament and filament-wall collisions. According to the principle of least action, the motion of the dynamical system from time 0 to t is such that the action integral has a stationary value for the actual path of the motion, and the variation of the action integral is zero (Goldstein *et al.*, 2002):

$$\mathcal{A} = \int_0^t \left[\int_\Gamma \frac{\Delta\rho}{2} \boldsymbol{U}^2 ds - \int_\Gamma \left[K_b \left(\frac{d^2\boldsymbol{X}}{ds^2} \right)^2 + \frac{T}{2} \left(\frac{d\boldsymbol{X}}{ds} \right)^2 \right] ds - \int_\Gamma \boldsymbol{F}_{IBS} \boldsymbol{X} ds + \int_\Gamma \boldsymbol{F}_c \boldsymbol{X} ds \right] dt, \tag{2.31}$$

$$\delta_{var} \mathcal{A} = 0. \tag{2.32}$$

Then, the resulting equation becomes the governing equation of motion of the filament,

$$\Delta\rho \frac{\partial^2 \boldsymbol{X}}{\partial t^2} = \frac{\partial}{\partial s} \left(T \frac{\partial \boldsymbol{X}}{\partial s} \right) - \frac{\partial^2}{\partial s^2} \left(K_b \frac{\partial^2 \boldsymbol{X}}{\partial s^2} \right) - \boldsymbol{F}_{IBS} + \boldsymbol{F}_c. \tag{2.33}$$

Here, the position vector of the Lagrangian markers on the filament is denoted by $\boldsymbol{X}(s,t) = [X(s,t), Y(s,t), Z(s,t)]$. The tension force along the filament axis is denoted by $T(s,t)$, and the bending rigidity is denoted by K_b. In this study, small elongation of the filaments, less than 1%, was allowed by setting the dimensionless stretching coefficient to $K_s/(\Delta\rho U_b^2 h_0^2) = 1$, where U_b is the bulk velocity in the channel, and h_0 is the height of the filament at its initial, undeformed state. The interaction force per unit length exerted on the filament by the surrounding fluid is denoted by $\boldsymbol{F}_{IBS}(s,t)$. The repulsive force, $\boldsymbol{F}_c$, from the filament-to-filament or filament-to-wall collision is introduced to prevent the filaments from crossing each other or crossing the channel walls while deforming.

The filaments are modeled with a free end at their tips and a clamped end at their roots. The boundary conditions at the free end are (Huang *et al.*, 2007)

$$T(s_{tip}, t) = 0, \frac{\partial^2 \boldsymbol{X}(s_{tip}, t)}{\partial s^2} = 0, \frac{\partial^3 \boldsymbol{X}(s_{tip}, t)}{\partial s^3} = 0, \tag{2.34}$$

and the boundary conditions at the clamped end are (Huang *et al.*, 2007)

$$\boldsymbol{X}(0,t) = \boldsymbol{X}(0,0), \frac{\partial \boldsymbol{X}(0,t)}{\partial s} = (0,0,\pm 1). \tag{2.35}$$

In equation 2.35, the positive (negative) signs are for the filaments mounted at the lower (upper) channel walls, respectively.

2.2.2 Dimensionless Governing Equation of Motion of Deformable/slender Filaments

A dimensionless form of the equation 2.33 can be obtained by multiplying by $h_0/\left(\Delta\rho U_b^2\right)$, where h_0 is the filament length in undeformed state:

$$\frac{\partial^2 \boldsymbol{X}^*}{\partial t^{*2}} = \frac{\partial}{\partial s^*}\left(T^* \frac{\partial \boldsymbol{X}^*}{\partial s^*}\right) - \frac{\partial^2}{\partial s^{*2}}\left(K_b^* \frac{\partial^2 \boldsymbol{X}^*}{\partial s^{*2}}\right) - \boldsymbol{F}^*_{IBS} + \boldsymbol{F}^*_c. \tag{2.36}$$

s^* is the dimensionless arc length (s/h_0); $\boldsymbol{X}^*$ is the dimensionless position of the I-th marker of a filament ($\boldsymbol{X}/h_0$); t^* the dimensionless time ($tU_{b,tar}/h_0$); T^* is the dimensionless tension force ($T^* \equiv K^* |\frac{\partial \boldsymbol{X}}{\partial s}| - 1$). The reference quantities used for the non-dimensionalization of stretching coefficient, bending rigidity, and Lagrangian forcing are $K_{s,ref} = \Delta\rho U_{b,tar}^2$ and $K_{b,ref} = \Delta\rho U_{b,tar}^2 h_0^2$, and $F_{ref} = \frac{\Delta\rho U_{b,tar}^2}{h_0}$, respectively. In this proposed study, dimensionless form is used to keep consistency in dealing with the stretching coefficient and bending rigidity. Moreover, the dimensionless forms allows for comparing the different sizes of systems in a consistent manner.

This study adopted a short-range repulsive force model proposed by Glowinski *et al.* (1999). In this model, the repulsive force has a non-zero value once the I-th Lagrangian marker of a filament is closed to the markers of the other neighboring filaments or to the channel walls within a distance of d_{cf} or d_{cw}, respectively. The resulting net force on the marker is given by

$\boldsymbol{F}^*_{c,I} = \boldsymbol{F}^{f*}_{c,I} + \boldsymbol{F}^{w*}_{c,I}$, where

$$\boldsymbol{F}^{f*}_{c,I} = \begin{cases} \sum_{J\neq I} K^*_c \left(\boldsymbol{X}^*_I - \boldsymbol{X}^*_J\right)\left(d^*_{IJ} - d^*_{cf}\right)^2, & \left(d^*_{IJ} \leq d^*_{cf}\right) \\ \boldsymbol{0}, & \text{(otherwise)} \end{cases} \tag{2.37}$$

$$\boldsymbol{F}^{w*}_{c,I} = \begin{cases} \pm K^*_c \left(Z^*_I - z^*_0\right)\left(d^*_{I0} - d^*_{cw}\right)^2, & \left(d^*_{I0} \leq d^*_{cw}\right) \\ \boldsymbol{0}, & \text{(otherwise)} \end{cases} \tag{2.38}$$

where $\boldsymbol{X}^*_I$ is the position of the I-th marker of a filament normalized by h_0; $\boldsymbol{X}^*_J$ is the position of the J-th marker of its neighboring filaments, normalized by h_0. $\boldsymbol{F}^{f*}_{c,I}$ is the dimensionless repulsive force exerted on the I-th Lagrangian marker of a filament by the J-th Lagrangian marker of its neighboring filaments; their dimensionless gap distance is denoted by $d^*_{IJ} = |\boldsymbol{X}_I - \boldsymbol{X}_J|/h_0$; $\boldsymbol{F}^{w*}_{c,I}$ is the dimensionless repulsive force exerted on the I-th Lagrangian marker of the filament by the channel wall; the dimensionless wall-normal distance between the marker and the channel wall is denoted by $d^*_{I0} = |Z_I - z_0|/h_0$; K^*_c is the dimensionless stiffness parameter, which is set to 1, appropriate enough to prevent the collisions between filament-filament as well as between filament-channel walls. In this study, marginal variation in the simulation results was observed once K^*_c is greater than 1. The repulsive force between Lagrangian markers and channel walls was limited to the wall-normal direction in this study, as shown in equation 2.38. In this study, d^{r*}_{cf} was set to $3\Delta^*$ to prevent overlapping the interpolation/spreading ranges of two or more filaments; d^{r*}_{cw} was set to $1.5\Delta^*$ to avoid overlapping the interpolation/spreading ranges of the filaments with the channel wall, where Δ^* is the dimensionless Eulerian grid size (Δ/h_0). The positive (negative) sign in equation 2.38 denotes the filament-wall collisions at the lower (upper) channel wall. The total repulsive force acting on the I-th Lagrangian marker of a filament turns out to be $\boldsymbol{F}^*_c = \boldsymbol{F}^{f*}_c + \boldsymbol{F}^{w*}_c$.

A staggered grid is used in Lagrangian coordinate system, as can be seen in figure 2.3.

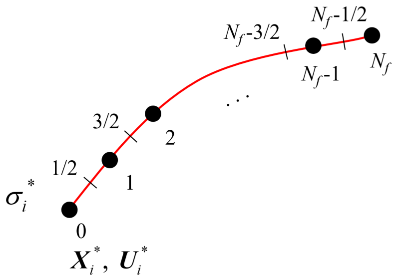

Figure 2.3: Schematic diagram of staggered grid along a filament. Tension force is defined on $s_{i+1/2}$. Solid position and velocity are defined on s_i.

Tension force is defined on the interfaces and the other Lagrangian variables are defined on the nodes.

$$\frac{\boldsymbol{X}_i^{*n+1} - 2\boldsymbol{X}_i^{*n} + \boldsymbol{X}_i^{*n-1}}{\Delta t^2} = \boldsymbol{F}_{t,i}^{*n} + \boldsymbol{F}_{b,i}^{*n} - \boldsymbol{F}_{IBS,i}^{*n} + \boldsymbol{F}_{c,i}^{*n} \tag{2.39}$$

$$\boldsymbol{X}_i^{*n+1} = 2\boldsymbol{X}_i^{*n} - \boldsymbol{X}_i^{*n-1} + \Delta t^2 \left(\boldsymbol{F}_{t,i}^{*n} + \boldsymbol{F}_{b,i}^{*n} - \boldsymbol{F}_{IBS,i}^{*n} + \boldsymbol{F}_{c,i}^{*n} \right) \tag{2.40}$$

where $\boldsymbol{F}_{t,i}^{*n}$ and $\boldsymbol{F}_{b,i}^{*n}$ indicate the dimensionless tension and bending forces, respectively, which are described by

$$\begin{aligned} \boldsymbol{F}_{t,i}^{*n} &= \frac{T_{i+1/2}^{*n} \frac{\boldsymbol{X}_{i+1}^{*n} - \boldsymbol{X}_i^{*n}}{\Delta s^*} - T_{i-1/2}^{*n} \frac{\boldsymbol{X}_i^{*n} - \boldsymbol{X}_{i-1}^{*n}}{\Delta s^*}}{\Delta s^*} \\ &= \frac{K_s^* \left(\frac{\boldsymbol{X}_{i+1}^{*n} - \boldsymbol{X}_i^{*n}}{\Delta s^*} - 1 \right) \frac{\boldsymbol{X}_{i+1}^{*n} - \boldsymbol{X}_i^{*n}}{\Delta s^*} - K_s^* \left(\frac{\boldsymbol{X}_i^{*n} - \boldsymbol{X}_{i-1}^{*n}}{\Delta s^*} - 1 \right) \frac{\boldsymbol{X}_i^{*n} - \boldsymbol{X}_{i-1}^{*n}}{\Delta s^*}}{\Delta s^*}, \end{aligned} \tag{2.41}$$

$$\begin{aligned} \boldsymbol{F}_{b,i}^{*n} &= -\frac{\frac{\boldsymbol{X}_{i+2}^{*n} - 2\boldsymbol{X}_{i+1}^{*n} + \boldsymbol{X}_i^{*n}}{\Delta s^{*2}} - 2 \frac{\boldsymbol{X}_{i+1}^{*n} - 2\boldsymbol{X}_i^{*n} + \boldsymbol{X}_{i-1}^{*n}}{\Delta s^{*2}} + \frac{\boldsymbol{X}_i^{*n} - 2\boldsymbol{X}_{i-1}^{*n} + \boldsymbol{X}_{i-2}^{*n}}{\Delta s^{*2}}}{\Delta s^{*2}} \\ &= -\frac{\boldsymbol{X}_{i+2}^{*n} - 4\boldsymbol{X}_{i+1}^{*n} + 6\boldsymbol{X}_i^{*n} - 4\boldsymbol{X}_{i-1}^{*n} + \boldsymbol{X}_{i-2}^{*n}}{\Delta s^{*4}}. \end{aligned} \tag{2.42}$$

The position of Lagrangian markers, $\boldsymbol{X}_i^{*n+1}$, is updated from equation 2.40 and then the filament velocity is updated in turn using the second order backward difference scheme,

$$\boldsymbol{U}_i^{*n+1} = \frac{3\boldsymbol{X}_i^{*n+1} - 4\boldsymbol{X}_i^{*n} + \boldsymbol{X}_i^{*n-1}}{2\Delta t}. \tag{2.43}$$

2.3 Fluid-hairy Structure Interaction

2.3.1 Immersed Boundary (IB) Method

Fluid-structure interaction (FSI) is a ubiquitous phenomenon that is widely observed in various engineering applications, spanning from aerospace (Airfoil and engine blade designs), biomedical (Heart valves, beating cilia, and drug particle transport) to civil (Flow over urban areas, bridges, and skyscrapers), ocean (Riser, offshore platform), and energy engineering (Wind turbines, marine hydrokinetic devices, nuclear fuel rods). Numerous numerical studies have been conducted to comprehend FSI. The immersed boundary (IB) method has gained popularity for FSI simulations. The IB method was first proposed by Peskin in 1972 (Peskin, 1972) to simulate flow patterns around heart valves. Later, a number of its variants have been proposed to conduct a variety of FSI simulations and improve the numerical accuracy, stability, and robustness. FSI simulation with IB methods has provided intuitive solutions to the problem and suggested promising measures to accomplish a desired system features in several engineering applications, such as separation control with flaps mounted on airfoils and hairy coatings on cylinders (Shan *et al.*, 2000; Favier *et al.*, 2009; Fang *et al.*, 2019; Mao *et al.*, 2022), turbulent skin-friction drag reduction with ribbed-surfaces (Garcia-Mayoral & Jimenez, 2011), convective heat transfer or mixing enhancement with flexible flaps in a heat sink channel (Park *et al.*, 2016; Lee *et al.*, 2017, 2018; Chen *et al.*, 2020), energy harvesting with an inverted piezoelectric flag (Ryu *et al.*, 2015; Shoele & Mittal, 2016).

The key feature of IB method is to separate the solution procedures of the fluid flow and the motion of a solid body by describing the fluid flow in an Eulerian coordinate and the motion of the solid body in a Lagrangian coordinate, respectively. The fluid and solid motions are coupled via the interaction forces, which are incorporated to each governing equation to satisfy the fundamental physical principles, Newton's third law. This method can bypass the need for a tedious re-meshing process for moving geometries at each time step, which is a laborious and computationally expensive process commonly required the body-fitted methods (e.g. arbitrary Lagrangian-Eulerian approach).

The IB framework is often characterized by two categories: Interface schemes and forcing schemes, which have emerged to improve the accuracy, stability, and robustness of FSI solvers. The interface schemes can be subdivided into sharp-interface and diffusive-interface schemes, while the forcing schemes can be subdivided into feedback-forcing and direct-forcing schemes. Further details on the interface and forcing schemes are presented in the following sections.

2.3.1.1 Interface Schemes: Sharp- and Diffusive-interface Schemes

In IB simulations, the locations of Lagrangian nodes (or markers) do not generally match with the locations of Eulerian nodes, requiring an appropriate interface scheme in order to satisfy the basic kinematic rules such as the no-slip, non-penetration along the IB. This interface scheme can be categorized to two types: Sharp-interface scheme and diffusive-interface scheme. Figure 2.4 show the schematic diagrams of the sharp- and diffusive-interface schemes. The sharp-interface scheme is generally used to impose the fluid quantities on the forcing points near the surface of solid body whose cross-sectional area or volume are not negligible but large enough to have a few grid points inside the solid body and distinguish them from the fluid nodes. The interaction force on the IB is computed by using information on the fluid quantities that are discontinuously distributed across this boundary, which is why this scheme is often called 'discrete' forcing scheme (Mittal & Iccarino, 2005). In contrast, the diffusive-interface scheme imposes the fluid quantities on the IB by interpolating fluid quantities from the neighboring fluid nodes to the IB. With an appropriate smooth function (e.g. smoothed delta function), the interaction force on the IB is computed by interpolating the fluid quantities that are distributed continuously across the boundary, which is why it is often called a continuous forcing scheme (Mittal & Iccarino, 2005). More details in the smoothed function for the interpolation of Eulerian quantities and the spreading of Lagrangian quantities will be discussed at the end of this section.

In the sharp-interface scheme, the interface between the fluid and the immersed structure is modeled as a sharp boundary (Mohd-Yusof, 1997; Fedlun *et al.*, 2000). Forcing points are placed on the Eulerian nodes closest to the interface, and fluid quantities at the forcing node are determined using an appropriate interpolation scheme in order to satisfy the basic kinematic conditions (e.g. no-slip and non-penetration) along the IB. While this method resulted in acceptable accuracy and stability for stationary, rigid solid bodies, it is vulnerable to numerical instability in the case of moving boundary problems. This is due to spurious oscillations resulting from temporal and spatial discontinuities at Eulerian nodes within the solid region during the previous time step, which become exposed to the fluid region at the subsequent time step. To address this issue, various remedies have been proposed such as ghost-cell, cut-cell, iterative/non-iterative strong fluid-structure coupling schemes (Luo *et al.*, 2008; Mittal *et al.*, 2008; Seo & Mittal, 2011; Yang *et al.*, 2008; Yang & Stern, 2015). Although these approaches improved the numerical stability, it is still doubtful that the sharp-interface is applicable for elastic, slender, dynamically deforming solid bodies, because assigning grid points inside the solid body and distinguishing them from fluid nodes are challenging for such bodies.

In the diffusive-interface scheme, the fluid velocity is interpolated from the surrounding Eulerian grids into Lagrangian markers along the IB, employing a smoothing technique of the interpolation procedure (e.g. employing a discrete smooth delta function). The interaction force is dependent on the difference between the interpolated fluid velocity and the Lagrangian marker's velocity, and the calculated interaction force is distributed into the adjacent Eulerian nodes via the same smoothing technique. This scheme has the advantage of mitigating numerical oscillations, making it more accurate and stable for moving boundaries in comparison to sharp-interface scheme (Uhlmann, 2005). With this advantage, the diffusive-interface is widely adopted for FSI problems, especially elastic, slender, dynamically deforming solid bodies. This suggests that the diffusive-interface scheme more sounds valid for the present study where the dynamics of hairy filaments and their effects on the modulation of turbulent channel flows are

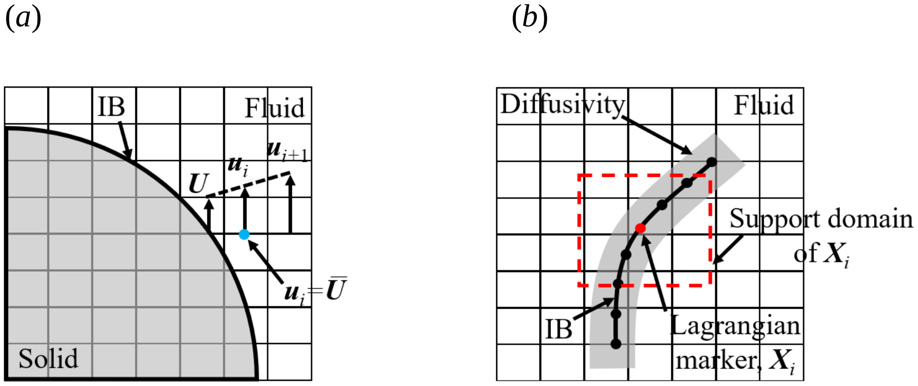

Figure 2.4: Schematic diagrams of (*a*) sharp-interface and (*b*) diffusive-interface schemes. (*a*) An example of velocity reconstruction method (Fedlun *et al.*, 2000) for a rigid, cylindrical solid body. $\bar{U}$ denotes the imposed velocity obtained from a linear approximation. (*b*) An example of an elastic, slender body with the support of the i^{th} Lagrangian marker in regards to 3-point discrete delta function (Roma *et al.*, 1999). The support denoted by the red-dashed box indicates the interpolation/spreading stencil. The gray shaded area denotes the diffusivity of the interface.

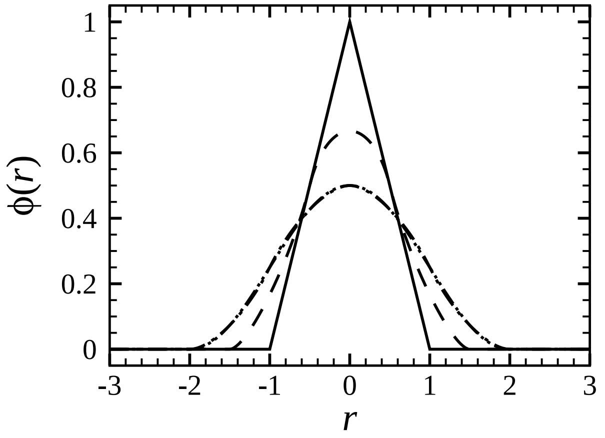

Figure 2.5: Distributions of one-dimensional continuous functions based on 2-point (Solid), 3-point (Dashed), 4-point-piecewise (Dashed-dot), 4-point-cosine (Dashed-dot-dot) smoothed delta functions.

investigated, as compared to the sharp-interface scheme.

In the framework of two-way coupling FSI simulation with the diffusive-interface scheme, the interpolation and force spreading are generally conducted by using a discrete smoothed delta function. In this scheme, the interpolation is conducted with a discrete smoothed delta function as present in figure 2.5. Its concept was first proposed by Peskin in 1972 for the smooth interpolation of the fluid velocity and the force spreading. Since then, several variants have been proposed, including 2-point discrete delta function, which corresponds to the bilinear interpolation in two dimensions and tri-linear interpolation in three dimension; 3-point discrete delta function (Roma *et al.*, 1999); 4-point cosine-type discrete delta function (Peskin, 1977); 4-point piecewise discrete delta function (Peskin, 2002); 6-point discrete delta function (Stockie, 1997). A choice of the discrete smooth delta function must be made properly since it affects the smoothness of the boundary and localization of interpolation/spreading. If the support size increases, the interpolation/spreading stencil become larger, thus the boundary becomes more diffusive, disabling to localize the interpolation/spreading operations and satisfy the no-slip condition accurately. Conversely, if the support size decreases, the interpolation/spreading stencil becomes too sharp, increasing the numerical instability. To achieve a balance between interface smoothness and numerical accuracy and stability, 3-point discrete smoothed delta function could be deemed a suitable compromise.

2.3.1.2 Forcing Schemes: Feedback- and Direct-forcing Schemes

The feedback-forcing IB method was pioneered by Peskin in 1972 for the simulation of blood flow in an elastic heart valve. Goldstein *et al.* (1993) developed the feedback-forcing scheme for numerical simulations of flow around a stationary rigid body. Later, the penalty IB method based on the feedback-forcing scheme were proposed to improve the numerical accuracy and stability (Kim & Peskin, 2007; Huang *et al.*, 2007; Huang & Sung, 2010), introducing the massless as well as massive boundaries that were linked together via virtual spring and damper.

In the feedback-forcing scheme, the interaction force exerted by fluid on solid was computed by Hook's law or proper feedback loops (Goldstein *et al.*, 1993; Saiki & Biringen, 1996; Huang *et al.*, 2007; Tian *et al.*, 2011), where the IB-related force is a function of the difference between the fluid velocity interpolated to a Lagrangian marker and the solid velocity at the marker. Then the computed force is distributed into the surrounding Eulerian grids. Although the feedback-forcing is simple and straightforward, the numerical accuracy and stability highly depend on the preconditioned virtual spring and damper constants (Shin *et al.*, 2008; Park *et al.*, 2016). Seeking a proper range of these constants requires *a priori* numerical experiments; however the range varies significantly depending on the flow conditions, geometries, time step, grid resolutions. Therefore, its less robustness leaves a suspicion that the feedback-forcing scheme is acceptable for numerical simulations requiring a systematic parametric study.

In contrast, the direct-forcing scheme obviates the arbitrariness resulting from the empirical constants. This scheme directly imposes the boundary conditions on the IB. This direct-forcing IB method was pioneered by Mohd-Yusof (1997); Fedlun *et al.* (2000) with a sharp-interface scheme. Later, Uhlmann (2005) combined the direct-forcing IB scheme with a diffusive-interface scheme. He showed that numerical instability resulting from the spurious oscillation was well suppressed along the IB, and thus numerical accuracy was improved. Although the direct-forcing scheme combined with a diffusive-interface showed a promise, it is still questionable whether it provides an acceptable basic kinematic rules, such as no-slip and non-penetration conditions along the IB. The no-slip along the IB is not often strictly fulfilled, because the force cannot be fully reconstructed after the interpolation and spreading operations (Gsell & Favier, 2021). This problem becomes more substantial for turbulent flows where the failure of the reconstruction provides a false velocity fluctuation field more significantly. Thus, a remedy is required to improve the basic kinematic condition in the framework of direct-forcing combined with diffusive-interface scheme, which will be discussed in the following sections.

2.3.2 LB-IB Method within the Framework of Diffusive-direct Forcing IB Scheme

2.3.2.1 Limitations of Previous Methods

The direct-forcing IB method, in combination with a diffusive-interface scheme, is commonly used for simulating the interaction between an elastic, slender body and a surrounding fluid flow in two-way coupled FSI simulations. This is because of its robustness and explicit implementation. However, the explicit nature of this procedure can give rise to slip-errors and flow penetration, which are contradictory to fundamental kinematic principles such as the no-slip and non-penetration conditions.

Several implicit methods have been proposed to overcome this problem. (Luo *et al.*, 2007; Kang & Hassan, 2011; Kempe & Fröhlich, 2012) proposed the multi-direct-forcing IB method for IB-NS and IB-LB simulations. In this approach, the direct-forcing is proceeded multiple times at sub-iteration steps until the slip-error reduces within a predefined criterion. Wu & Shu (2009) proposed IB-LB method based on the implicit velocity correction method. In this method, the interaction force imposed on the IB is set as unknown rather than pre-calculated and it is determined after the no-slip along the IB is enforced implicitly. Although these implicit forcing schemes suppressed the slip-error and flow penetration, it becomes much more computationally expensive when the number of immersed solid bodies increases. The implicit implementation should be taken into account for each Lagrangian marker along a number of immersed bodies at each time step. Furthermore, it relied on a solution procedure of linear matrix equation that brings about an additional implementation effort. Therefore, it is evident that an explicit formulation is still desired to maintain the computational costs and the implementation efforts within reasonable limits while making an effort to fulfill the no-slip and non-penetration conditions.

An explicit approach to fulfill the fundamental kinematic rules can be achieved by ensuring the reciprocity of interpolation-spreading operations. Pinelli *et al.* (2010) introduced a correcting parameter involved in the spreading operator to ensure the reciprocity. The main idea is that a Lagrangian quantity should be reproduced after consecutive procedures of spreading and interpolation,

$$\Psi(s,t) = I\left[S\left[\Psi(s,t)\right]\right], \tag{2.44}$$

where $I[\ ]$ and $S[\ ]$ denote the interpolation and spreading operators, respectively, also represented by

$$\Psi(s,t) = I\left[\psi(\boldsymbol{x},t)\right] = \int_\Omega \psi(\boldsymbol{x},t)\delta(\boldsymbol{X}-\boldsymbol{x})d\boldsymbol{x}, \tag{2.45}$$

$$\psi(\boldsymbol{x},t) = S\left[\Psi(s,t)\right] = \int_\Gamma \Psi(s,t)\delta(\boldsymbol{X}-\boldsymbol{x})\varepsilon(s,t)ds, \tag{2.46}$$

where ε is the correcting parameter, $\Psi(s,t)$ is a Lagrangian quantity, $\psi(s,t)$ is an Eulerian quantity, $d\boldsymbol{x}$ is equivalent to the infinitesimal volume $\Delta V = \Delta x \Delta y \Delta z$ in three-dimensional Eulerian domain, Ω, and Γ is the Lagrangian domain. The local coordinate along the filament axis is denoted by s. $I\,[\,]$ is the interpolation operator of an Eulerian quantity, $S\,[\,]$ is the spreading operator of a Lagrangian quantity.

In this manner, Lagrangian forcing, $\boldsymbol{F}_{IB}(s,t)$, exerted on solid by fluid, and momentum forcing, $\boldsymbol{f}_{IB}(\boldsymbol{x},t)$, exerted on fluid by solid should also satisfy the reciprocity to maintain the forcings conserved during the interpolation/spreading operations. Then the Lagrangian quantity can be replaced by $\boldsymbol{F}_{IB}(s,t)$ in equation 2.44, and its discrete form can be expressed by

$$\boldsymbol{F}_{IB,q}(s_J,t) = \sum_K \alpha_{J,K}\varepsilon(s_K,t)\boldsymbol{F}_{IB,q}(s_K,t), \tag{2.47}$$

$$\alpha_{J,K} = \sum_{\boldsymbol{x}_{l,m,n}\in\Omega_J} \Delta s_K \delta(\boldsymbol{X}_J - \boldsymbol{x}_{l,m,n})\delta(\boldsymbol{X}_K - \boldsymbol{x}_{l,m,n})\Delta\boldsymbol{x}, \tag{2.48}$$

where the subscript $q = \{1,2,3\}$ denotes the $x, y,$ and z directions, Ω_J is the interpolation/spreading window of J-th marker of a filament, $\boldsymbol{x}_{l,m,n}$ is the location of Eulerian grids within Ω_J as shown in figure 2.6. In this study, $\delta(\boldsymbol{X}-\boldsymbol{x})$ is 3-point smoothed delta function,

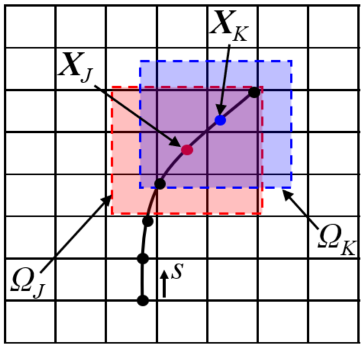

Figure 2.6: A schematic diagram of the compact supports for J-th and K-th Lagrangian markers. Their positions are denoted by $\boldsymbol{X}_J$ and $\boldsymbol{X}_K$, respectively. The corresponding compact supports are denoted by red and blue shaded areas, Ω_J and Ω_K, respectively. The support size corresponds to the size of the interpolation/spreading stencil of 3-point smoothed delta function (Roma *et al.*, 1999).

comprising the product of 1D delta functions at each direction (Roma *et al.*, 1999),

$$\delta(\boldsymbol{X}-\boldsymbol{x}) = \frac{1}{\Delta x \Delta y \Delta z}\phi\left(\frac{|X-x|}{\Delta x}\right)\phi\left(\frac{|Y-y|}{\Delta y}\right)\phi\left(\frac{|Z-z|}{\Delta z}\right) \tag{2.49}$$

with

$$\phi(r) = \begin{cases} \frac{1}{3}\left(1+\sqrt{-3r^2+1}\right), & (0<r<0.5) \\ \frac{1}{6}\left(5-3|r|-\sqrt{-3(1-|r|)^2+1}\right), & (0.5<r<1.5) \\ 0, & \text{otherwise} \end{cases} \tag{2.50}$$

where r is the gap distance between a Lagrangian marker and its adjacent Eulerian grids, normalized by the size of the local Eulerian grid.

It is noteworthy that the correcting parameter maintains the dimensional equality during the spreading operation. The dimension of the correcting parameter is the same as either the dimension of the square of the grid resolution ($\varepsilon \sim \Delta^2$) for one-dimensional solid body in three-dimensional flow or the dimension of the grid resolution for two-dimensional solid body in three-dimensional flow and one-dimensional solid body in two-dimensional flow ($\varepsilon \sim \Delta$). This is why it is often referred to as 'hydrodynamic area' for the former or 'hydrodynamic thickness' for the latter (Pinelli *et al.*, 2010; Favier *et al.*, 2014; Li *et al.*, 2016; Jiang & Liu, 2019).

Accurate evaluation of the correcting parameter is responsible for ensuring the reciprocity of interpolation-spreading operations and thus the no-slip and non-penetration conditions along the IB. For examples of rigid cylinders or rigid slender plates with their pre-described velocity, Pinelli *et al.* (2010) assumed that the forcings distributed along the IB remain constant, leading to $\boldsymbol{F}_q(s_J, t) = \boldsymbol{F}_q(s_K, t)$. In this assumption, the equation 2.47 can be reduced to

$$\boldsymbol{1} = \sum_k \alpha_{J,K} \varepsilon(s_K, t), \tag{2.51}$$

and its a matrix equation form is expressed by

$$\underline{\underline{A}} \begin{bmatrix} \varepsilon(s_0, t) \\ \varepsilon(s_1, t) \\ \dots \\ \\ \varepsilon(s_{N_F}, t) \end{bmatrix} = \begin{bmatrix} 1 \\ 1 \\ \dots \\ \\ 1 \end{bmatrix}. \tag{2.52}$$

where the coefficients of the matrix $\underline{\underline{A}}$ are denoted by $\alpha_{J,K}$ in the equation 2.48, and $s_0, \dots, s_{N_F}$ denote the Lagrangian markers along the IB. This matrix equation can be solved to obtain $\varepsilon(s, t)$, which can be subsequently incorporated into the spreading operator whilst maintaining the dimensional equality during the force spreading. With this approach, Pinelli *et al.* (2010) showed reasonable numerical accuracy with an improvement of no-slip along the IB and the range of applicability of the proposed methodology for stationary and moving rigid solid bodies. Although this approach showed a promise to fulfill the no-slip on IB, few drawbacks were found in this study.

First, a slender filament located with a certain position in relative to the surrounding Eulerian grids can result in a set of coefficients of A matrix that leads to a zigzag distribution of $\varepsilon(s, t)$

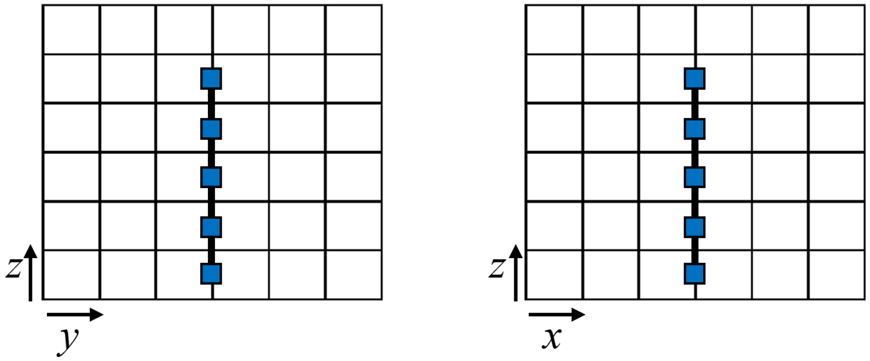

Figure 2.7: An example of a rigid, slender filament positioned at Eulerian grids in the x and y directions and at the halfway of Eulerian grids in the z direction, respectively. The filament is uniformly discretized with 5 Lagrangian markers.

along the IB. Assume that a slender rigid filament is located as shown in figure 2.7. In this example, the Lagrangian markers are located at the Eulerian grid points in the x and y directions, but located at the center of grid cell in the z direction. To evaluate the first coefficient, $\alpha_{0,0}$, of $\underline{\underline{A}}$, a set of Eulerian grid points involved in the interpolation/spreading support of the 0-th marker can be found as denoted by circular symbols in figure 2.8(*a*). Each circular symbol denoted in figure 2.8(*a*) indicates the Eulerian grid points included in the support of the 0-th Lagrangian marker, which is denoted by the blue-colored, square-shaped symbol. The resulting coefficient, $\alpha_{0,0}$, can then be obtained from

$$\alpha_{0,0} = \sum_{\mathbf{x}_{l,m,n} \in \Omega_0} \Delta s_0 \delta(\boldsymbol{X}_0 - \mathbf{x}_{l,m,n}) \delta(\boldsymbol{X}_0 - \mathbf{x}_{l,m,n}) \Delta x^3 = \frac{\Delta s_0}{\Delta x^3} \beta_{0,0} \tag{2.53}$$

$$\begin{aligned} \beta_{0,0} &= \sum_{\mathbf{x}_{l,m,n} \in \Omega_0} \delta(\boldsymbol{X}_0 - \mathbf{x}_{l,m,n}) \delta(\boldsymbol{X}_0 - \mathbf{x}_{l,m,n}) \\ &= \sum_{\mathbf{x}_{l,m,n} \in \Omega_0} \phi\left(\frac{x_{l,m,n} - X_0}{\Delta x}\right) \phi\left(\frac{y_{l,m,n} - Y_0}{\Delta y}\right) \phi\left(\frac{z_{l,m,n} - Z_0}{\Delta y}\right) \\ &\phi\left(\frac{x_{l,m,n} - X_0}{\Delta x}\right) \phi\left(\frac{y_{l,m,n} - Y_0}{\Delta y}\right) \phi\left(\frac{z_{l,m,n} - Z_0}{\Delta z}\right). \end{aligned} \tag{2.54}$$

Then the breakdowns of $\beta_{0,0}$ can be expressed in terms of 4 green-, 4 red-, 8 yellow-, 2 skyblue-colored circular symbols denoted in figure 2.8(*a*) and obtained regarding non-zero outcomes,

$$\begin{aligned}\beta_{0,0} &= 4\phi(1)\phi(0)\phi(0.5)\phi(1)\phi(0)\phi(0.5) + 4\phi(0)\phi(1)\phi(0.5)\phi(0)\phi(1)\phi(0.5)\\ &+ 8\phi(1)\phi(1)\phi(0.5)\phi(1)\phi(1)\phi(0.5) + 2\phi(0)\phi(0)\phi(0.5)\phi(0)\phi(0)\phi(0.5)\\ &= 4\left(\frac{1}{6}\right)\left(\frac{2}{3}\right)\left(\frac{1}{2}\right)\left(\frac{1}{6}\right)\left(\frac{2}{3}\right)\left(\frac{1}{2}\right) + 4\left(\frac{2}{3}\right)\left(\frac{1}{6}\right)\left(\frac{1}{2}\right)\left(\frac{2}{3}\right)\left(\frac{1}{6}\right)\left(\frac{1}{2}\right)\\ &+ 8\left(\frac{1}{6}\right)\left(\frac{1}{6}\right)\left(\frac{1}{2}\right)\left(\frac{1}{6}\right)\left(\frac{1}{6}\right)\left(\frac{1}{2}\right) + 2\left(\frac{2}{3}\right)\left(\frac{2}{3}\right)\left(\frac{1}{2}\right)\left(\frac{2}{3}\right)\left(\frac{2}{3}\right)\left(\frac{1}{2}\right)\\ &= 0.125.\end{aligned} \tag{2.55}$$

Then $\alpha_{0,0} = 0.125\Delta s_0/\Delta x^3$ is obtained from the equations 2.53 and 2.55.

Similarly, $\alpha_{0,1}$ can also be obtained as followed,

$$\alpha_{0,1} = \sum_{\boldsymbol{x}_{l,m,n}\in\Omega_0} \Delta s_0 \delta(\boldsymbol{X}_0 - \boldsymbol{x}_{l,m,n})\delta(\boldsymbol{X}_1 - \boldsymbol{x}_{l,m,n})\Delta x^3 = \frac{\Delta s_1}{\Delta x^3}\beta_{0,1} \tag{2.56}$$

$$\begin{aligned}\beta_{0,1} &= \sum_{\boldsymbol{x}_{l,m,n}\in\Omega_0} \delta(\boldsymbol{X}_0 - \boldsymbol{x}_{l,m,n})\delta(\boldsymbol{X}_1 - \boldsymbol{x}_{l,m,n})\\ &= \sum_{\boldsymbol{x}_{l,m,n}\in\Omega_0} \phi\left(\frac{x_{l,m,n} - X_0}{\Delta x}\right)\phi\left(\frac{y_{l,m,n} - Y_0}{\Delta y}\right)\phi\left(\frac{z_{l,m,n} - Z_0}{\Delta y}\right)\\ &\phi\left(\frac{x_{l,m,n} - X_1}{\Delta x}\right)\phi\left(\frac{y_{l,m,n} - Y_1}{\Delta y}\right)\phi\left(\frac{z_{l,m,n} - Z_1}{\Delta z}\right).\end{aligned} \tag{2.57}$$

The breakdowns of $\beta_{0,1}$ can be expressed in terms of 2 green-, 2 red-, 4 yellow-, 1 skyblue-colored circular symbols denoted in figure 2.8(*b*), and obtained regarding non-zero outcomes,

$$\begin{aligned}\beta_{0,0} &= 2\phi(1)\phi(0)\phi(0.5)\phi(1)\phi(0)\phi(0.5) + 2\phi(0)\phi(1)\phi(0.5)\phi(0)\phi(1)\phi(0.5)\\ &+ 4\phi(1)\phi(1)\phi(0.5)\phi(1)\phi(1)\phi(0.5) + 1\phi(0)\phi(0)\phi(0.5)\phi(0)\phi(0)\phi(0.5)\\ &= 2\left(\frac{1}{6}\right)\left(\frac{2}{3}\right)\left(\frac{1}{2}\right)\left(\frac{1}{6}\right)\left(\frac{2}{3}\right)\left(\frac{1}{2}\right) + 2\left(\frac{2}{3}\right)\left(\frac{1}{6}\right)\left(\frac{1}{2}\right)\left(\frac{2}{3}\right)\left(\frac{1}{6}\right)\left(\frac{1}{2}\right)\\ &+ 4\left(\frac{1}{6}\right)\left(\frac{1}{6}\right)\left(\frac{1}{2}\right)\left(\frac{1}{6}\right)\left(\frac{1}{6}\right)\left(\frac{1}{2}\right) + 1\left(\frac{2}{3}\right)\left(\frac{2}{3}\right)\left(\frac{1}{2}\right)\left(\frac{2}{3}\right)\left(\frac{2}{3}\right)\left(\frac{1}{2}\right)\\ &= 0.0625.\end{aligned} \tag{2.58}$$

Then $\alpha_{0,1} = 0.0625\Delta s_0/\Delta x^3$ is obtained from the equations 2.56 and 2.58.

In similar fashion, the other coefficients, $\alpha_{J,K}$, can be calculated and filled in $\underline{\underline{A}}$. In this example, the indices vary from 0 to 4, $J = 0, ..., 4$ and $K = 0, ..., 4$. The resulting linear matrix equation (Equation 2.52) becomes

$$\begin{bmatrix} 0.125 & 0.0625 & 0 & 0 & 0 \\ 0.0625 & 0.125 & 0.0625 & 0 & 0 \\ 0 & 0.0625 & 0.125 & 0.0625 & 0 \\ 0 & 0 & 0.0625 & 0.125 & 0.0625 \\ 0 & 0 & 0 & 0.0625 & 0.125 \end{bmatrix} \begin{bmatrix} \varepsilon(s_0, t) \\ \varepsilon(s_1, t) \\ ... \\ \\ \varepsilon(s_4, t) \end{bmatrix} = \begin{bmatrix} 1 \\ 1 \\ ... \\ \\ 1 \end{bmatrix} \tag{2.59}$$

This matrix equation can be solved for $\varepsilon(s, t)$ by using an appropriate linear solver (e.g. LU decomposition). $\varepsilon(s, t)$ obtained from the equation above ends up having a zigzag distribution as shown in figure 2.9. This zigzag distribution of ε is incorporated into the spreading operator, leading to the force distribution which is no longer continuous along the IB and eventually exacerbating the numerical stability.

As a remedy, a modification was made to the spreading operator by proposing a uniform distribution of the correcting parameter along the IB based on the averaging their local values over the IB (Jiang & Liu, 2019). This involved calculating $\bar{\varepsilon}(t)$ as the sum of $\varepsilon(s, t)$ for s_0 to s_{N_f}, divided by $(N_f + 1)$, giving $\bar{\varepsilon}(t) = \sum_{s_0}^{s_{N_f}} \varepsilon(s, t)/\left(N_f + 1\right)$. The resulting $\bar{\varepsilon}(t)$ was then used in place of the local correcting parameter $\varepsilon(s, t)$ in the spreading operator (Equation 2.46). However, this strategy does not provide the accurate no-slip condition along the IB, but result in huge slip-errors as it violates the mathematical formulation of reciprocity, as will be shown in Section 2.7.5.

Second, the assumption made in the previous study (Pinelli *et al.*, 2010), that the interaction force distributed along the IB is constant, $\boldsymbol{F}q(s_J, t) = \boldsymbol{F}q(s_K, t)$, is no longer valid when dealing with an elastic, slender body interacting with non-uniform flows. To illustrate this

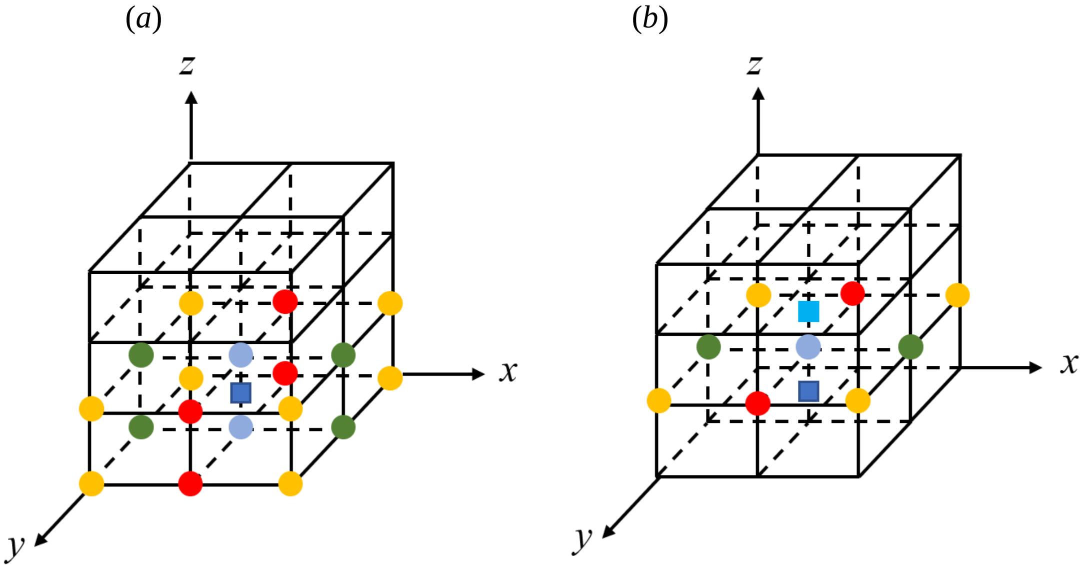

Figure 2.8: (*a*) Blue-colored, square-shaped symbol denotes the 0-th Lagrangian marker. Circle-shaped symbols denote the Eulerian grid points included in both supports of the 0-th marker and the same 0-th marker. The resulting $\alpha_{0,0}$ is obtained by summing up the outcome of the continuous functions, $\sum_{\mathbf{x}_{l,m,n}\in\Omega_0}\delta(\boldsymbol{X}_0-\mathbf{x}_{l,m,n})\delta(\boldsymbol{X}_0-\mathbf{x}_{l,m,n})$. (*b*) Blue-colored, square-shaped symbol and skyblue-colored, square-shaped symbol denote the 0-th and 1st Lagrangian markers, respectively. Circle-shaped symbols denote the Eulerian grid points included in both supports of the 0-th marker and the 1st marker. The resulting $\alpha_{0,1}$ is obtained by summing up the outcome of the continuous functions, $\sum_{\mathbf{x}_{l,m,n}\in\Omega_0}\delta(\boldsymbol{X}_0-\mathbf{x}_{l,m,n})\delta(\boldsymbol{X}_1-\mathbf{x}_{l,m,n})$.

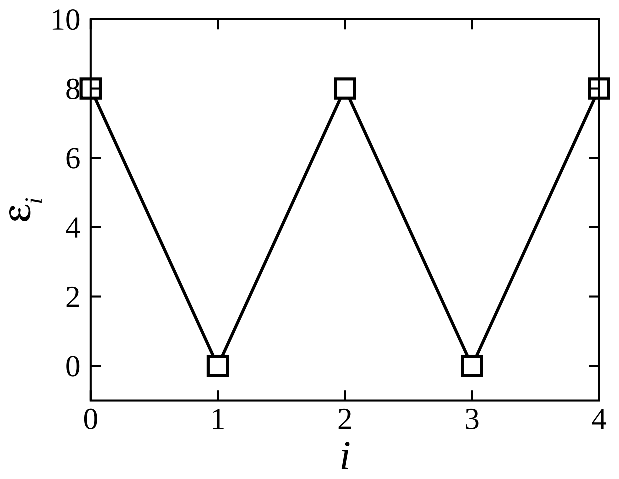

Figure 2.9: The distribution of ε, resulted from the previous approach (Pinelli *et al.*, 2010), for the example of the rigid, slender filament, discretized with 5 Lagrangian markers.

point, consider two different geometries: The flow over a rigid cylindrical solid body and the flow over an elastic, slender solid body, as shown in Figure 2.10. While the assumption may be acceptable for a rigid solid body, which can be assumed to be a lumped body sharing the same velocity and forcings across the Lagrangian markers, this is no longer valid for an elastic, slender body. The velocities interpolated into individual Lagrangian markers are different, resulting in different magnitudes and directions of the interaction forces at each Lagrangian marker, $\boldsymbol{F}q(s_J, t) \neq \boldsymbol{F}q(s_K, t)$. Therefore, it is prohibitive to maintain the oversimplified assumption, although the assumption continues to be used in their successors (Favier *et al.*, 2014; Li *et al.*, 2016; Jiang & Liu, 2019; O'Connor & Revell, 2019).

Although the previous efforts to meet the no-slip condition along the IB have mitigated the slip-error and flow penetration within a tolerable limit, these attempts still need to be extended to satisfy the no-slip more rigorously, especially for elastic, slender bodies interacting with highly fluctuating, non-uniform flows. This is important for the present study because the field of turbulent channel flow over the flexible filamentous surfaces is quite sensitive to the slip-error near the channel walls. Thus, the simulation results would be no longer reliable without a rigorous formulation. Furthermore, there is yet to be a theoretical analysis explaining the failure of reciprocal interpolation-spreading operations for elastic, slender IB, and suggesting its remedy within the framework of diffusive direct-forcing IB scheme.

2.3.2.2 A New LB-IB Method with Improved Reciprocity of Interpolation-spreading Operations

This study proposes a precise interpolation-spreading procedure that rigorously satisfies the reciprocity of the interpolation-spreading operations for elastic, slender IB and significantly reduces the slip-error. The proposed approach involves combining the correcting parameter with Lagrangian forcing at the same Lagrangian node, expressed as $\boldsymbol{F}_{IBS}(s, t) = \varepsilon(s, t)\boldsymbol{F}_{IB}(s, t)$.

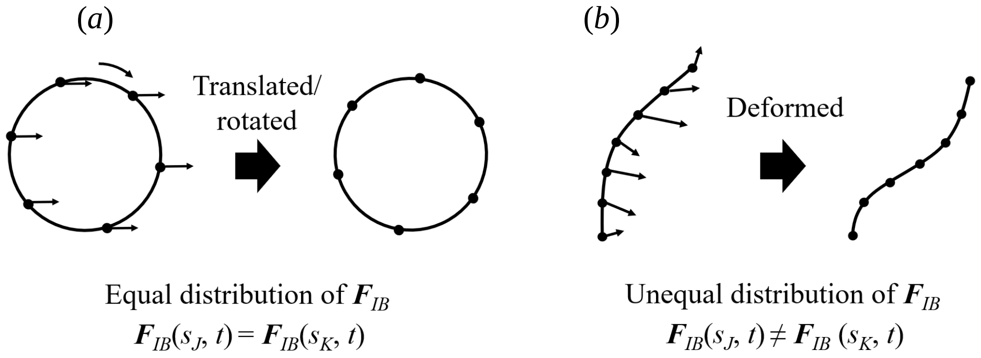

Figure 2.10: (*a*) Schematic diagram of the equally distributed Lagrangian forcing along the IB for example of a rigid, cylindrical solid body in a uniform flow. The uniformity of the Lagrangian forcing was resulted from the assumption, $\boldsymbol{F}_{IB}(s_J, t) = \boldsymbol{F}_{IB}(s_K, t)$. (*b*) Schematic diagram of the non-equally distributed Lagrangian forcing along the IB for example of an elastic, slender solid body in non-uniform flows. The Lagrangian forcings varies along the IB, which is more realistic and rigorous.

This allows for rewriting the equation 2.47 as

$$\boldsymbol{F}_{IB,q}(s_J, t) = \sum_K \alpha_{J,K} \varepsilon(s_K, t) \boldsymbol{F}_{IB,q}(s_K, t) = \sum_K \alpha_{J,K} \boldsymbol{F}_{IBS,q}(s_K, t). \tag{2.60}$$

The reformulated equation explains that the interaction force per unit volume is converted to the interaction force per unit length for the one-dimensional filament immersed in three-dimensional fluid flow through the straightforward correction. The discrete equation above can be expressed by a matrix form,

$$\underline{\underline{A}} \begin{bmatrix} F_{IBS,q}(s_0, t) \\ F_{IBS,q}(s_1, t) \\ \dots \\ \\ F_{IBS,q}(s_{N_F}, t) \end{bmatrix} = \begin{bmatrix} F_{IB,q}(s_0, t) \\ F_{IB,q}(s_1, t) \\ \dots \\ \\ F_{IB,q}(s_{N_F}, t) \end{bmatrix}. \tag{2.61}$$

Note that this matrix equation is distinct from the matrix equation derived from the previous study (Equation 2.52). The difference results from excluding the oversimplified assumption that the interaction force is uniform along the IB. The reformulated matrix equation can be solved for $\boldsymbol{F}_{IBS}(s,t)$, which can be subsequently incorporated to the spreading operator with a revised form,

$$\boldsymbol{f}_{IB}(\boldsymbol{x},t) = S\left[\boldsymbol{F}_{IB}(s,t)\right] = \int_{\Gamma} \boldsymbol{F}_{IBS}(s,t)\delta(\boldsymbol{X}-\boldsymbol{x})ds. \tag{2.62}$$

Unlike the previous methods (Pinelli *et al.*, 2010; Favier *et al.*, 2014; Li *et al.*, 2016; Jiang & Liu, 2019), this approach avoids numerical instability resulting from the zigzag distribution of $\varepsilon(s,t)$ and the oversimplified assumption used for the rigid solid body. This is accomplished by solving the linear equation 2.62, derived rigorously from the reciprocity of interpolation-spreading operations.

2.3.2.3 IB-LB Coupling

The IB-LB coupling scheme centers around the computation of interaction forcings and their allocation into the governing equations of solid and fluid. In this study, the direct-forcing IB scheme (Li *et al.*, 2016) is utilized to compute the Lagrangian forcing, where the fluid velocity is directly imposed on the Lagrangian marker through interpolation. In this approach, the velocity-forcing relation described in equation 2.13 can be expressed at the Lagrangian markers via interpolation procedures over the Eulerian variables, giving

$$I\left[\boldsymbol{f}_p(t) + \boldsymbol{f}_{IB}(\boldsymbol{x},t)\right] = \boldsymbol{F}_p(t) + \boldsymbol{F}_{IB}(s,t) = \frac{2}{\Delta t}\Big[I\left[\rho(\boldsymbol{x},t)\right]\boldsymbol{U}(s,t) - I\left[\rho(\boldsymbol{x},t)\boldsymbol{u}^{noF}(\boldsymbol{x},t)\right]\Big], \tag{2.63}$$

where $\boldsymbol{U}(s,t)$ is the velocity of a Lagrangian marker on the IB. Once the Lagrangian forcing is computed, it is distributed into the surrounding Eulerian grids via the spreading operator to update the momentum forcing field. Then the momentum forcing is consecutively incorporated into the LB equation via Guo's forcing (Equations 2.6 and 2.7, respectively).

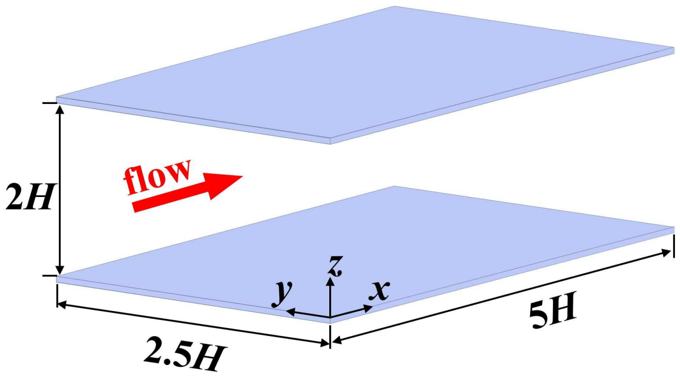

Figure 2.11: Schematic diagram of a turbulent channel

2.4 Maintaining a Constant Bulk Reynolds Number

2.4.1 Control Volume Analysis without IB Force

LB simulations of the pressure-driven channel flow can be carried out maintaining either constant pressure gradient (CPG) or constant flow rate (CFR). In this study, CFR formulation is adopted due to its advantages over CPG, which will be presented in Section 2.7. The mean pressure gradient is dynamically adjusted to keep bulk Reynolds number Re_b constant for all simulations and compare drag reductions at the same Re_b. Figure 2.11 shows a schematic diagram of a channel flow with periodicity in the streamwise (x)and spanwise (y) directions. No-slip boundary conditions are applied at the channel walls using half-way bounce back boundary condition Ladd (1994). The integral form of the momentum equation reads

$$\boldsymbol{F}_R(\mathbf{x},t) = \frac{\partial}{\partial t}\int_{CV} \rho(\mathbf{x},t)\boldsymbol{u}(\mathbf{x},t)\,dV, \tag{2.64}$$

where $\boldsymbol{F}_R$ denotes the resultant force, and the sum of momentum fluxes at control surfaces, $\int_{CS} \rho(\mathbf{x},t)\boldsymbol{u}(\mathbf{x},t)\{\boldsymbol{u}(\mathbf{x},t)\cdot d\boldsymbol{A}\}$, is zero due to the periodicity. A force equivalent to the resultant force should be applied to the flow in order to maintain a constant bulk Reynolds number. This force becomes equivalent to the pressure force accounting for the mean pressure gradient. Then the magnitude of the force should satisfy

$$\int_t^{t+\Delta t} \boldsymbol{F}_R(\boldsymbol{x},t)\,dt = \int_{CV} \rho(\boldsymbol{x},t)\boldsymbol{u}(\boldsymbol{x},t)\,dV|_{t+\Delta t} - \int_{CV} \rho(\boldsymbol{x},t)\boldsymbol{u}(\boldsymbol{x},t)\,dV|_t. \tag{2.65}$$

The first term in the right-hand side can be interpreted as the desired flow rate, which is represented by

$$\int_{CV} \rho(\boldsymbol{x},t)\boldsymbol{u}(\boldsymbol{x},t)\,dV|_{t+\Delta t} = (\rho U_{b,tar})\,L_x L_y(2H), \tag{2.66}$$

where $U_{b,tar}$ is the target bulk mean velocity that satisfies a constant Re_b. L_x and L_y denote the channel lengths in the periodic streamwise and spanwise directions, respectively, and $2H$ is the full channel height. The mean pressure gradient is imposed only in the streamwise direction. Equation 2.65 then can be rewritten in terms of the force per unit volume:

$$\int_t^{t+\Delta t} \boldsymbol{f}_p(t)\,dt = \rho U_{b,tar} - \frac{\int \rho(\boldsymbol{x},t)\boldsymbol{u}(\boldsymbol{x},t)\,dV}{\int dV}, \tag{2.67}$$

Using the second order explicit Adams-Bashforth integration, the left hand side of equation 2.67 can further be expanded to give

$$\frac{3\Delta t}{2}\boldsymbol{f}_p(t) - \frac{\Delta t}{2}\boldsymbol{f}_p(t-\Delta t) = \rho U_{b,tar} - \frac{\int \rho(\boldsymbol{x},t)\boldsymbol{u}(\boldsymbol{x},t)\,dV}{\int dV}. \tag{2.68}$$

Then the integrand in the right-hand side of the equation 2.68 can be reformed regarding the equation 2.11,

$$\frac{3\Delta t}{2}\boldsymbol{f}_p(t) - \frac{\Delta t}{2}\boldsymbol{f}_p(t-\Delta t) = \rho U_{b,tar} - \frac{\int \rho(\boldsymbol{x},t)\boldsymbol{u}^{noF}(\boldsymbol{x},t) + \frac{\Delta t}{2}\boldsymbol{f}_p(\boldsymbol{x},t)\,dV}{\int dV}. \tag{2.69}$$

Without introducing external forces other than the pressure force $\boldsymbol{f}_{ext}(\boldsymbol{x},t) = \boldsymbol{f}_p(t)$, the equation above becomes

$$\boldsymbol{f}_p(t) = \frac{1}{2\Delta t}\left[\rho U_{b,tar} - \frac{\int \rho(\boldsymbol{x},t)\boldsymbol{u}^{noF}(\boldsymbol{x},t)\,dV}{\int dV}\right] + \frac{1}{4}\boldsymbol{f}_p(t-\Delta t). \tag{2.70}$$

$f_p(t)$ is directly computed from equation 2.70 and then incorporated to equation 2.12 to update the fluid velocity field. Once the fluid variables are computed, the equilibrium distribution function is calculated from equation 2.4.

2.4.2 Control Volume Analysis in the Presence of IB Force

In the presence of an IB force, the form of the equation 2.70 should be reformed. The equation 2.69 derived from the control volume analysis can be rewritten as

$$\begin{aligned}\frac{3\Delta t}{2}\boldsymbol{f}_p(t) - \frac{\Delta t}{2}\boldsymbol{f}_p(t-\Delta t) &= \rho U_{b,tar} \\ &\quad - \frac{\int \rho(\boldsymbol{x},t)\boldsymbol{u}^{noF}(\boldsymbol{x},t) + \frac{\Delta t}{2}\boldsymbol{f}_p(t) + \frac{\Delta t}{2}\boldsymbol{f}_{IB}(\boldsymbol{x},t)\,dV}{\int dV},\end{aligned} \tag{2.71}$$

$$\begin{aligned}\frac{3\Delta t}{2}\boldsymbol{f}_p(t) - \frac{\Delta t}{2}\boldsymbol{f}_p(t-\Delta t) &= \frac{1}{\Delta t}\left[\rho U_{b,tar} - \frac{\int \rho(\boldsymbol{x},t)\boldsymbol{u}^{noF}(\boldsymbol{x},t)\,dV}{\int dV}\right] - \frac{1}{2}\frac{\int \boldsymbol{f}_p(\boldsymbol{x},t) + \boldsymbol{f}_{IB}(\boldsymbol{x},t)\,dV}{\int dV} \\ &= \frac{1}{\Delta t}\left[\rho U_{b,tar} - \frac{\int \rho(\boldsymbol{x},t)\boldsymbol{u}^{noF}(\boldsymbol{x},t)\,dV}{\int dV}\right] - \frac{1}{2}\frac{\int \boldsymbol{f}_p(\boldsymbol{x},t) + \boldsymbol{f}_{IB}(\boldsymbol{x},t)\,dV'}{\int dV} \\ &\quad - \frac{1}{2}\frac{\int \boldsymbol{f}_p(\boldsymbol{x},t)\,d(V-V')}{\int dV},\end{aligned} \tag{2.72}$$

where V is the entire volume of the channel, V' is the volume subject to the spreading operation of IB-forcing. Reorganizing the equation above in terms of $\boldsymbol{f}_p(\boldsymbol{x},t)$,

$$\begin{aligned}\boldsymbol{f}_p(t)\left[\frac{3}{2} + \frac{1}{2}\left(1 - \frac{\int dV'}{\int dV}\right)\right] &= \frac{1}{2}\boldsymbol{f}_p(t-\Delta t) \\ &\quad + \frac{1}{\Delta t}\left[\rho U_{b,tar} - \frac{\int \rho(\boldsymbol{x},t)\boldsymbol{u}^{noF}(\boldsymbol{x},t)\,dV}{\int dV}\right] \\ &\quad - \frac{1}{2}\frac{\int_{V'} S\left[\boldsymbol{F}_p(t) + \boldsymbol{F}_{IB}(s,t)\right]\,dV'}{\int dV}.\end{aligned} \tag{2.73}$$

The last term of the right-hand side can be achieved by directly taking into account the spreading operation over the outcome obtained from the equation 2.63. Once the pressure force is obtained from the equation 2.73, the Lagrangian forcing $\boldsymbol{F}_{IB}(s,t)$ is obtained by subtracting the pressure force from the outcome of the equation 2.63, $\boldsymbol{F}_{IB}(s,t) = [\boldsymbol{F}_p(t) + \boldsymbol{F}_{IB}(s,t)] - \boldsymbol{F}_p(t)$, then the calculation of the momentum forcing can be followed as, $\boldsymbol{f}_{IB}(\boldsymbol{x},t) = S\left[\boldsymbol{F}_{IB}(s,t)\right](\boldsymbol{x},t)$.

2.5 Overview of the Present IB-LB Coupling Algorithm

The details on the time advancing procedures for the present IB-LB coupling algorithm are shown in Algorithm 1 and figure 2.12.

Algorithm 1 IB-LB coupling algorithm

```
Require: $f_i(\boldsymbol{x},0)$, $\boldsymbol{X}(s,0)$, $\boldsymbol{X}(s,-1)$, $\boldsymbol{F}_{IB}(s,0)$, $\boldsymbol{f}_{IB}(\boldsymbol{x},0)$, and $\boldsymbol{f}_p(0)$ are given.
1: Calculate the fluid density, $\rho(\boldsymbol{x},0)$, and velocity, $\boldsymbol{u}(\boldsymbol{x},0)$ with equations 2.10 and 2.12.
2: Calculate the equilibrium distribution function, $f_i^{eq}(\boldsymbol{x},0)$, and forcing function, $G_i(\boldsymbol{x},0)$ with equations 2.4 and 2.7.
3: Calculate the fluid density, $\rho(\boldsymbol{x},1)$, and velocity, $\boldsymbol{u}^{noF}(\boldsymbol{x},1)$, with equations 2.10 and 2.11 once the distribution function, $f_i(\boldsymbol{x},1)$, is updated from collision and streaming steps (Equations 2.8 and 2.9).
4: Compute the tension force, $\boldsymbol{F}_t(s,0)$, from the equation 2.41. Compute the bending force, $\boldsymbol{F}_b(s,0)$, from the equation 2.42. Compute the repulsive force, $\boldsymbol{F}_b(s,0)$, from the equations 2.37 and 2.38. Prepare the interaction force, $\boldsymbol{F}_{IBS}(s,0)$, obtained at the previous time step of *step 8*.
5: Advance the dynamic Euler-Bernoulli beam equation by taking the 2nd order central difference methods in space and time. Obtain the position of Lagrangian markers, $\boldsymbol{X}(s,1)$, and velocity of Lagrangian markers, $\boldsymbol{U}(s,1)$ with equations 2.40 and 2.43.
6: Consider the lumped forces, $[\boldsymbol{F}_p(1)+\boldsymbol{F}_{IB}(s,1)]$. Individual terms cannot be obtained at this stage. Obtain $[\boldsymbol{F}_p(1)+\boldsymbol{F}_{IB}(s,1)]$ from the equation 2.63.
7: Obtain the pressure force from the equation 2.73.
8: Obtain the Lagrangian forcing, $\boldsymbol{F}_{IB}(s,1)$, by subtracting the pressure force, obtained from *step 7*, from the lumped forces, obtained from *step 6*. $\boldsymbol{F}_{IB}(s,1) = [\boldsymbol{F}_p(1)+\boldsymbol{F}_{IB}(s,1)] - \boldsymbol{F}_p(1)$
9: Update the fluid velocity, $\boldsymbol{u}(\boldsymbol{x},1)$ with equation 2.12 and go to Step 1 for the next time-step.
```

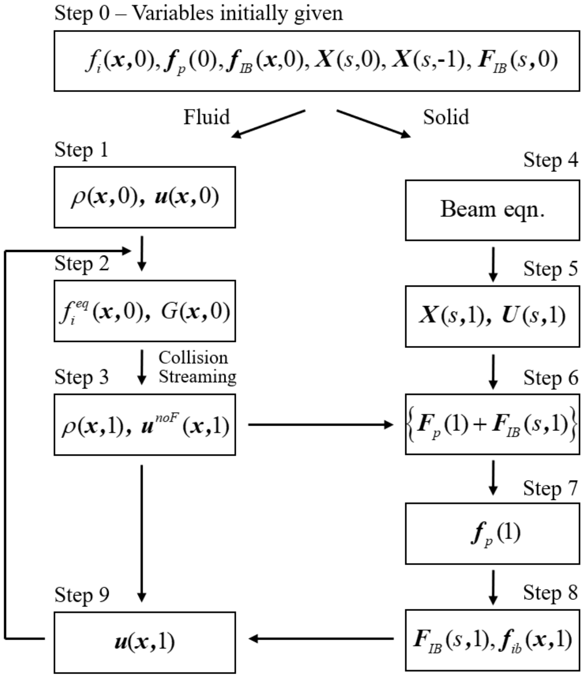

Figure 2.12: Main algorithm of the present IB-LB solution procedure

2.6 Domain Decomposition and Parallelization

A computational domain of turbulent channel flow is partitioned with a two dimensional ($x-y$) domain decomposition strategy as shown in figure 2.13. To perform the simulations, each sub-domains was assigned to a separate processor of a parallel computer. In this domain decomposition, the collision step is not affected due to its local nature of computational stencils. For the streaming step, however, the distribution functions leaving a sub-domain should be transferred to the neighboring sub-domain during a data transfer step using an appropriate MPI (Message passing interface) routines. In this study, non-blocking communication is adopted for data transfer between sub-domains in order to maximize the parallel performance by overlapping the communications with the computations. The parallel performance of the code was tested in a turbulent channel flow, corresponding to the geometry of the planned studies, both with grid embedding and without it. The numerical simulations were performed in channel of size $5H \times 2.5H \times 2H$ in the streamwise, spanwise, and wall-normal directions, respectively, at a

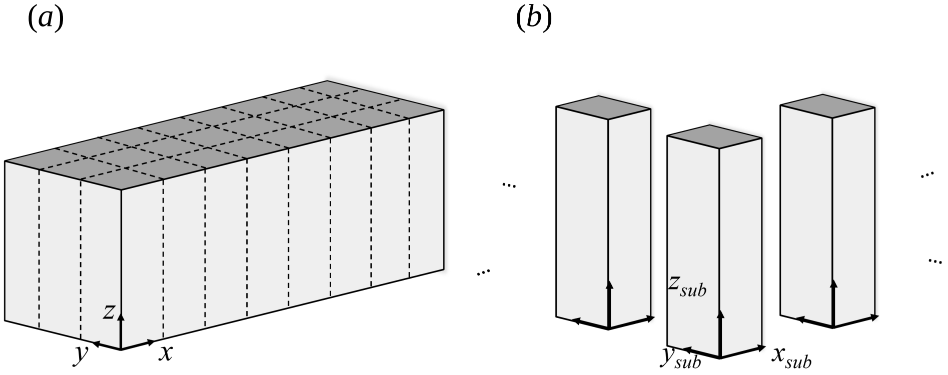

Figure 2.13: (*a*) The global computational domain of turbulent channel flow partitioned with $x-y$ domain decomposition. (*b*) Each chunk of sub-domain is assigned to a separate processor of a parallel computer.

bulk Reynolds number of $Re_b = 3600$ corresponding to $Re_\tau = u_\tau H/\nu \approx 221$. The simulations without grid embedding were performed with resolutions of $512 \times 256 \times 223$, in the streamwise, spanwise and wall-normal directions, respectively, corresponding to a uniform grid spacing of $\Delta x^{+0} \approx 2$ wall units in all three directions. For $GR = 2$, a grid spacing of $\Delta x_c^{+0} \approx 2$ wall units on the coarse grid, and $\Delta x_f^{+0} \approx 1$ wall units on the fine grid were used. For $GR = 4$, a grid spacing of $\Delta x_c^{+0} \approx 2$ wall units on the coarse grid, and $\Delta x_f^{+0} \approx 0.5$ wall units on the fine grid were used.

Figure 2.14 show the results of the tests for the parallel performance of LB code on Stampede2 of Texas Advanced Computing Center (TACC). The CPU time spent per each time step of the simulation drops linearly with the number of processors for non-grid embedding, $GR = 2$, and $GR = 4$, as shown in figure 2.14 (*a*). In addition, the mean computational cost of the codes, described by CPU time per grid point per time step of the computations, remained nearly constant for LB method and LB-IB methods, regardless of the number of processors, for tests in turbulent channel flow with smooth walls and turbulent channel flow with hairy surfaces, respectively, as seen in figure 2.14 (*b*). In figure 2.14 (*c*) shows that the parallel efficiency is preserved up to the use of 2048 processors.

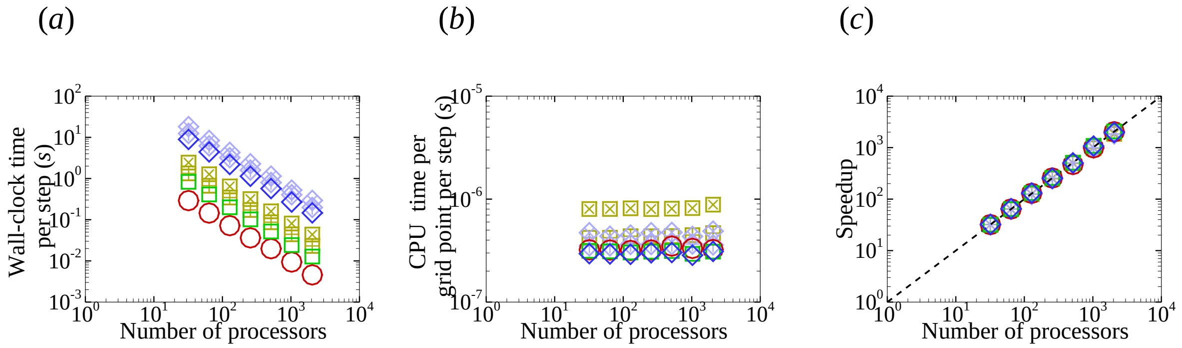

Figure 2.14: Parallel performance on Stampede2 of Texas Advanced Computing Center for LB DNS and LB DNS coupled with IB method: (*a*) Wall-clock time per an iteration, (*b*) Wall-clock time per grid points per an iteration, and (*c*) speed-up as a function of the number of processors. ○(Red), LB DNS without grid-embedding, smooth channel wall, resolution $512 \times 256 \times 221$; □(Green), LB DNS with grid embedding, $GR = 2$, smooth channel wall, resolution $1024 \times 512 \times 28$ (nw)/ $512 \times 256 \times 197$ (core)/ $1024 \times 512 \times 28$ (nw); ▽ (Blue) , LB DNS with grid embedding $GR = 4$, smooth channel wall, resolution $2048 \times 1024 \times 56$ (nw)/ $512 \times 256 \times 197$ (core)/ $2048 \times 1024 \times 56$ (nw); ⊞ (Brown), IB-LB DNS with grid embedding $GR = 2$, flexible hairy surfaces $s_x^{+0} \approx 8$, $s_y^{+0} \approx 8$, $h^{+0} \approx 8$, $K_s = 1$, $K_b = 5 \times 10^{-5}$, resolution $1024 \times 512 \times 36$ (nw)/ $512 \times 256 \times 197$ (core)/ $1024 \times 512 \times 36$ (nw); ⊠ (Brown), IB-LB DNS with grid embedding $GR = 2$, flexible hairy surfaces $s_x^{+0} \approx 4$, $s_y^{+0} \approx 4$, $h^{+0} \approx 8$, $K_s = 1$, $K_b = 5 \times 10^{-5}$, resolution $1024 \times 512 \times 36$ (nw)/ $512 \times 256 \times 197$ (core)/ $1024 \times 512 \times 36$ (nw); ⟐(Purple), IB-LB DNS with grid embedding $GR = 4$, flexible hairy surfaces $s_x^{+0} \approx 8$, $s_y^{+0} \approx 8$, $h^{+0} \approx 8$, $K_s = 1$, $K_b = 5 \times 10^{-5}$, resolution $2048 \times 1024 \times 72$ (nw)/ $512 \times 256 \times 197$ (core)/ $2048 \times 1024 \times 72$ (nw); ◈(Purple), IB-LB DNS with grid embedding $GR = 4$, flexible hairy surfaces $s_x^{+0} \approx 4$, $s_y^{+0} \approx 4$, $h^{+0} \approx 8$, $K_s = 1$, $K_b = 5 \times 10^{-5}$, resolution $2048 \times 1024 \times 72$ (nw)/ $512 \times 256 \times 197$ (core)/ $2048 \times 1024 \times 72$ (nw).

2.7 Verification and Validation

A number of numerical experiments have been performed to verify and validate the present IB-LB methods. These tests include verification of second-order accuracy of the LB and LB-IB codes in laminar flow, grid independence studies in turbulent channel flow with smooth no-slip walls and comparisons to pseudo-spectral results, and grid independence studies in turbulent channel flow with rigid, blade riblets and comparisons to available experimental data. The slip-errors are evaluated for a turbulent channel flow with hairy surfaces in terms of the present and previous IB-LB methods. Details on the verification/validation studies can be found in the following subsections.

2.7.1 Laminar Channel Flow

LB formulations based on the constant flow rate (CFR) and the constant pressure gradient (CPG) have been tested in Poiseulle channel flows. The body force that drives the laminar channel flow is the pressure gradient, which is adjusted during the course of simulation to keep the flow rate constant for CFR formulation, whereas the body force is fixed during the course of simulation for CPG formulation. The streamwise velocity profile with respect to the wall normal direction is compared to the analytical solution. The convergence test is performed to verify the present LB formulations and examine the order of accuracy for both CFR and CPG formulations.

Figure 2.15 shows the normalized streamwise velocity profile with respect to the wall normal direction z (2D simulation) and the relative L_2 norm which is defined as (Mei *et al.*, 2000),

$$L_2 = \sqrt{\frac{\sum_{k=1}^{N_z} (u_{al}(z_k) - u(z_k))^2 \Delta x}{\sum_{k=1}^{N_z} (u_{al}(z_k))^2 \Delta x}}, \tag{2.74}$$

as a function of the wall normal grid points $N_z = 10, 20, 40,$ and 80 for CPG and CFR formu-

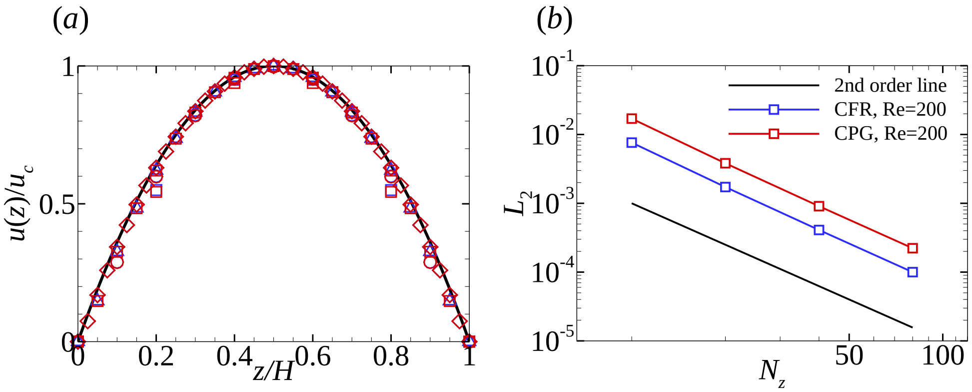

Figure 2.15: (*a*) The streamwise velocity normalized the centerline velocity, u_c, with respect to the wall normal direction, z, normalized by the channel height (H). (*b*) The relative L_2 error norm as a function of grid points along the wall normal direction N_z. The black solid line, square, circle, triangle, diamond symbols indicate the analytical solution, $N_z = 10,\ 20,\ 40,$ and 80, respectively.

lations. u_{al} is the analytical solution of the velocity profile in a Poiseulle channel flow. Using the Chapman-Enskog expansion, the resulting LB scheme provides the second order accuracy (Krüger *et al.*, 2017). The second order accuracy of the proposed scheme is verified through the convergence test as shown in Figure 2.15(b). For CFR formulation, the magnitudes of the relative L_2 error norm are about 2.3 times smaller than those for the constant pressure gradient formulation. This suggests that CFR formulation is more reasonable for all numerical simulations in this study.

2.7.2 Womersley Flow with and without Flexible Flaps

The present study aims to validate the numerical methods against the experimental results obtained from Favier *et al.* (2017). First, the convergence test is performed to verify if the present LB formulation reproduces the analytical solution and satisfies the second order accuracy without the presence of the hairy filaments. Figures 2.16 and 2.17 show the simulation results of Womersley flow with Womersley number of Reynolds number of $Re = U_{max}(3h_0)/\nu = 360$ and $Wo = h_0(2\pi/\nu)^{1/2} = 15$. The analytical solution (Chandrasekaran *et al.*, 2005),

u_{alw}, is represented in figure 2.16(*a*). Figure 2.16(*b*) shows that the velocity profile is converged to the analytical solution with increasing number of grids at the specific time instant, $t/T = 1.0$. To quantify the numerical error, the L_2 error norm of Womersley flow is defined as $L_{2,w} = \sqrt{\frac{1}{N_z}\sum_i^{N_z}\left(\frac{u}{U_{max}} - \frac{u}{U_{max}}|_{alw}\right)^2}$ and evaluated for each grid resolution. For this unsteady flow, $L_{2,w}$ is hovering around the mean value as shown in figure 2.17(*a*). The tail of the time history of $L_{2,w}$ was averaged over 4 time periods to obtain the time-averaged $L_{2,w}$ as represented in the inset of figure 2.17(*a*). In figure 2.17(*b*), the time-averaged $L_{2,w}$ decreases by a factor of the square of the grid resolution (Δx^2), verifying the second order accuracy of the present LB formulation.

Second, the validation study of the present IB-LB method is performed in comparison to the experimental study (Favier *et al.*, 2017). Figure 2.18 (*a*) illustrates the schematic diagram of a row of 10 flexible flaps, mounted on the bottom channel wall. The two-dimensional computational domain is $22h_0 \times 3h_0$, and periodic boundary conditions are applied to the left and right boundaries, while the no-slip boundary conditions are applied to the upper and lower channel walls via the half-way bounce back boundary condition (Ladd, 1994). The spacing between flaps in the streamwise direction was set to $0.5h_0$. The periodic, sinusoidal pressure gradient was applied to drive the oscillating channel flow, $\partial\bar{p}/\partial x = A_{osc}cos\,(2\pi f_{osc}t)$. A_{osc} and f_{osc} are the amplitude and frequency of the pressure gradient, respectively. In this numerical experiments, A_{osc} and f_{osc} are determined, corresponding to Reynolds number of $Re = U_{max}(3h_0)/\nu = 360$ and Womersley number of $Wo = h_0(2\pi/\nu)^{1/2} = 15$, to reproduce the flow condition represented in the reference study (Favier *et al.*, 2017). Figure 2.18 (*b*) displays the non-dimensional vorticity fields influenced by the wall-mounted flexible flaps. In two-dimensional simulations, the flexible hairy filament is considered to be a flexible plate or flap. The interaction between the fluid flow and the flexible flaps seems physically plausible based on a qualitative analysis. Figure 2.18 (*c*) presents the comparison between the simulation and experimental results for the streamwise tip positions of F1-F5 (First left flap - fifth left flap). In this figure, the numerical simulation shows good agreement with experimental results.

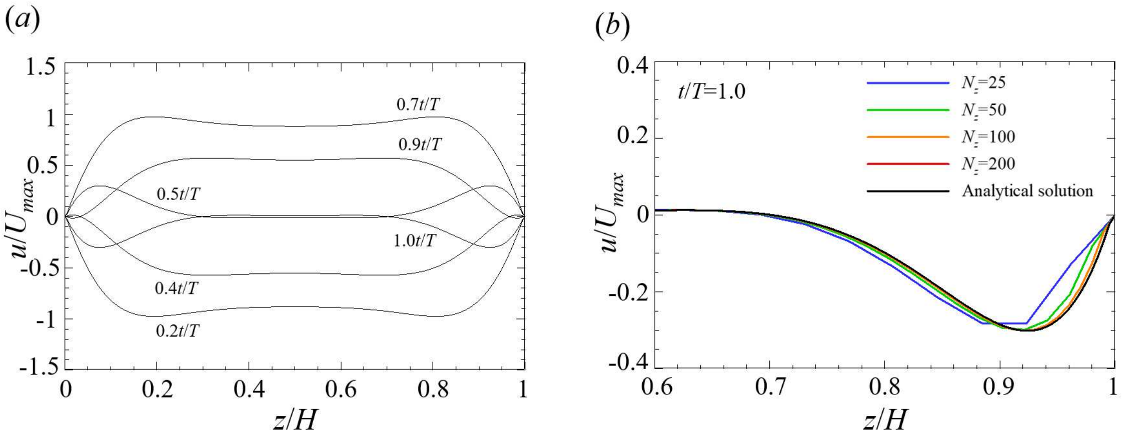

Figure 2.16: (*a*) Analytical solution of Womersley flow. (*b*) The velocity profiles for each grid resolution at the time instant of $t/T = 1.0$.

For the convergence study, numerical experiments are performed varying the grid resolution and parameters correspondingly. The cases used for the numerical experiments are tabulated in Table 2.3. As shown in figure 2.19, the present IB-LB method for the simulation of the dynamics of elastic, slender bodies during their interaction with unsteady flows holds the second order accuracy.

CFL	$(L_x/\Delta x \times L_z/\Delta z)$	$H/\Delta x$	$h_0/\Delta x$	$T/\Delta t$
0.1	330 × 45	45	15	4524
0.075	440 × 60	60	20	8042
0.06	550 × 75	75	25	12566
0.05	660 × 90	90	30	18096
0.0375	880 × 120	120	40	32170

Table 2.3: Cases for the convergence study.

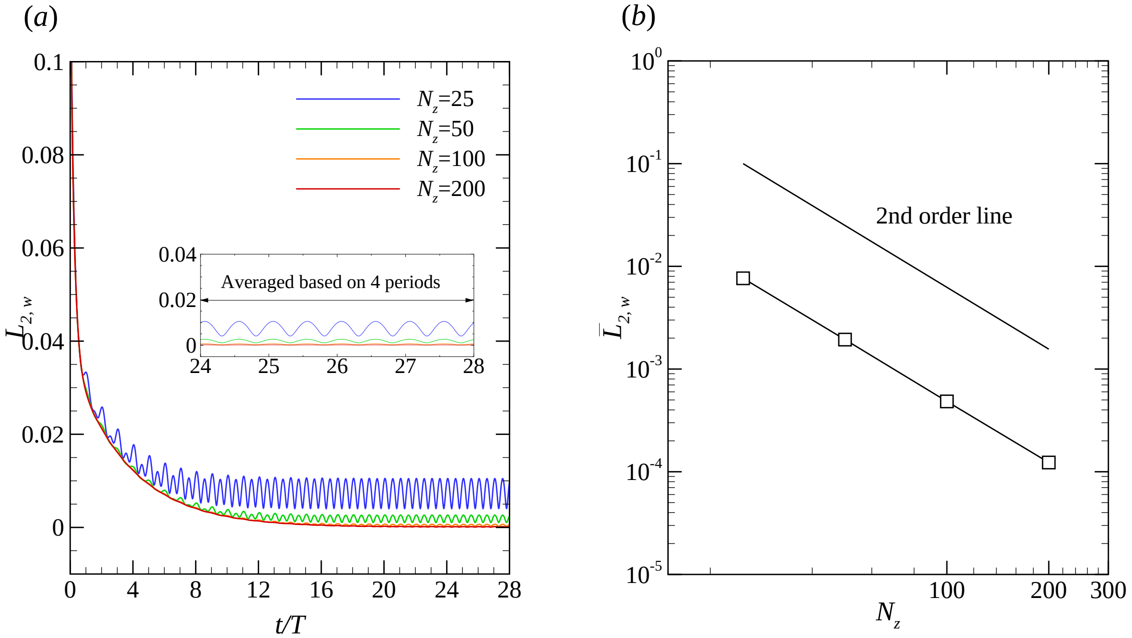

Figure 2.17: (*a*) Time histories of the $L_{2,w}$ of Womersley flow for each grid resolution, $L_{2,w} = \sqrt{\frac{1}{N_z}\sum_i^{N_z}\left(\frac{u}{U_{max}} - \frac{u}{U_{max}}|_{alw}\right)^2}$, is obtained at every time instant at a coarse grid over the last 4 periods to obtain the time-averaged error norm, $\bar{L}_{2,w}$. (*b*) Verification of the second order accuracy of the present LB formulation.

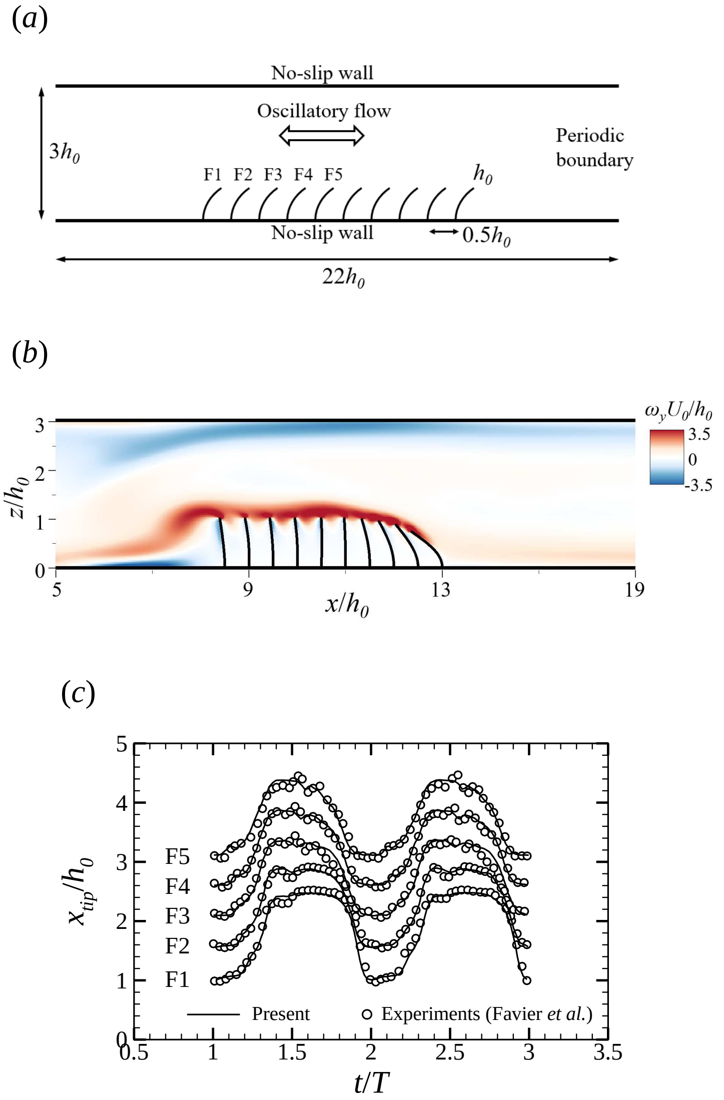

Figure 2.18: (*a*) Schematic of computational domain and boundary conditions for validation. A series of 10 flaps are mounted on a channel wall where an oscillatory flow is generated with a periodic pressure gradient. (*b*) An instantaneous snapshot of the non-dimensional spanwise vorticity field, represented by the contour level ranging from -3.5 to 3.5. (*c*) non-dimensional tip positions of flaps (F1-F5) in the x-direction with respect to the time normalized by the period of the oscillatory flow. Solid line denotes the results from the present simulation, compared against the experimental results (Favier *et al.*, 2017), which is denoted by the circle-shape symbols.

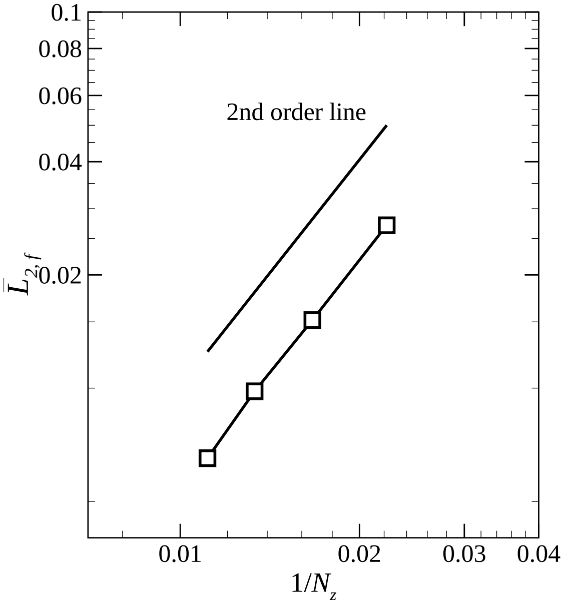

Figure 2.19: The time-averaged error norm, $\bar{L}_{2,f}$, for the position of the flap tips at each grid resolution. Here, $L_{2,f} = \sqrt{\frac{1}{N_f}\sum_i^{N_f}\left(\frac{x_{tip}}{h_0} - \frac{x_{tip}}{h_0}|_{ref}\right)^2}$. For this unsteady FSI simulation, $\frac{x_{tip}}{h_0}$ is obtained at every time and compared to $\frac{x_{tip}}{h_0}|_{ref}$ to obtain $L_{2,f}$ at every same time instant, shared by both a coarse grid resollution and the reference. The time-averaged error norm, $\bar{L}_{2,f}$ is then computed by averaging $L_{2,f}$ at the time instants. The reference case corresponds to the finest grid resolution with $CFL = 0.375$.

2.7.3 Turbulent Channel Flow

The accuracy of LB DNS code in turbulent flow with smooth, no-slip walls was assessed by comparing its results, both with and without grid embedding, to pseudo-spectral DNS in turbulent channel flow. The pseudo-spectral DNS results are given from an earlier study (Rastegari & Akhavan, 2018). The bulk Reynolds number of $Re_b = q/2\nu = 3600$, where q is the flow rate per unit channel width. The corresponding friction Reynolds number of $Re_{\tau 0} \approx 221$. The subscript 0 denotes the base channel flow with no-slip walls. Periodic boundary conditions are imposed in x and y direction. A channel size $L_x \times L_y \times L_z = 5H \times 2.5H \times 2H$ is used in the numerical experiments. The corresponding numbers of grid points along x, y, and z directions in the flow domain are 512, 256, and 223, respectively. LB DNS without grid embedding was performed using uniform grid spacings of $\Delta x^{+0} \approx 2$. LB DNS with grid embedding was performed with grid refinement ratios of $GR = 2$ and 4, employed in the region between the channel walls and the edge of the buffer layer ($z^{+0} \approx 30$), resulting in grid spacings of $\Delta x_f^{+0} \approx 1$ and $\Delta x_f^{+0} \approx 0.5$ at $z^{+0} \lesssim 30$ for $GR = 2$ and 4, respectively, as shown in figure 2.2. Here, the superscript $+0$ denotes the normalization with the wall-friction velocity, $u_{\tau 0}$, and the kinematic viscosity of fluid, ν, for the turbulent channel flow with smooth, no-slip walls.

The LB code has been verified by comparing turbulent statistics to those given from pseudo-spectral DNS data. Figure 2.21(a) shows the time history of the skin-friction coefficient. The time history of C_f was averaged from $tU_b/H = 100$ to 400, corresponding to the eddy turnover time of approximately 6.2 for the initial cut-off and 18.6 for the time-averaging, respectively. The resulting skin-friction coefficients are $C_f = 0.007714$, 0.007668, and 0.007662 for non-grid embedding, $GR = 2$, and 4. The relative errors of the time averaged C_f to $C_{f,ps}$ pseudo-spectral DNS, $|C_{f,ps} - C_f|/C_{f,ps}$, are 1.0%, 0.4%, and 0.3% for non-grid embedding, $GR = 2$, and 4, respectively. Figure 2.21(*b*) shows the mean velocity profile as a function of z^+. The mean velocity within the viscous sub-layer ($z^+ \leq 5$) increases linearly with the wall normal location, showing a good agreement with the law of the wall. In the log layer, the mean velocity profile agrees well with the logarithmic law,

$$\left\langle \bar{U} \right\rangle^+ = \frac{1}{\kappa} \ln z^+ + B, \tag{2.75}$$

where κ is Karman constant ($\kappa = 0.41$) and B is the intercept of logarithmic law representation of the mean velocity profiles in the channel flow with smooth, no-slip walls ($B = 5.5$).

The mean velocity profiles from non-grid embedding, $GR = 2$, and 4 agree well with the mean velocity profile from pseudo-spectral DNS as shown in figure 2.21(*b*). Figures 2.21(*c*) and (*d*) show the turbulence intensities as a function of z^+. LB DNS data show a good agreement with pseudo-spectral DNS data. Figure 2.21(*e*) shows the mean Reynolds stress as a function of z/H. The theoretical total shear stress is denoted by the dotted line in figure 2.21(*e*). The total shear stress consists of two components: turbulent shear stress ($-\left\langle \overline{uw} \right\rangle^+$) and laminar shear stress (du^+/dz^+). The contribution of Reynolds stress to the total shear stress is negligible adjacent to the wall, implying that the total shear stress at $z/H < 0.15$ depends on the contribution of laminar shear stress, and conversely, depends on that of turbulent shear stress at $0.15 < z/H < 1$. Figure 2.21(*f*) shows the mean root mean square (rms) of the pressure fluctuation as a function of z^+. LB DNS results show that the mean rms of the pressure fluctuation becomes closer to pseudo-spectral data with increasing grid refinement ratio. Higher order stats such as skewness and flatness from LB DNS was compared to those from pseudo-spectral DNS as shown in figures 2.21(*a*) and (*b*). The skewness profiles agree well with those of pseudo-spectral DNS, except for LB DNS results without grid-embedding. Similarly, the flatness profiles also agree well with those of pseudo-spectral DNS, except for LB DNS results without grid-embedding. These results imply that LB DNS requires grid-embedding to obtain accurate results near the wall region.

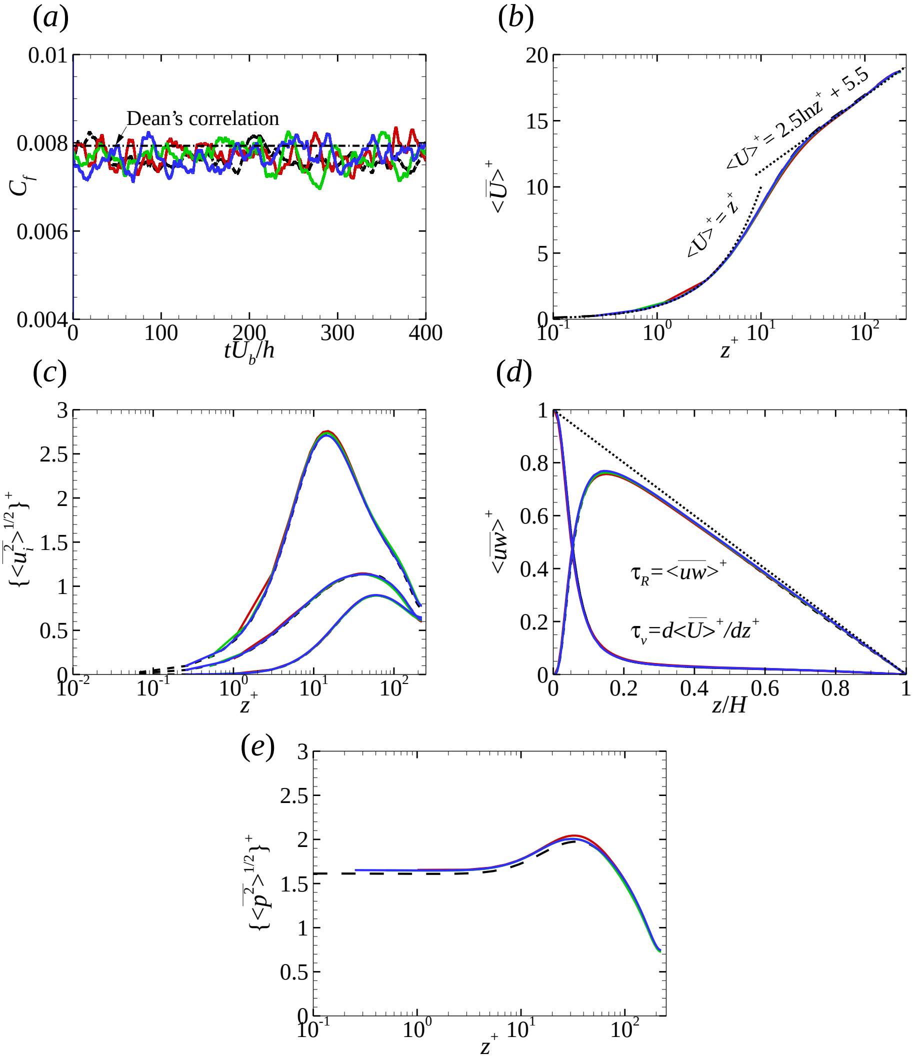

Figure 2.20: (*a*) Time history of the skin-friction coefficients. Turbulent stats: (*b*) Mean velocity, (*c*) mean rms of velocity fluctuations, (*d*) Reynolds shear stress, (*e*) mean pressure fluctuation. Red line, non-grid embedding; green line, GR=2; blue line, GR=4; Black dashed line, pseudo-spectral DNS data.

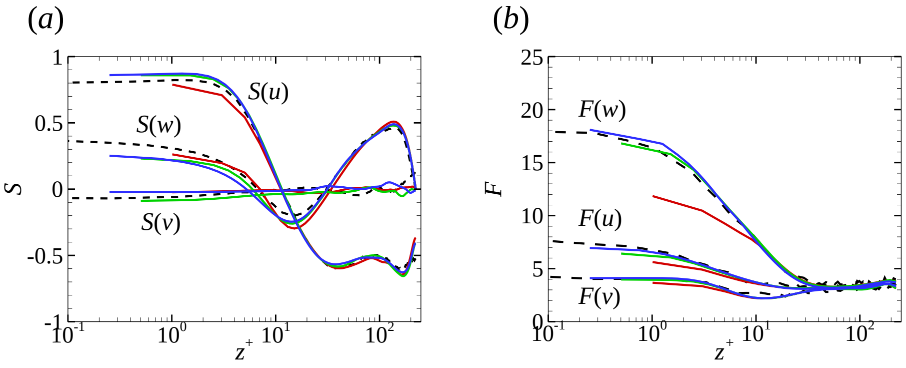

Figure 2.21: (*a*) Skewness and (*b*) flatness of the streamwise, spanwise, and wall normal velocity fluctuations in turbulent channel flows. Line types as in figure 2.20.

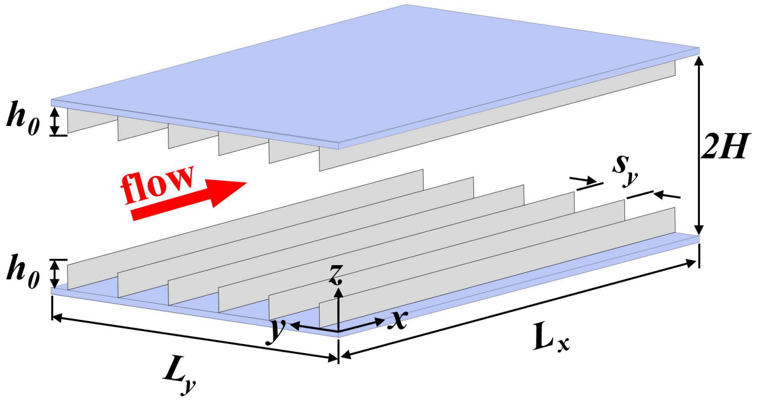

Figure 2.22: Schematic diagram of a turbulent channel over surfaces covered with blade riblets.

2.7.4 Turbulent Flow over Blade Riblets

A grid resolution study was performed to verify the present IB-LB implementation in a turbulent flow over blade riblets. The bulk Reynolds number is $Re_b = q/2\nu = 3600$, where q is the flow rate per unit channel width. The corresponding friction Reynolds number is $Re_{\tau 0} \approx 221$. The subscript, 0, denotes the base channel flow with no-slip walls. Periodic boundary conditions are imposed in the streamwise and spanwise directions. The turbulent channel flow was driven by the same flow rate, dynamically adjusting the mean pressure gradient over time. The blade riblet surface is realized by rows of rigid hairy filaments implanted at every grid cell center in the streamwise direction with an appropriate spanwise spacing. Figure 2.22 shows a schematic diagram of a turbulent flow over blade riblets. In this numerical exercise, the spanwise spacing was set to $s_y^{+0} \approx 16$, which is the optimal spanwise spacing of the blade riblets (Bechert *et al.*, 1997a; Garcia-Mayoral & Jimenez, 2011). Two sets of simulations were carried out using two distinct grid resolutions: Grid 1 ($GR = 2$ with $\Delta x_c^{+0} \approx 2$, $\Delta x_f^{+0} \approx 1$) and Grid 2 ($GR = 4$ with $\Delta x_c^{+0} \approx 2$, $\Delta x_f^{+0} \approx 0.5$). The fine grid resolution is set from the channel wall, $z^{+0} = 0$, to the edge of the buffer layer, $(z + h_0)^{+0} \approx 30$, for both Grid 1 and Grid 2. Each row of rigid hairs with $GR = 2$ and $GR = 4$ have the thickness of $\Delta x_{f,GR=2}$ and $\Delta x_{f,GR=4}$, respectively. For $GR = 4$, the thickness of a rib is twice smaller than that for $GR = 2$ ($\Delta x_{f,GR=2} = 2\Delta x_{f,GR=4}$) since the cross-sectional area of each filament occupies one Eulerian grid cell. Therefore, two rows of rigid hairs with $GR = 4$ can be consecutively placed in the streamwise and spanwise directions to reproduce the same geometrical features of the blade riblets represented by $GR = 2$, as shown in figure 2.23.

In this simulation setup, the turbulent statistics were compared for both grid resolutions. Figure 2.24 shows the comparison of the mean velocity profiles, mean root-mean-square of velocity fluctuations, and shear stress distributions in the wall-normal direction. The drag reductions of

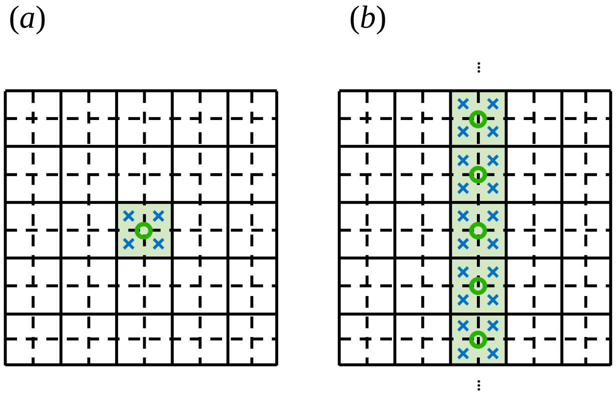

Figure 2.23: Schematic of the filament distribution for $GR = 2$, denoted by O (Green), and $GR = 4$, denoted by x (Blue), respectively, on the top view. (*a*) Top view of rigid hairs mounted on the channel wall. The cross-sectional area, denoted by green-shaded area, of one hair with $GR = 2$ can be reproduced by 2×2 hairs with $GR = 4$, regarding the effective area of each filament that occupies one Eulerian grid cell. (*b*) One row of rigid hairs with $GR = 2$ can be replicated by two rows of rigid hairs with $GR = 4$. The solid grid lines denote the lattices with $\Delta x_{f,GR=2}$, and the dashed grid lines denote the lattices with $\Delta x_{f,GR=4}$.

$DR = 7.0\%$ and $DR = 6.6\%$ were obtained for $GR = 2$ and $GR = 4$, respectively. The difference of drag reductions between $GR = 2$ and $GR = 4$ is close enough to be considered as grid independent. Furthermore, the turbulent statistics from $GR = 2$ agree well with those from $GR = 4$, supporting the grid independence.

2.7.5 Turbulent Flow over Flexible, Filamentous Surfaces

A numerical experiment was conducted within the framework of a diffusive, direct-forcing IB scheme coupled with LB method to determine whether the improved reciprocity of interpolation-spreading operators yields acceptable accuracy regarding basic kinematic conditions such as the no-slip and non-penetration conditions. As discussed in Section 2.3.2.1, the oversimplified assumption, where Lagrangian forcings remain constant along the IB, (Pinelli *et al.*, 2010; Favier *et al.*, 2014; Li *et al.*, 2016; O'Connor & Revell, 2019) is not valid for an elastic, slender solid body that interacts with unsteady, non-uniform flows. Additionally, it was noted that the approach proposed by Jiang & Liu (2019), where the averaged correcting parame-

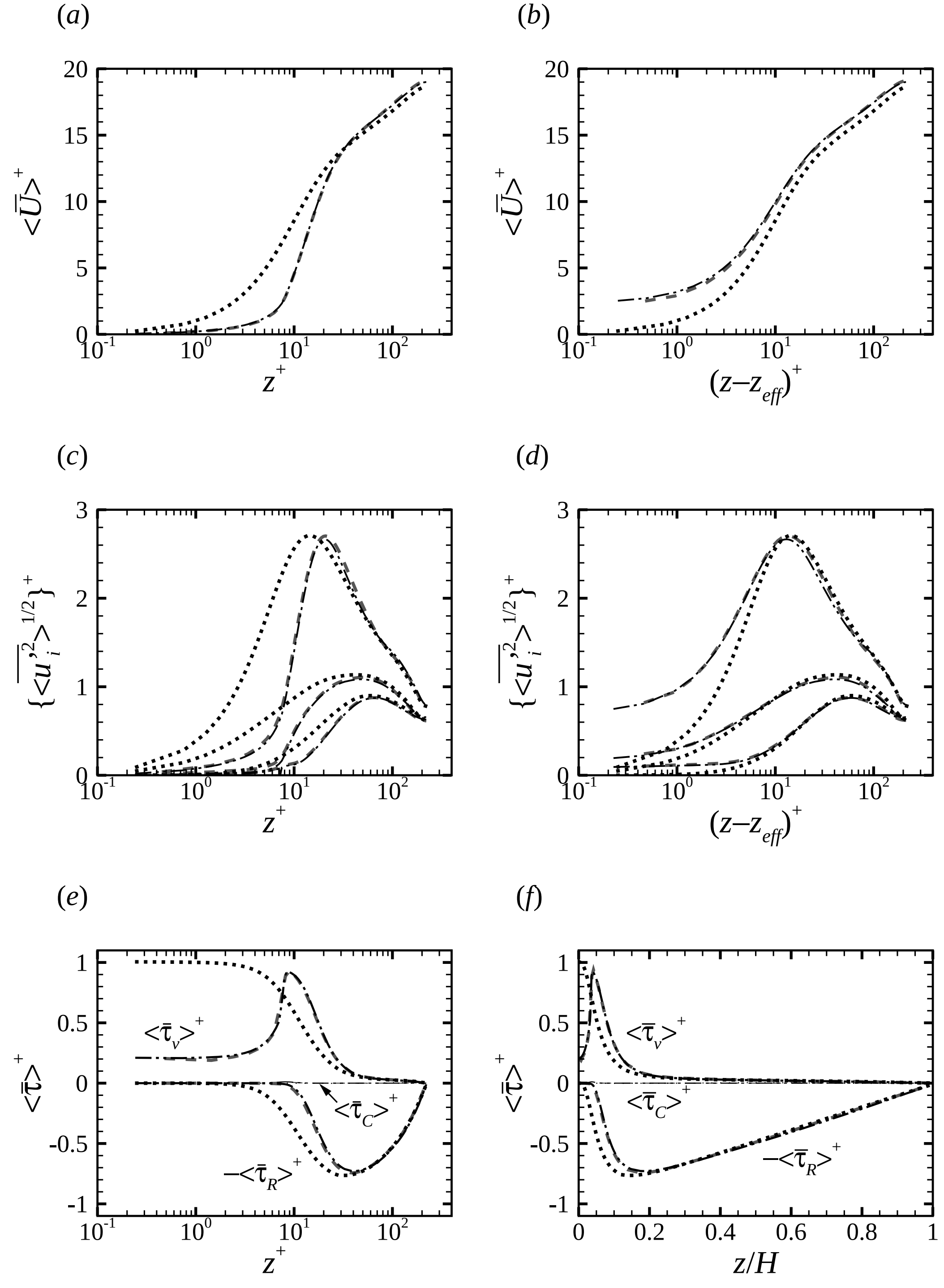

Figure 2.24: (*a*), (*b*)Mean velocity profiles, (*c*), (*d*) turbulence intensities with respect to z^+ (First column) and $(z - z_{eff})^+$ (Second column). (*e*), (*f*) Distribution of shear stresses with respect to z^+ (First column) and z/H (Second column). IB-LB DNS results of turbulent flow over blade riblets are represented for $h_0^{+0} \approx 8$, $h_0/s = 1/2$, $h_0/t \approx 0.06$, with Grid 1, – – (Gray), and Grid 2, –··– (Black), respectively. For comparison, LB DNS result of the base turbulent channel flow with smooth, no-slip walls is represented with · · · · · (Black).

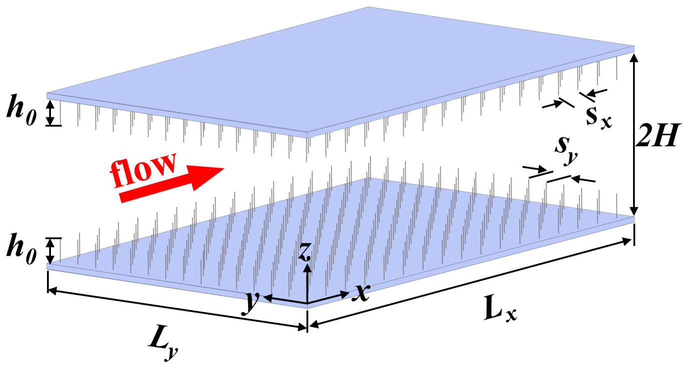

Figure 2.25: Schematic diagram of a turbulent channel over surfaces covered with hairy surfaces.

ter is incorporated to the spreading operator, inherently violates the mathematical formulation of the reciprocity. While the analytical proof of the incorrectness resulting from the oversimplified assumption and its resulting linear matrix equation form was presented in Section 2.3.2.1.

The schematic depicted in figure 2.25 illustrates a turbulent flow over surfaces covered with flexible filaments that are uniformly distributed and erected in their initial, undeformed state. Numerical experiments are conducted for the case of the filament height of $h_0^{+0} \approx 8$, height-to-spacing ratio of $h_0/s = 1$, dimensionless stretching coefficient of $K_s^* = 1$, dimensionless bending rigidity of $K_b^* = 2 \times 10^{-6}$, density ratio of $\rho_r = 700$. The slip-error is a measure of the deviation from the unity in the ratio of the velocity of Lagrangian markers to the fluid velocity interpolated to the marker, i.e., $\boldsymbol{U}(s,t)/I\left[\boldsymbol{u}(\boldsymbol{x},t)\right]$. A value of 1 for $\boldsymbol{U}(s,t)/I\left[\boldsymbol{u}(\boldsymbol{x},t)\right]$ indicates strict satisfaction of the no-slip condition. Compared to the previous IB-LB method (Jiang & Liu, 2019), the present method exhibits significant improvement in reducing the slip-error. As shown in Figure 2.26, the previous method results in huge slip errors up to $O(1000)$ in percentage, which is unacceptable. In contrast, the present method demonstrates a substantial enhancement in imposing the no-slip condition along the IB. The improved reciprocity ensures better no-slip enforcement on the Lagrangian markers, resulting in a maximum slip error of less than $\sim 2\%$. The current level of the slip-error is marginal enough to consider the present IB-LB method acceptable for the DNS of turbulent channel flow over hairy surfaces.

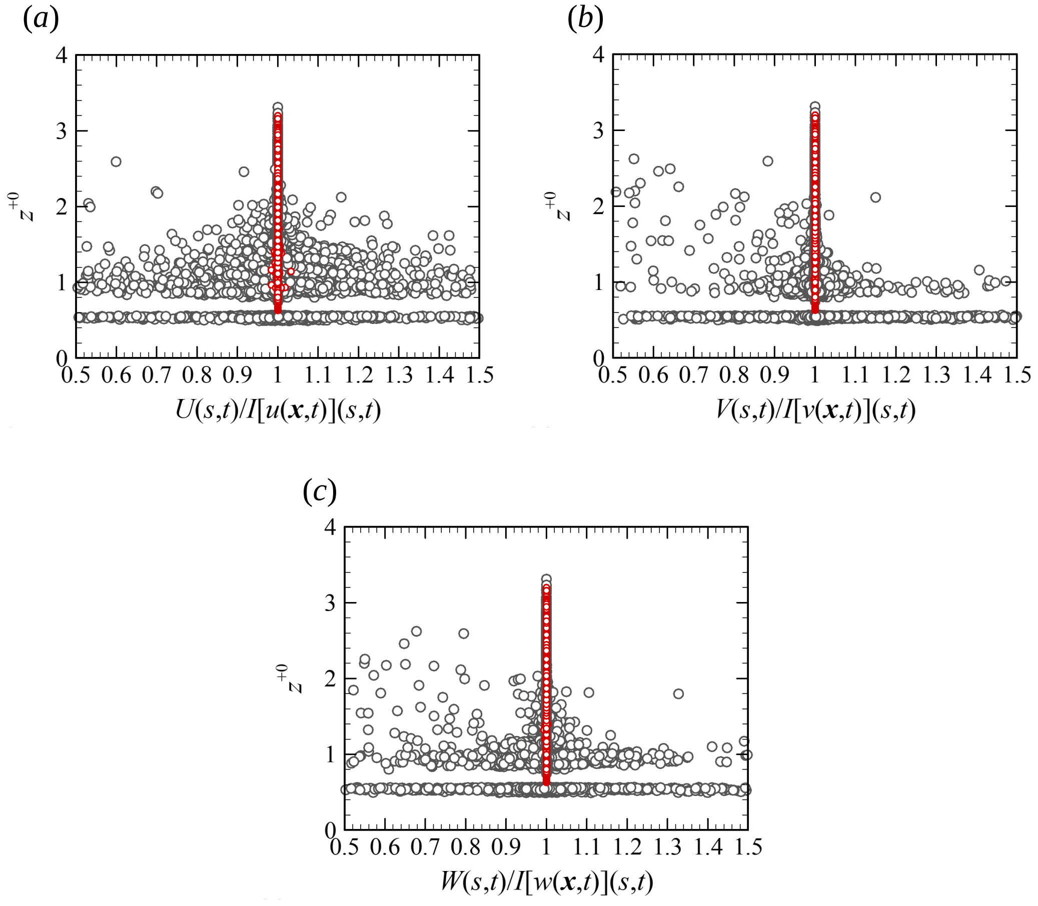

Figure 2.26: Slip errors obtained from the present method and reference method, denoted by the red-contoured and grey-contoured symbols, respectively, in the (*a*) streamwise, (*b*) spanwise, and (*c*) wall-normal directions. IB-LB DNS results of turbulent flow over hairy surfaces are represented for $h_0^{+0} \approx 8$, $h_0/s = 1$, $K_s^* = 1$, $K_b^* = 2 \times 10^{-6}$, $\rho_r = 700$. The slip errors at each Lagrangian marker were measured along the entire filaments implanted in both channel walls over 100 realizations of the flow over the eddy turnover time of ≈ 6.2. $\boldsymbol{U}(s,t)/I\left[\boldsymbol{u}(\boldsymbol{x},t)\right](s,t) = (1,1,1)$ indicates that the no-slip on the marker is strictly satisfied.

CHAPTER 3

Skin-friction DR with Hairy Surfaces

The carpet of flexible filaments creates a functional surface that dynamically interacts with turbulence and modifies its dynamics. Depending on the filament parameters, these interaction can lead to drag enhancement or drag reduction. This study investigated the filament deflection in response to turbulent flow and its effects on the modification of turbulence dynamics. The resulting drag reduction was evaluated for various filament parameters such as Cauchy number, filament height, filament height-to-spacing ratio. In order to gain an understanding of the influence of hairy surfaces on turbulence dynamics, an analysis of turbulence statistics is conducted for a channel with hairy surfaces, and compared to the statistics of the base turbulent channel flow.

3.1 Direct Numerical Simulation Study

3.1.1 Problem Statement

Simulations were performed in turbulent channel flows, assumed to be periodic in the streamwise (*x*) and spanwise (*y*) directions, with periodicity lengths of L_x and L_y, and a channel height of $2H$. Carpets of filaments of initial undisturbed filament heights of h_0, filament thicknesses of d, and uniform filament spacings of $s_x = s_y = s$ in the streamwise and spanwise directions were implanted on both channel walls, as shown in Figure 3.1(*a*).

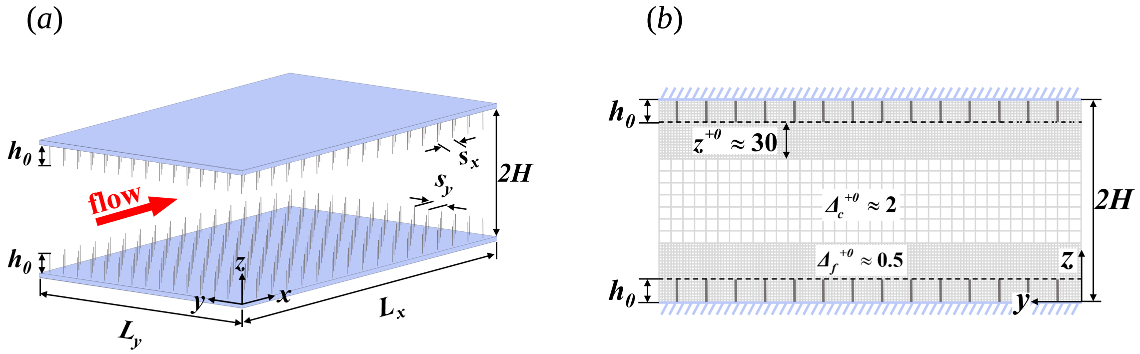

Figure 3.1: Schematic of the channel, coordinate system, and the computational grid used in the simulations. (*a*), the channel configuration and coordinate system are depicted, where a uniform carpet of flexible filaments (with $s_x = s_y$) is implanted on both channel walls, with the filaments shown in their initial un-deformed state. (*b*) The computational grid used in the simulations, with a grid-embedding ratio of 4:1.

Throughout all simulations, a constant flow rate was enforced in the turbulent channel to ensure that the bulk Reynolds number was $Re_b \equiv q/\nu = 7200$, where $q \equiv U_b(2H)$ represents the flow rate per unit spanwise width of the channel. This value of bulk Reynolds number correspond to friction Reynolds numbers of $Re_{\tau 0} \equiv Hu_{\tau 0}/\nu \approx 221$ in a turbulent channel flow with smooth, no-slip walls, which serves as the baseline for comparison.

In order to increase the accuracy of our calculations, this study employed grid embedding (Lagrava *et al.*, 2012) with a grid ratio of 4:1 in the region between the channel walls and a height of $z^{+0} \approx (30 + h_0^{+0})$ from the channel walls, as shown in figure 3.1(*b*). Here, the superscript $+0$ indicates normalization with respect to the wall friction velocity, $u_{\tau 0}$, and the kinematic viscosity, for the base turbulent channel flow. The resulting grid spacings were $\Delta_f^{+0} \approx 0.5$ in the region $0 \leq z^{+0} \lesssim (30 + h_0^{+0})$, and $\Delta_c^{+0} \approx 2$ in the region $(30 + h_0^{+0}) \lesssim z^{+0} \leq H^{+0}$.

3.1.2 Governing Dimensionless Parameters

The dynamics of filaments and their interactions with the surrounding fluid flows are influenced by several non-dimensional groups. These include the filament's geometrical parameters such as the initial height of the filament in wall units of the base flow, h_0^{+0}; filament diameter, d^{+0}; filament height-to-spacing ratio, h_0/s; density ratio of the filament to the surrounding fluid, $\rho_r = \Delta\rho/\left(\Delta\rho_f A_0\right)$ where A_0 is the effective cross-sectional area, which is already discussed in Section 2.7; and the Cauchy number, defined as the ratio of the hydrodynamic forces acting on the filament to the restoring force. The Cauchy number is expressed as Equation 3.1 (Luhar & Nepf, 2016; He *et al.*, 2022),

$$Ca = \frac{\rho_f {u_{\tau_0}}^2 d h_0^3}{K_b}. \tag{3.1}$$

where K_b is the bending rigidity of the filaments, and u_{τ_0} is the characteristic fluid velocity acting on the filaments. The friction velocity, u_{τ_0}, is used as the characteristic velocity since the filaments are placed within the inner layer, where the friction velocity is the more relevant velocity scale.

In addition to the non-dimensional groups mentioned above, it is helpful to define the time scale ratio, given by $\frac{T_{fil} u_{\tau_0}}{H}$, which represents the ratio of the characteristic time scale of the filaments, T_{fil}, to the time scale of the largest eddies in the base turbulent channel flow. This time scale ratio can be expressed by the combination of the Cauchy number, the density ratio, and the geometrical parameters of the filaments as,

$$\frac{T_{fil}\, u_{\tau_0}}{H} = \frac{h_0}{H}\sqrt{(Ca)\left(\frac{\Delta\rho}{\rho_f A_0}\right)\left(\frac{d}{h_0}\right)}. \tag{3.2}$$

Here, the superscript $+0$ denotes the normalization with the wall-friction velocity, $u_{\tau 0}$, and the kinematic viscosity of fluid, ν, for the base turbulent channel flow with smooth, no-slip walls. Similarly, the superscript $+$ denotes the normalization with the wall-friction velocity, u_τ, and the kinematic viscosity of fluid, ν, for the turbulent channel flow with the presence of the surface-textures. Note that the wall friction velocity with the surface textures is obtained at the actual channel wall in this study.

A parametric study was conducted in turbulent channel flows at a Reynolds number of $Re_b =$

7200 ($Re_{\tau_0} \approx 221$). The filament height ranges from $h_0^{+0} = 4$ to 16, the filament thickness of approximately $d^{+0} \approx 0.5$, the filament height to spacing ratios ranges from $h_0/s = 1/4$ to 2, the density ratio ranges from $\rho_r = 30$ to 1000, and Cauchy numbers of $Ca = 10$, 20, 40, 60, and 80. The simulations were performed in channels with dimensions of $L_x/H = 5$ and $L_y/H = 2.5$, of which the adequacy of the domain size was confirmed in the previous study (Rastegari & Akhavan, 2018). A summary of all simulations performed in this study is presented in Table 3.1.

3.1.3 Calculation of DR

This study presents the drag reductions with hairy surfaces and compare them with those over a smooth wall. Using the definition of $DR = (1 - C_f/C_{f0})$, the magnitude of drag reduction can be obtained from

$$DR \equiv 1 - \frac{C_f}{C_{f0}} \tag{3.3}$$

where $C_{f0} \equiv \tau_{w0}/\left(\frac{1}{2}\rho U_b^2\right)$ and $C_f \equiv \tau_w/\left(\frac{1}{2}\rho U_b^2\right)$ are the skin-friction coefficients in the base turbulent channel flow with smooth, no-slip walls and in the turbulent channel flow with the filamentous surfaces, respectively, and U_b are the bulk velocity obtained by averaging the streamwise velocity over the entire channel at the same bulk Reynolds number.

The turbulent statistics were collected over a minimum of $12 - 13$ eddy turnover times in the simulation. The simulation was run for a duration of at least 6 eddy turnover times from the initial condition to ensure a statistically steady state. The streamwise mean pressure gradient was then averaged over a minimum of $12 - 13$ eddy turnover times, excluding the initial 6 eddy turnover times. Subsequently, the wall shear stress and friction velocity were calculated based on the averaged pressure gradient. Using these quantities, the friction coefficient was computed and compared to that of the base flow to determine DR.

Case	Symbol	Line type	ρ_r	Ca	h_0^{+0}	s^{+0}	h_0/s	$T_{fil}u_{\tau 0}/H$	z_{eff}^{+}	$DR(\%)$	
SM		······	–	–	–	–	–	–	–	–	–
D700Ca40h4s4	■	——	700	40	4.19	4.19	1	0.125	2.73	1.6	
D700Ca40h4s8	●	— —	700	40	4.19	8.37	1/2	0.031	1.72	2.0	
D700Ca40h6s6	■	——	700	40	6.10	6.10	1	0.083	2.18	3.5	
D700Ca40h6s12	●	— —	700	40	6.10	12.20	1/2	0.021	2.18	3.8	
D700Ca10h8s8	■	——	700	10	7.98	7.98	1	0.063	5.16	1.8	
D700Ca10h8s16	●	— —	700	10	7.98	15.97	1/2	0.016	4.64	2.9	
D700Ca20h8s8	■	——	700	20	7.98	7.98	1	0.063	4.14	3.1	
D700Ca20h8s16	●	— —	700	20	7.98	15.97	1/2	0.016	3.14	3.3	
D700Ca40h8s4	◆	-·-·-	700	40	7.98	3.99	2	0.250	5.20	1.5	
D700Ca40h8s8	■	——	700	40	7.98	7.98	1	0.063	3.11	5.3	
D700Ca40h8s16	●	— —	700	40	7.98	15.97	1/2	0.016	3.11	5.4	
D700Ca40h8s32	▲	- - - -	700	40	7.98	31.94	1/4	0.004	2.19	1.6	
D700Ca60h8s8	■	——	700	60	7.98	7.98	1	0.063	2.65	3.5	
D700Ca60h8s16	●	— —	700	60	7.98	15.97	1/2	0.016	2.65	3.4	
D700Ca80h8s8	■	——	700	80	7.98	7.98	1	0.063	2.67	2.3	
D700Ca80h8s16	●	— —	700	80	7.98	15.97	1/2	0.016	2.19	1.4	
D700Ca40h10s10	■	——	700	40	9.83	9.83	1	0.050	3.61	3.2	
D700Ca40h10s20	●	— —	700	40	9.83	19.66	1/2	0.013	3.58	4.4	
D700Ca40h12s12	■	——	700	40	12.10	12.10	1	0.042	4.06	3.1	
D700Ca40h12s24	■	— —	700	40	12.10	24.20	1/2	0.010	4.05	3.7	
D700Ca40h16s8	◆	—··—	700	40	16.07	8.03	2	0.125	8.54	-0.7	
D700Ca40h16s16	■	——	700	40	16.07	16.07	1	0.031	4.95	3.2	
D30Ca40h8s8	⧄	—·-·—	30	40	7.98	7.98	1	0.063	2.68	1.2	
D30Ca40h8s16	⊘	—·-·—	30	40	7.98	15.97	1/2	0.016	2.69	0.9	
D100Ca40h8s8	◫	— · —	100	40	7.98	7.98	1	0.063	2.68	1.5	
D100Ca40h8s16	⦶	— · —	100	40	7.98	15.97	1/2	0.016	2.67	2.3	
D300Ca40h8s8	⊞	- - - -	300	40	7.98	7.98	1	0.063	3.16	2.1	
D300Ca40h8s16	⊕	- - - -	300	40	7.98	15.97	1/2	0.016	3.15	3.0	
D1000Ca40h8s8	⊠	— —	1000	40	7.98	7.98	1	0.063	3.14	3.5	
D1000Ca40h8s16	⊗	— —	1000	40	7.98	15.97	1/2	0.016	3.14	3.6	

Table 3.1: Summary of the simulations performed in the present study.

3.2 Filament Deflection in Response to Turbulent Flow

Figures 3.2 (*a*), (*c*), (*e*) show the instantaneous configurations of the filaments, for the density ratio of $\rho_r = 700$, filament height of $h^{+0} \approx 8$, and the height-to-spacing ratio of $h_0/s = 1/2$, at three Cauchy numbers of $Ca = 10, 40$, and 80. The density ratio of $\rho_r = 700$ was chosen to mimic the density ratio between bird feather fibers and air density (Reddy & Yang, 2007; Tesfaye *et al.*, 2018), while the filament height of $h^{+0} \approx 8$ was selected based on earlier experiments reporting the maximum drag reduction at this micro-fiber height (Takata *et al.*, 1996).

Figures 3.2 (*b*), (*d*), (*f*) are the contour plots of the streamwise velocity fluctuations on the plane of $z = z_{eff}$, which represents the demarcation at which the fluid flow is subject to the drag force exerted by the filaments. The filaments display a motion that is locked into the motion of turbulent structures, getting lifted up from the wall at the locations of the low-speed streaks and pushed down towards the wall at the locations of the high-speed streaks.

Figure 3.2 (*g*)–(*i*) show the filament configurations projected onto the $x - z$ and $y - z$ planes at different Cauchy numbers of $Ca = 10, 40, 80$. The flexible filaments primarily deflect in the streamwise and wall-normal directions and exhibit the streamlined postures at the spanwise plane in response to the mean flow. In contrast, the spanwise deflection occurs in both positive and negative directions. As Ca increases, the extent of deflection at each direction becomes more significant in the streamwise and wall-normal directions but lesser in the spanwise direction.

To better characterize the filament deflection in response to the turbulent flow, this study explored the probability density function (p.d.f) of the mean deflection, which is determined by the location of the filament tip in relative to its location at undeformed (or initial) state. Figures 3.3 (*a*)–(*c*) show the p.d.f.s of filament deflections in the x, y, and z directions, scaled by the filament height for various filament height-to-spacing ratios of $h_0/s = 1/2, 1, 2$ and Cauchy numbers of $Ca = 10, 20, 40$ and 80. As Cauchy number increases, the restoring force relative

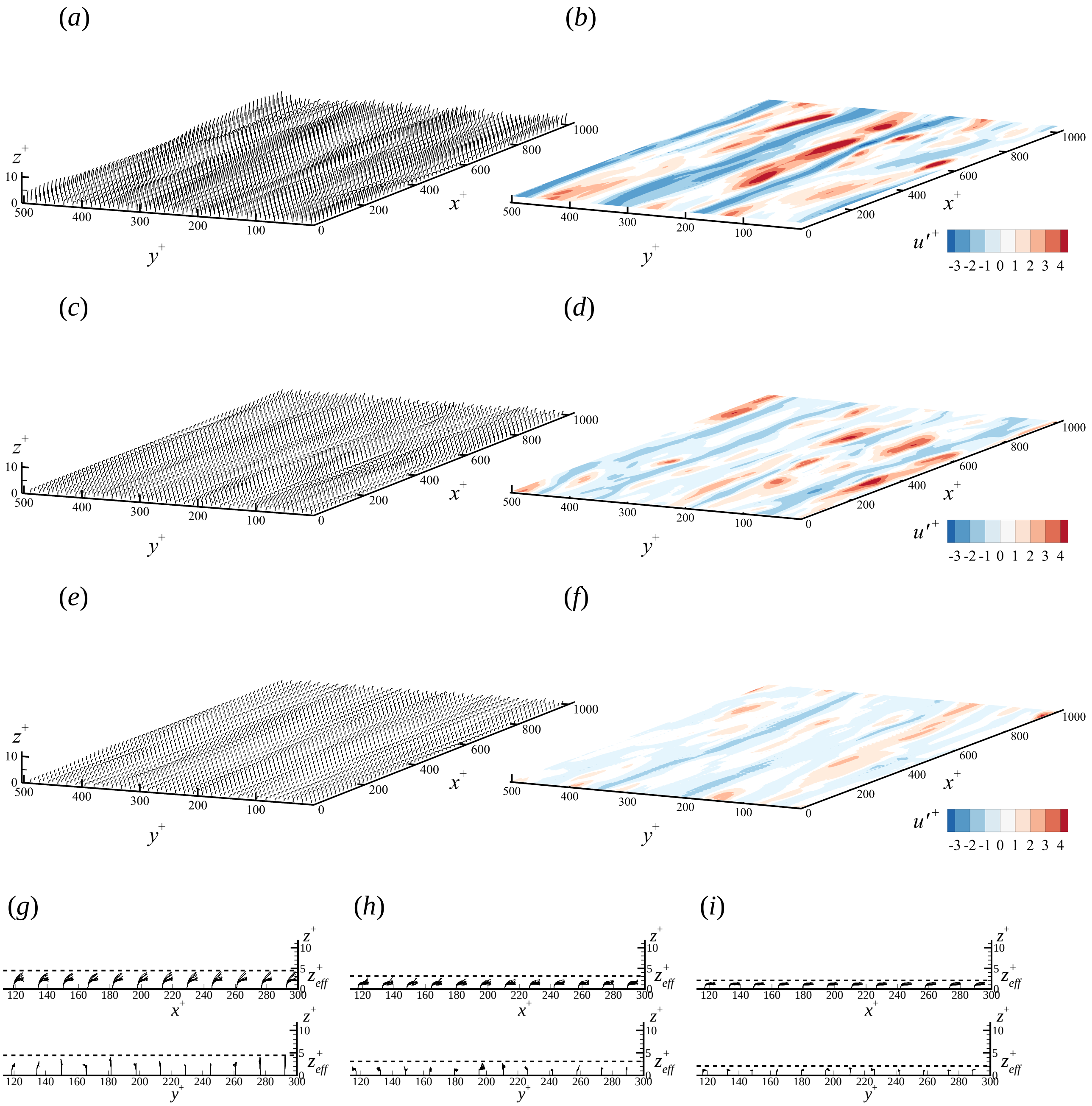

Figure 3.2: Instantaneous filament configurations and $x-y$ plane view of streamwise velocity fluctuation for $\rho_r = 700$, $h^{+0} \approx 8$, $s^{+0} \approx 16$, (*a*, *b*) Ca=10, (*c*, *d*) Ca=40, (*e*, *f*) Ca=80. The $x-y$ plane view was obtained at z^+_{eff} corresponding each Ca. Superimposed filament configurations at x-z plane and y-z plane ($115 \lesssim x^+ \lesssim 300$ and $115 \lesssim y^+ \lesssim 300$) for (*g*) Ca=10, (*h*) Ca=40, (*i*) Ca=80. The dashed lines in (*g*)–(*i*) denote the location of z^+_{eff} at the corresponding Ca.

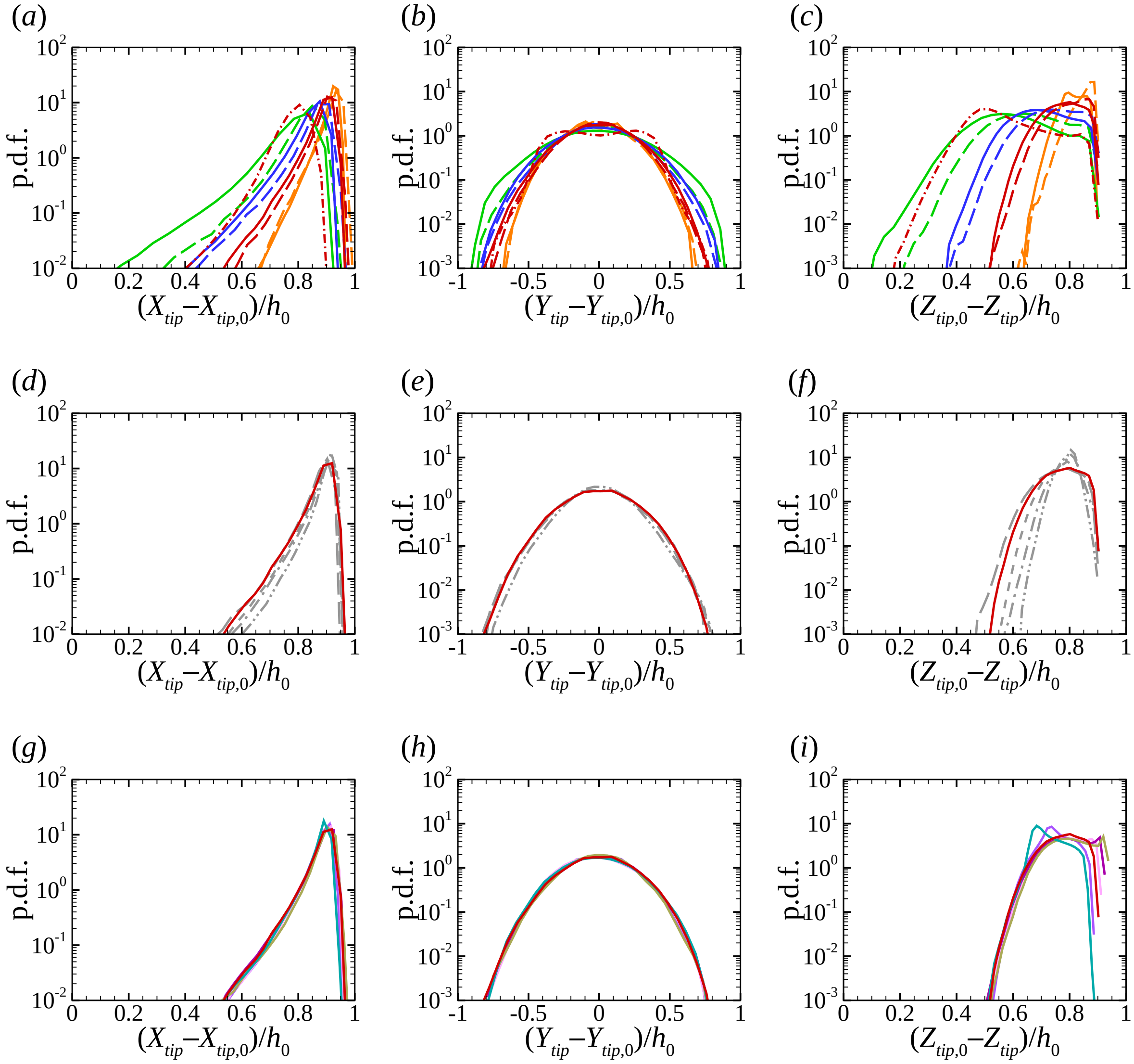

Figure 3.3: Effect of Cauchy number, density ratio, filament height and filament height to spacing ratio on filament deflection, as measured by the p.d.f. of filament tip location relative to its location at the undeformed state: (*a*)-(*c*) effect of Cauchy number and filament height to spacing ratio, at $\rho_r = 700$ and $h_0^{+0} \approx 8$, for Ca=10, 20, 40, 80 and $h_0/s = 1/2, 1, 2$; (*d*)-(*f*) effect of density ratio, at Ca=40, $h_0^{+0} \approx 8$ and $h_0/s = 1$, for $\rho_r = 30, 100, 300, 700, 1000$; (*g*)-(*i*) effect of filament height, at $\rho_r = 700$, Ca=40, $h_0/s = 1$ for $h_0^{+0} \approx 4, 6, 8, 10, 12, 16$. Line types as shown in Table 3.1.

to the hydrodynamic force decreases, and thus the mean streamwise and wall-normal deflections increase. However, the mean spanwise deflection remains symmetric with respect to zero.

Furthermore, the range of p.d.f.s also features the filament deflection for each direction. The ranges of p.d.f.s shown in the streamwise and wall-normal directions are smaller than p.d.f.s. shown in the spanwise direction. This indicates that the behavior of the filament deflections generally more freely in the positive and negative directions than in the streamwise and wall-normal directions. As Cauchy number increases, the ranges of p.d.f.s in the streamwise and wall-normal directions are shrinking, while the range of p.d.f. in the spanwise direction becomes wider. This is because higher Cauchy number brings about less filament deflection due to higher restoring force relative to hydrodynamic force, and thus filament tips interact with higher velocity fluctuations as they are lifted away from the channel walls.

An additional characteristic of the mean deflection represented by the flexible filaments was observed in terms of h_0/s. As h_0/s increases, the filamentous layer becomes denser, and the motion of individual hairy filaments affects the motions of neighboring filaments, resulting in a more pronounced mutual-sheltering effect (Raupach, 1992; Luhar *et al.*, 2008; Shao & Yang, 2005). The mutual-sheltering reduces the transfer of momentum flux from the overlying flow to the filaments, thus making them less deflective. As a result, the peaks of the p.d.f.s in both the streamwise and wall-normal directions shift towards smaller values with increasing h_0/s, as shown in figure 3.3 (*a*) and (*c*). Moreover, another distinct feature of the spanwise mean deflection is observed with increasing h_0/s. Figure 3.3 (*b*) shows that the p.d.f.s of the spanwise mean deflection generally display one peak located at around $(Y_{tip} - Y_{tip,0})/h_0 = 0$ for $h_0 = 1/2$ and 1, but this behavior breaks down as h_0/s increases to 2, exhibiting multiple peaks located far from $(Y_{tip} - Y_{tip,0})/h_0 = 0$. This is because as the filamentous layer becomes denser, the flexible filaments move in the spanwise direction to circumvent their neighbors, located next to them in the streamwise direction.

Figures 3.3 (*d*)–(*f*) illustrate the p.d.f.s of the mean filament deflection for fixed filament height of $h^{+0} \approx 8$, height-to-spacing of $h_0/s = 1/2$ and Cauchy number of $Ca = 40$, at different density ratios of $\rho_r = 30, 100, 300, 700, 1000$. The range of filament deflection becomes wider with increasing density ratio in each direction. This is because a higher density ratio brings about higher restoring force of the flexible filament relative to the hydrodynamic force, resulting in less deflection. With less deflection, the filament tips are located farther away from the channel walls and thus more subject to the increased fluid velocity fluctuations. As a result, the filament tips with higher density ratio move more actively and deflect over a wider range, as compared to a lower density ratio.

Figure 3.3 (*g*)–(*i*) show the p.d.f.s of $(\mathbf{X}_{tip} - \mathbf{X}_{tip,0})/h_0$ for different heights of $h^{+0} \approx 4-16$, with the fixed density ratio of $\rho_r = 700$, height-to-spacing of $h_0/s = 1$ and Cauchy number of $Ca = 40$. In figures 3.3(*g*) and (*h*), the p.d.f.s of $(X_{tip} - X_{tip,0})/h_0$ and $(Y_{tip} - Y_{tip,0})/h_0$ are statistically self-similar in terms of the filament heights. Moreover, the self-similarity is maintained in the wall-normal direction at $(Z_{tip,0} - Z_{tip})/h_0 \lesssim 0.6$. This self-similarity suggests that the filament deflection is primarily characterized by the filament height.

3.3 Effects of Filament Parameters on DR

The effects of filament parameters on the drag reduction were evaluated. This study first started the parametric study with the density ratio of $\rho_r = 700$, mimicking the density ratio of the chicken feather fiber to the air density (Reddy & Yang, 2007; Tesfaye *et al.*, 2018), and the filament height of $h^{+0} \approx 8$, regarding the micro-fiber height that provided the maximum drag reduction in the earlier experiments (Takata *et al.*, 1996), at various Cauchy numbers of $Ca = 10, 20, 40, 60, 80$ and two filament spacings of $s^{+0} \approx 8$ and 16.

In figure 3.4(*a*), the maximum drag reduction of $DR \approx 5.4\%$ occurs at $Ca = 40$. The drag reduction decreases as Cauchy number deviates from $Ca = 40$. Specifically, at $Ca < 40$, the filaments become stiffer and occupy a greater cross-sectional area of the channel due to the increased restoring force. These stiff filaments block the mean flow, increasing the form drag. Conversely, at $Ca > 40$, the filaments become excessively flexible, and their proximity to the channel wall makes them incapable of disrupting the fluid flow effectively. As a result, the flow pattern resembles the base turbulent channel flow with smooth, no-slip walls, resulting in a drag reduction converging to $DR \approx 0$.

The drag reduction can also be characterized by the ratio of filament height to spacing, h_0/s. Figure 3.4(*a*) shows that as h_0/s increases for $Ca = 40$, the drag reduction initially increases, saturates at $h_0/s = 1/2$, and then decreases with further increasing h_0/s. Filamentous surfaces with $h_0/s = 1/4$ are sparser and have marginal mutual-sheltering effects (Raupach, 1992; Luhar *et al.*, 2008; Shao & Yang, 2005). This makes them more susceptible to flow-induced forces, causing them to be deflected towards the channel walls and thus resulting in a flow environment similar to the base turbulent channel flow. In contrast, filamentous surfaces with $h_0/s = 2$ are denser and experience significant mutual-sheltering effects, which reduces the filament deflection towards the channel walls and leads to increased form drag. Filaments distributed with moderate sparseness, $h_0/s = 1/2 - 1$, are more suitable for reducing skin-friction drag as the filaments do not excessively deflect nor increase the form drag.

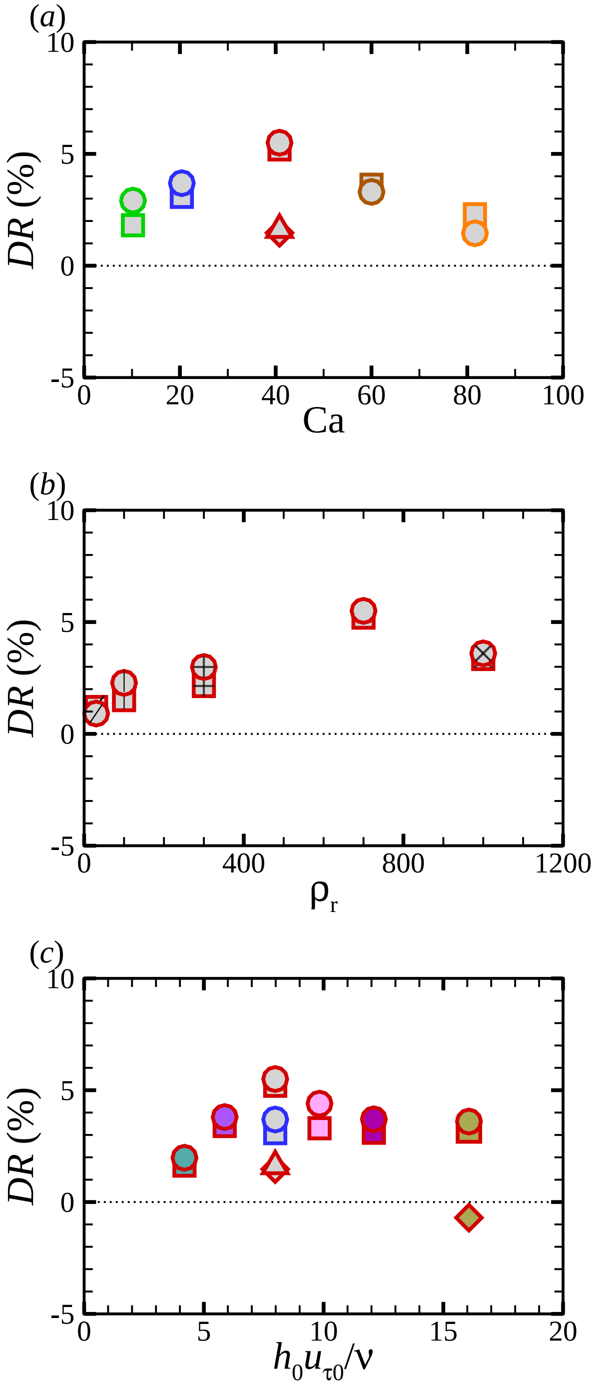

Figure 3.4: Effect of Cauchy number, density ratio, filament height and filament spacing on drag reductions: (*a*) Effect of Cauchy number, at $\rho_r = 700$, $h_0^{+0} \approx 8$ and 16, $h_0/s = 1/2, 1$ for Ca=10, 20, 60, 80; (*b*) effect of density ratio, at Ca=40, $h_0^{+0} \approx 8$, $h_0/s = 1/2, 1$; (*c*) effect of filament height, at $\rho_r = 700$, Ca=20, 40, and $h_0/s = 1/4, 1/2, 1, 2$. Symbol types as shown in Table 3.1.

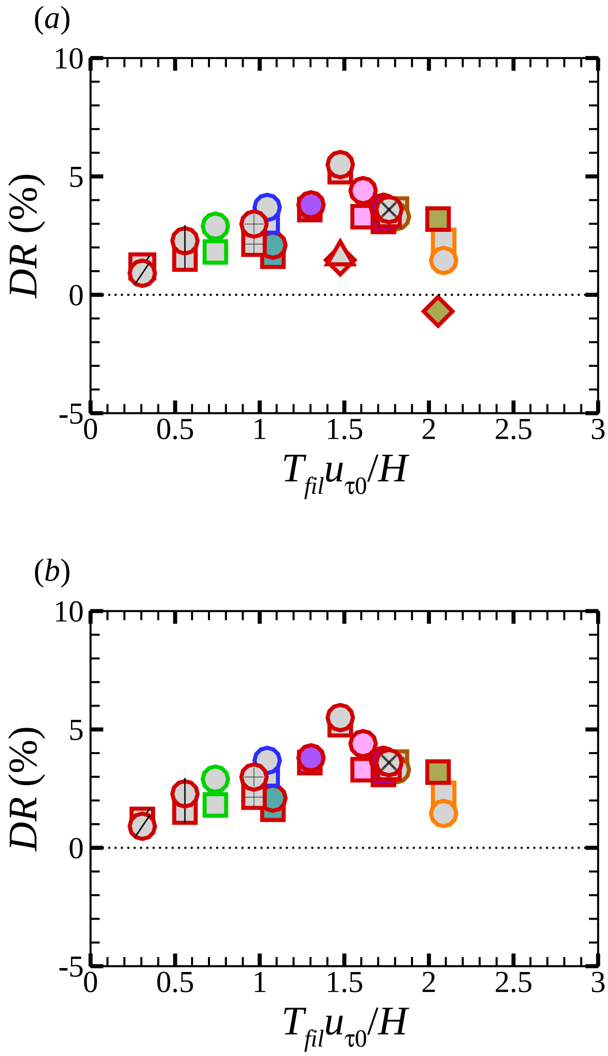

Figure 3.5: DRs as a function the characteristic time scale ratio for (*a*) all data points and (*b*) data points fallen into $1/4 < h_0/s < 2$ and $z^+_{eff} < 6$. Symbol types as shown in Table 3.1.

In addition, the drag reduction was explored for various density ratios of $\rho_r = 30, 100, 700, 1000$, at fixed filament height of $h^{+0} \approx 8$, height-to-spacing ratio of $h_0/s = 1/2$ and 1, Cauchy number of $Ca = 40$. Figure 3.4(*b*) shows that the drag reduction increases with increasing density ratio and reaches maximum drag reduction at a density ratio of $\rho_r = 700$, then decreases with further increasing density ratio. According to Sundin & Bagheri (2019), hairy filaments with a lower density ratio have a lower time scale of the motion so that the hairy filaments move faster and quickly comply with the turbulent structures, inducing the flux of turbulent fluctuation into the channel walls and leading to a significant drag increase, while hairy filaments with a higher density ratio have a larger time scale of the motion so that the hairy filaments deform slowly and modulate the turbulent structures, providing a minor drag increase. The drag reduction saturates at a moderately high density ratio, inspiring that a specific range of the filament time scale can lead to a favorable condition to reduce skin-friction drag reduction.

One particular interest of this study is to identify the key parameter that governs the trends of DR. The results presented in figures 3.4(*a*) and (*b*) show that neither Cauchy number nor density ratio can solely determine the DR trends, nor can filament height and height-to-spacing ratio in figure 3.4(*c*). Therefore, DR trends cannot be determined by a single parameter. In an effort to seek a determining parameter of DR trend, this study attempts to derive a prominent dimensionless parameter combining those individual parameters. In this effort, the characteristic time scale ratio, $T_{fil}u_{\tau 0}/H$, was derived, as explained in the previous section. This simplifies the prediction of DR trends. Figure 3.5(*a*) shows that the drag reductions fall on top of each other except for excessively sparse ($h_0/s \lesssim 1/4$) or dense filamentous surfaces ($h_0/s \gtrsim 2$) and the filamentous layer protruding above the demarcation of the hydraulic-smooth layer ($z^+ > 6$).

Based on this observation, one can suggest criteria that determine the DR trends with $T_{fil}u_{\tau 0}/H$, including moderate sparseness of the filamentous surfaces ($1/4 < h_0/s < 2$) and the filamentous layer determined below the demarcation of the hydraulic-smooth layer ($z^+_{eff} < 6$). The drag reductions obtained within this criteria show a collapse, as shown in figure 3.5(*b*). The highest drag reduction occurs at around $T_{fil}u_{\tau 0}/H \approx 1.4 - 1.5$. This finding suggests that when

T_{fil} latches onto a time scale $1.4 - 1.5$ times higher than the time scale of the largest eddies of the base turbulent channel flow, the drag reduction saturates. For lower time scale ratios, T_{fil} cannot latch onto the time scale of the largest eddies and instead latches onto the time scale of eddies larger than the channel allows. For higher time scales, T_{fil} latches onto the smaller scale turbulent eddies, and the drag reduction becomes less effective.

3.4 Turbulence Statistics

This study aims to investigate the influence of hairy surfaces on the modulation of turbulence dynamics and the resulting drag reduction. To achieve this, this study analyzes turbulence statistics and compare them with those obtained from the base turbulent channel flow with no-slip, smooth channel walls. Due to the spatial variability of wall structures, flows over hairy surfaces do not always exhibit homogeneity in a certain plane parallel to the wall. To overcome this issue, this study adopted an ensemble averaging, which involves averaging the wall-parallel plane in regards to the periodic pattern of the wall surfaces (Oikawa & Meng, 1995; Coceal *et al.*, 2007; Mejia-Alvarez & Christensen, 2013; Toloui *et al.*, 2019; Mangavelli *et al.*, 2021; Durbin, 2023). This technique isolates typical features of the flow fields from a relatively large number of events (Coceal *et al.*, 2007). The definition of the ensemble averaging for a fluid quantity $\phi(x, y, z)$ is expressed by

$$\phi(x_i, y_j, z) = \frac{1}{N_{enx}N_{eny}} \sum_{ii}^{N_{enx}-1} \sum_{jj}^{N_{enj}-1} \phi(x_{i+ii\left(\frac{N_x}{N_{enx}}\right)}, y_{j+jj\left(\frac{N_y}{N_{eny}}\right)}, z). \tag{3.4}$$

where N_x and N_y are the numbers of grid points in the streamwise and spanwise directions over the entire channel, and N_{enx}, N_{eny} are the numbers of ensemble patches in the streamwise and spanwise directions over the entire channel, respectively, which are determined by the sparseness of surface-textures. Therefore, the numbers of the grid points at each ensemble patch are obtained by dividing the number of grid points over the entire channel by the number of the ensemble patches, N_x/N_{enx} and N_y/N_{eny} in the streamwise and spanwise directions, respectively. The indices i, j in the left hand side of the equation 3.4 range from 0 to $N_x/N_{enx} - 1$ and from 0 to $N_y/N_{eny} - 1$, respectively.

A distinct feature of wall-bounded turbulence is to exhibit coherent structures that persist in time and space (Kline *et al.*, 1967; Robinson, 1991). Key observed coherent structures are self-sustaining and are generally represented by hairpin-shaped vortex packets comprising quasi-streamwise vortices and corresponding low- and high-streaks near the walls (Hamilton *et al.*, 1995; Waleffe, 1997; Tomkins & Adrian, 2003; Adrian, 2007; Graham & Floryan, 2021). The structures grow from the wall to the outer region (Zhou *et al.*, 1999), determining the dynamics of turbulence from the inner-layer and the outer region (Jimenez, 2018). The inner-scale turbulence can be represented by mean turbulence statistics with a proper normalization with inner-scale quantities, which are determined by the wall friction properties such as the kinematic viscosity and the friction velocity. Normalizing turbulence statistics by the inner-scale quantities enables to illustrate a general picture of the modulation of the internal dynamics of the wall-bounded turbulence.

In this chapter, an analysis of the wall-normal distributions of mean streamwise velocity, mean shear stress, mean turbulence intensity, and mean streamwise vorticity fluctuation, which are normalized using the wall-friction properties, will be focused. In addition, turbulence statistics investigated in terms of various filament parameters will be discussed.

3.4.1 Mean Streamwise Velocity Profile

The variation of the skin-friction resulting from the presence of surface texture is well known to be explained by the shift of the mean velocity profile in the logarithmic region. According to the classical theory (Clauser, 1954; Hama, 1954), the shift in the log-law intercept with the existence of surface textures from the log-law intercept of the base turbulent channel flow is indicative of the momentum deficit or surplus resulting from the surface textures. This shift can be interpreted as a measure of the drag penalty or reduction relative to a smooth wall, where a downward shift indicates drag increase, and an upward shift indicates drag reduction (Bechert *et al.*, 1997a; Spalart & McLean, 2011).

The log-law shift was investigated for various Cauchy numbers, filament height, and height-to-spacing ratios with a fixed density ratio of $\rho_r = 700$, as shown in figure 3.6. Figure 3.6 (*a*) shows the wall-normal distribution of the mean streamwise velocity normalized by the wall-

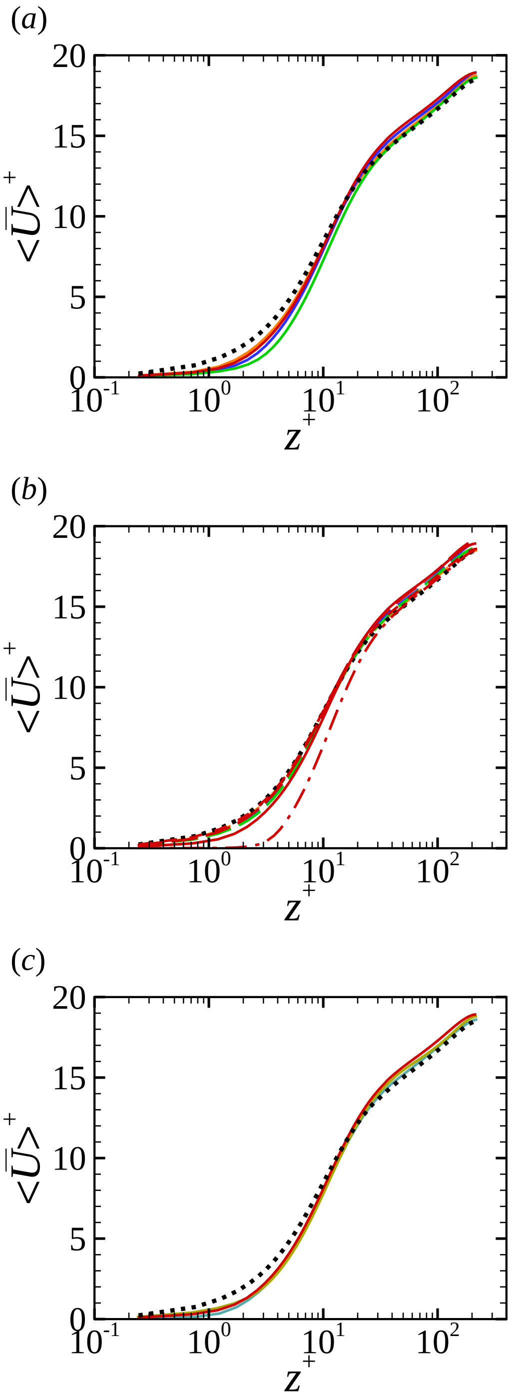

Figure 3.6: The wall-normal distribution of the mean streamwise velocity for (*a*) various Ca with $h_0/s = 1$, $h_0 \approx 8$, $\rho_r = 700$; (*b*) various Ca with $h_0/s = 1/2$, $h_0 \approx 8$, $\rho_r = 700$, and various $h_0/s = 1/4, 1/2, 1, 2$ with Ca= 40, $h_0 \approx 8$, $\rho_r = 700$; (*c*) various h_0 with Ca= 40, $h_0/s = 1$, $\rho_r = 700$. Line types as in Table 3.1.

friction velocity for various Cauchy numbers with the filament height of $h_0^{+0} \approx 8$ and the filament height-to-spacing ratio of $h_0/s = 1$. As expected from the classical theory, the drag reducing surfaces show the upward shift of the log-law intercept, and the extent of the upward shift follows the trends of DR. For various Cauchy number with $h_0^{+0} \approx 8$ and $h_0/s = 1$, the magnitude of DR increases with increasing Ca from 10, saturates at $Ca = 40$, and decays with further increasing Cauchy number, as pointed out in figure 3.4 (*a*). Similarly, it is observed that the extent of the upward shift of the log-law intercept in the mean streamwise velocity profile increases with increasing Ca from 10, saturates at $Ca = 40$, and decays with further increasing Cauchy number, as shown in figure 3.6 (*a*). The trends of the upward shift of the log-law intercept in consistent with the trends of DR uphold for various Cauchy numbers with $h_0/s = 1/2$ and $h_0^{+0} \approx 8$, as shown in figures 3.4 (*a*) and 3.6 (*b*).

According to the drag reduction curve with respect to h_0/s in figure 3.4 (*a*), the magnitude of DR increases as h_0/s increases from $1/4$, reaches the maximum at $h_0/s = 1/2 - 1$, and subsequently decreases with further increases in h_0/s. Figure 3.6 (*b*) illustrates that the degree of the upward shift of the log-law intercept also increases with increasing h_0/s from $1/4$, saturates at $h_0/s = 1/2 - 1$, and then decreases with further increases in h_0/s. The same feature of the shift in the log-law intercept is maintained for various filament height. Figure 3.6 (*c*) shows that the upward shift of the log-law intercept reaches a peak at $h^{+0} \approx 8$ and becomes lower at $h^{+0} \approx 4$ and 8 with fixed $h_0/s = 1$ and $Ca = 40$. The magnitudes of DR is consistent with the trend as shown in figure 3.4 (*c*).

In contrast to the trends represented by the mean streamwise velocity profiles in the logarithmic region, the mean streamwise velocity profiles near the wall no longer follow the trends of DR. Rather, it is featured by the filament deflections. In figure 3.6 (*a*), the mean streamwise velocity profiles are distinguished by Cauchy numbers at $z^+ \lesssim 10$. As Cauchy number increases, the mean flow is less deterred due to an increase in filament deflection led by the decrease in the restoring force of the filaments. The remarkable filament deflection results in a flow that resembles the base turbulent channel flow. Therefore, with increasing Cauchy number, the velocity profile near the wall gradually converges to the velocity profile of the base turbulent channel flow, as shown in figure 3.6 (*a*).

A similar feature is observed for decreasing h_0/s in figure 3.6 (*b*). As h_0/s decreases, the sparseness of the filaments increases, resulting in less mutual-sheltering effects (Raupach, 1992; Luhar *et al.*, 2008; Shao & Yang, 2005). With decreasing mutual-sheltering effects, the momentum flux from the overlying flow towards filamentous layer becomes notable, leading to an increase in the hydrodynamic force exerted on the filaments. Thus, the filaments deflect more toward the channel walls with decreasing h_0/s. As the filament deflection becomes greater with decreasing h_0/s, the filaments less obstruct the flow, and the flow ends up being similar to the base turbulent channel flow. Therefore, the mean streamwise velocity profile near the wall gradually converges to the mean streamwise velocity profile of the base turbulent channel flow at the lower near-wall region with decreasing h_0/s in figure 3.6 (*b*).

Although Cauchy number and the filament height-to-spacing ratio effectively distinguish the mean streamwise velocity profiles near the wall, the different filament heights do not seem to distinguish the mean streamwise velocity profiles near the wall, as shown in figure 3.6 (*c*). This is due to the self-similarity of the filament deflection in terms of various filament heights with fixed $h_0/s = 1$, as pointed out in figure 3.3. This indicates that the effects of the self-similarity shown in the filament deflection on turbulence are limited within the lower near-wall region ($z \lesssim 10$).

In light of the observed features of the mean streamwise velocity profile in the inner-layer, its trends show discernible features depending on whether it is from the near the wall to lower part of the buffer-layer ($z^+ \approx 10$) or from the upper part of the buffer layer to the logarithmic region. The effect of the filament deflection on the modulation of the mean streamwise velocity profiles is remarkable from the near the wall to the lower part of the buffer-layer, but it is difficult to find its relevance to the mean streamwise velocity profile from the upper part of the buffer-layer to the logarithmic region. In addition, it was shown that the effects of hairy surfaces on the modification of turbulence reaches above the buffer-layer, although the filaments move near

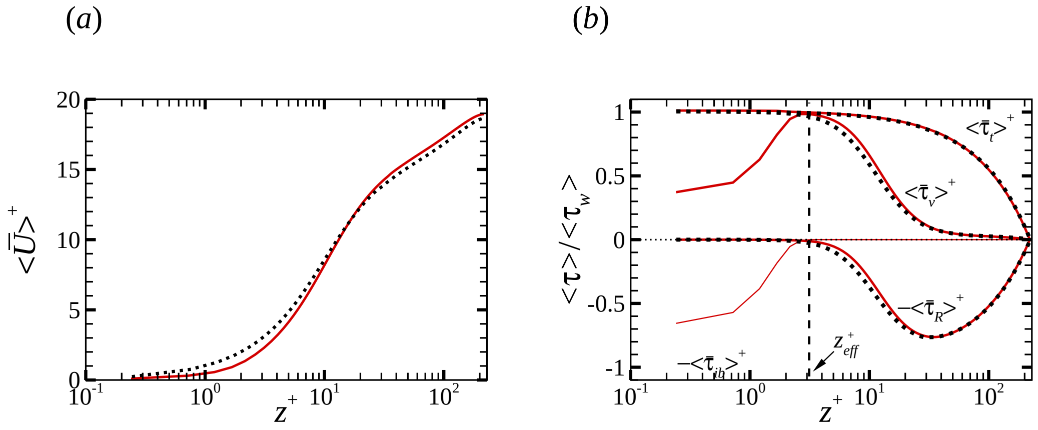

Figure 3.7: (*a*) Mean velocity profiles and (*b*) distribution of mean shear stresses in the wall-normal direction for a turbulent channel flow over hairy surfaces, with the ratio of solid density to the fluid density of $\rho_r = 700$, $h^{+0} \approx 8$, $h/s = 1$, $K_s^* = 1$, Ca=40. Line types as in Table 3.1.

the wall. The upward shift of the log-law intercept determines DR trends, suggesting that the modification of turbulence above buffer-layer is in charge of DR rather than the modification of the near-wall turbulence.

3.4.2 Distribution of Mean Shear Stress

To gain an understanding of the momentum transport in the presence of the hairy surfaces, the wall-normal distributions of shear stresses were explored. For steady, fully developed, turbulent channel flow with smooth, no-slip channel walls, the streamwise Reynolds-averaged momentum equation is given by

$$\frac{1}{\rho}\frac{d\bar{P}}{\partial x} = \frac{\partial}{\partial x}\left(\nu\frac{\partial \bar{U}}{\partial x} - \overline{u'u'} - \bar{U}\bar{U}\right) + \frac{\partial}{\partial y}\left(\nu\frac{\partial \bar{U}}{\partial y} - \overline{u'v'} - \bar{U}\bar{V}\right) + \frac{\partial}{\partial z}\left(\nu\frac{\partial \bar{U}}{\partial z} - \overline{u'w'} - \bar{U}\bar{W}\right) + \frac{1}{\rho}\bar{f}_{ibx}. \tag{3.5}$$

$\bar{U}$, $\bar{V}$, $\bar{W}$ and u', v', w' are the streamwise (x), spanwise (y), and wall-normal (z) components of Reynolds-averaged mean and fluctuating velocities, respectively, and $\bar{P}$ indicates the Reynolds-averaged mean pressure. Averaging over time and periodic pattern of the filamentous surface in the streamwise and spanwise direction, and integrating in the wall-normal direction from the channel center, $z = H$, to an arbitrary height, z ($z < H$), gives

$$-\frac{H}{\rho}\left\langle \frac{d\bar{p}}{dx} \right\rangle \left(1 - \frac{z}{H}\right) = \nu \left\langle \frac{\partial \bar{U}}{\partial z} \right\rangle - \langle \overline{u'w'} \rangle - \langle \bar{U}\bar{W} \rangle - \frac{1}{\rho}\int_{z}^{H} \langle \bar{f}_{ibx} \rangle dz. \tag{3.6}$$

where $\langle\ \rangle$ denotes averaging over the periodic pattern of the filamentous surface. Then the shear stress balance can be represented by

$$\tau_v + \tau_R + \tau_C + \tau_{fil} = \tau_t \left(1 - \frac{z}{H}\right), \tag{3.7}$$

$$\tau_v = \nu \left\langle \frac{\partial \bar{U}}{\partial z} \right\rangle,\ \tau_R = -\langle \overline{u'w'} \rangle,\ \tau_C = -\langle \bar{U}\bar{W} \rangle,\ \tau_t = -\frac{H}{\rho}\left\langle \frac{d\bar{p}}{dx} \right\rangle, \tag{3.8}$$

where τ_v is the viscous shear stress, τ_R is the Reynolds shear stress, τ_C is the convective shear stress, τ_t is the total shear stress. In the presence of the filaments, the shear stress balance contains the drag exerted by the filaments, τ_{fil}, which becomes effective at the wall-normal locations less than the effective thickness of the filamentous layer, $z < z_{eff}$, where the mean velocity gradient decreases, and the mean viscous shear stress drops with decreasing z, as shown in figure 3.7. This is because the momentum flux exerted on the fluid by means of the mean shear rate is transferred to the filaments at $z < z_{eff}$. The shear stress balance portrays that the sum of the streamwise shear stress, $\tau_t = \tau_v + \tau_R + \tau_C + \tau_{fil}$, at any given z is balanced by the force exerted by the pressure gradient above. It was observed that the convective shear stress (τ_C) was negligible for all cases studied. This is attributed to the uniform distribution of hairy surfaces, which reduces the effectiveness of the convective shear stress that is typically observed in anisotropic surface topologies (Finnigan, 2000; He *et al.*, 2022).

The wall-normal distributions of shear stress components were investigated for different Cauchy numbers, filament height-to-spacing ratios, and filament height with a fixed density ratio of $\rho_r = 700$. In figures 3.8 (*a*) – (*c*), the Reynolds shear stress reaches a peak at $z^+ \approx 30$ and gradually decays as the wall-normal distance from the wall decreases from 30 in wall units,

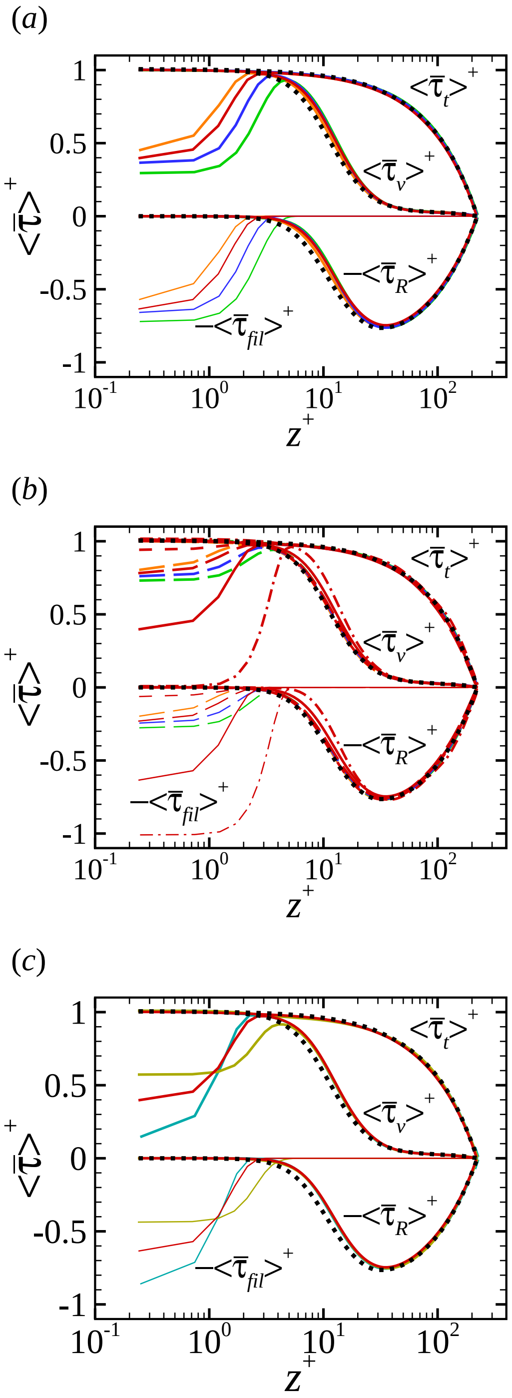

Figure 3.8: The wall-normal distribution of the mean shear stresses for (*a*) various Ca with $h_0/s = 1$, $h_0 \approx 8$, $\rho_r = 700$; (*b*) various Ca with $h_0/s = 1/2$, $h_0 \approx 8$, $\rho_r = 700$, and various $h_0/s = 1/4, 1/2, 1, 2$ with Ca$= 40$, $h_0 \approx 8$, $\rho_r = 700$; (*c*) various h_0 with Ca$= 40$, $h_0/s = 1$, $\rho_r = 700$. Line types as in Table 3.1.

while the viscous shear stress recovers and reaches a maximum at around $z = z_{eff}$. When further decreasing z from z^+_{eff}, the viscous shear stress rapidly drops, and the contribution of filament drag becomes more signified since the momentum flux that would have exerted on the fluids by means of the mean shear rate is transferred to the filaments.

The distribution of the shear stress below $z^+ \approx 10$ appears to be influenced by the filament parameters. As shown in figure 3.8(*a*), it is clearly shown that the magnitude of filament drag is distinguishable by Cauchy number. As the Cauchy number increases, the resistance of the filaments to the mean streamwise flow decreases, and thus the filaments are more deflective. Therefore, increasing Cauchy number leads to a monotonic decrease in the filament drag as well as the mean streamwise velocity profile below $z^+ \approx 10$, as observed in figures 3.6(*a*) and 3.8(*a*). The same feature also upholds for different Cauchy numbers with $h_0/s = 1/2$, $h_0^{+0} \approx 8$, in figure 3.8 (*b*).

Figures 3.8 (*b*) and (*c*) demonstrate different aspects of the shear stress distribution regarding the effects of h_0/s and h_0^+. In figure 3.8 (*b*), as h_0/s decreases, the filament drag is gradually reduced below $z^+ \approx 10$. Here, the decrease in h_0/s with a fixed filament height explains the increase in the filament spacing. As the filaments are located farther away from each other, the mutual-sheltering effect becomes marginal, leading to more hydrodynamic force exerted on the filament and thus more filament deflection (Raupach, 1992; Luhar *et al.*, 2008; Shao & Yang, 2005). The more deflective filaments give rise to the effective height of the filamentous layer (z_{eff}) closer to the channel wall. For lower z_{eff}, the mean flow is less obstructed. Therefore, decreasing h_0/s leads to less filament drag.

Figure 3.8 (*c*) illustrates the impact of varying filament heights while maintaining a constant height-to-spacing ratio of $h_0/s = 1$ on the distribution of shear stress. According to earlier study (Nepf, 2012; Sharma & Garcia-Mayoral, 2020*a*,*b*), the fluid momentum flux from the overlying flow to the filamentous layer is amplified due to the onset of Kelvin-Helmholtz like mixing-layer instability near the interface between the overlying flow and the filamentous layer. The active momentum flux leads to a significant increase in $\langle \bar{f}_{ibx} \rangle$ near $z \approx z_{eff}$, and as a result the filament drag, τ_{fil}, represented by the integral of $\langle \bar{f}_{ibx} \rangle$ from z to H (Last term of the equation 3.6), also increases significantly. However, as z decreases from z_{eff}, the increment of $\langle \bar{f}_{ibx} \rangle$ decreases due to lack of fluid momentum within the filamentous layer, resulting in marginal variation of the filament drag with a flat profile. Correspondingly, for taller filaments, z_{eff} appears far from the wall. This indicates that τ_{fil} starts increasing and is getting flat at higher z^+ compared to lower filaments, as shown in figure 3.8 (*c*). Furthermore, as the filament height increases, the magnitude of τ_{fil} decreases near the channel wall. This is due to the increased resistance to the flow penetration from the overlying flow into the filamentous layer comprising taller hairy filaments, which limit the active fluid momentum from reaching the filament bed.

Based on the findings of this study, it is possible to describe the distribution of shear stresses in the wall-normal direction by considering different filament parameters, including Cauchy numbers, filament height-to-spacing ratios, and filament height. Furthermore, the distinct features of this distribution can be observed depending on whether it appears below or above $z \approx 10$. It is worth noting that, despite variations in shear stress components along the wall-normal direction, the total shear stress remains balanced and conforms to the theoretical line of $\langle \tau_t \rangle^+ = (1 - z/H)$.

3.4.3 Mean Turbulence Intensities

Figure 3.9 shows the wall-normal distribution of the normalized u'_{rms}, v'_{rms}, w'_{rms} for different Cauchy numbers, filament height-to-spacing ratios (h_0/s), and filament height (h) with a fixed density ratio of $\rho_r = 700$. In figure 3.9 (*a*), the turbulence intensities resulted from various Cauchy numbers with $h_0/s = 1$ and filament height $h \approx 8$ show a prominent feature in terms of the intercomponent energy transfer. It is well established that the turbulent energy production occurs primarily in the streamwise component, and it is redistributed into the spanwise and wall-normal components by means of the pressure-strain correlation (Tennekes & Lumley, 1972; Pope, 2000). However, in the presence of the hairy surfaces, the turbulence intensity appears to

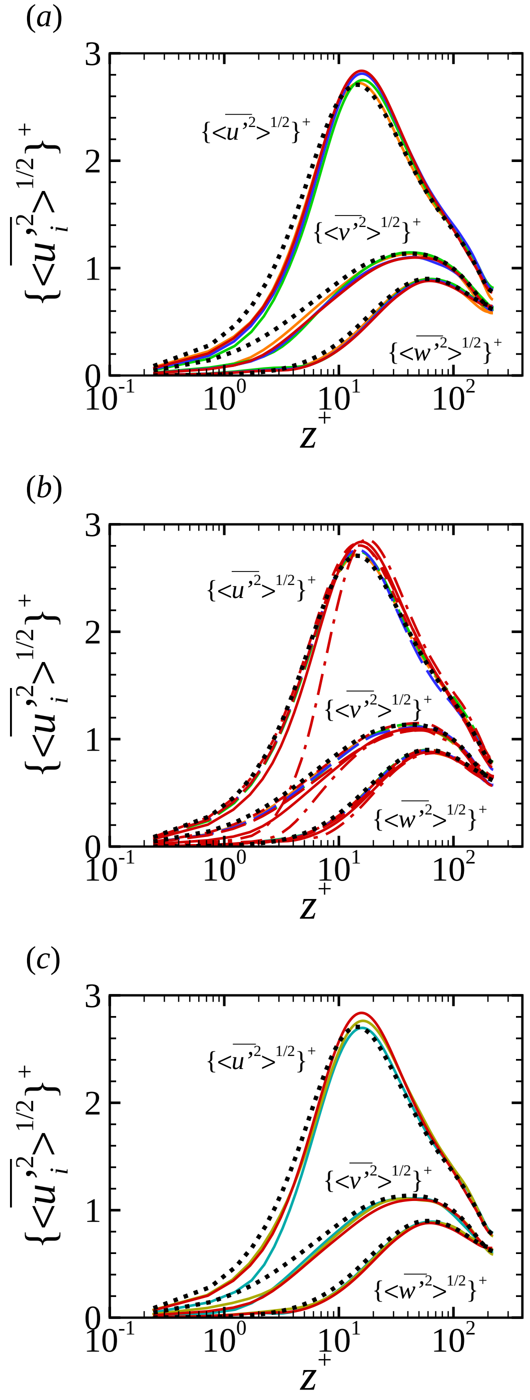

Figure 3.9: The wall-normal distribution of the mean turbulent intensities for (*a*) various Ca with $h_0/s = 1$, $h_0 \approx 8$, $\rho_r = 700$; (*b*) various Ca with $h_0/s = 1/2$, $h_0 \approx 8$, $\rho_r = 700$, and various $h_0/s = 1/4, 1/2, 1, 2$ with Ca$= 40$, $h_0 \approx 8$, $\rho_r = 700$; (*c*) various h_0 with Ca$= 40$, $h_0/s = 1$, $\rho_r = 700$. Line types as in Table 3.1.

be concentrated in the streamwise component at $z^+ \approx 15-16$, while the turbulence intensities are reduced in the spanwise and wall-normal components, as shown in figure 3.9 (*a*). The turbulent intensity piled up in the streamwise component can also be found in figures 3.9 (*b*) and (*c*) for various Cauchy numbers with $h_0/s = 1/2$ and filament height $h \approx 8$ as well as various filament heights with $h_0/s = 1$ and filament height $Ca = 40$. This implies that the existence of hairy filaments disrupts the redistribution of turbulent energy from the streamwise component to the other components. In fact, as will be shown later, the pressure-strain correlation, which is in charge of the inter-component energy transfer, is deterred by the hairy surfaces.

In contrast to the Cauchy number and filament height, the filament height-to-spacing ratio reveals distinct features in terms of u'_{rms} peak. Figure 3.9 (*b*) shows the distribution of turbulent intensities for each component for different h_0/s with fixed $Ca = 40$ and $h^{+0} \approx 8$. The results show a monotonic decrease in the magnitude of u'_{rms} peak as h_0/s decreases. Furthermore, the z location where u'_{rms} peak appears is gradually shifted towards the z location corresponding to the peak resulted from the base turbulent channel flow, as h_0/s decreases. This is because the sparse distribution of hairy filaments with decreasing h_0/s becomes indistinguishable from the base turbulent channel flow.

This observation implies that as h_0/s increases, the coherent structures represented by quasi-streamwise vortices are shifted away from the channel walls in the wall-normal direction. Earlier studies that investigated the mechanism of drag reduction with riblet surfaces suggested that the upward shift and reduced magnitude of the peak explained a decrease in the contribution of coherent structures to the momentum flux towards the walls, resulting in less shear stress and lower skin-friction drag (Choi, 1989; Vukoslavcevic *et al.*, 1992; Choi *et al.*, 1993; El-Samni *et al.*, 2007). However, in the case of the hairy surfaces, figures 3.9 (*b*) and 3.4 (*a*) show that the trend of upward shift of u_{rms} peak no longer follows the trend of drag reduction in terms of h_0/s, suggesting that the drag reduction mechanism for hairy surfaces differs from that for rigid riblet surfaces.

3.4.4 Mean Streamwise Vorticity Fluctuations

In wall-bounded turbulence, the streamwise vorticity fluctuation appears due to the presence of shear in the flow, which creates regions of velocity gradients that can lead to vortex stretching and tilting (Tennekes & Lumley, 1972). This process generates streamwise vortices with opposite signs, which are responsible for the generation of large scale coherent structures in wall-bounded turbulent flows. The presence of streamwise vorticity fluctuations, ω_x', is a notable feature of wall-bounded turbulence, and their dynamics play an important role in the transport of momentum, energy, and mass in the flow. Depending on the filament parameters, the hairy filaments can modulate those features represented by the streamwise vorticity fluctuations, leading to drag enhancement or drag reduction. To gain a deeper understanding of turbulence modulation by hairy surfaces, the wall-normal distribution of the streamwise vorticity fluctuation was explored for various Cauchy numbers, filament height-to-spacing ratios, and filament heights.

Figure 3.10 (*a*) shows the wall-normal distributions of the streamwise vorticity fluctuations normalized by viscous wall units for various Cauchy numbers with $h_0/s = 1$ and $h_0^{+0} \approx 8$. The plot shows two distinct peaks. The first peak appears within the viscous sublayer and the second peak appears in the buffer layer. For the first peak, its wall-normal location seems to depend on the filament deflection. The z location corresponding to the first peak is shifted upward with increasing Cauchy numbers. As Cauchy number increases, the restoring force of the filaments to the mean flow becomes more intense, lifting up the filament tips, and thus the effective thickness of the filamentous layer, z_{eff}, increases. As the effective height z_{eff} increases, the fluctuating streamwise vorticity is discharged away from the wall. In contrast, the z location corresponding to the second peak seems similar for $Ca = 10, 20, 40, 80$, but the magnitudes of the peak are discernible. The trends of the magnitudes of the second peak follow the DR trends, as shown in figures 3.10 (*a*) and 3.4 (*a*). This observation suggests that the extent of which the streamwise vorticity fluctuation decreases in the buffer layer corresponds to the level of DR achieved. The same features can also be found for various Cauchy numbers with $h_0/s = 1/2$ and $h_0^{+0} \approx 8$ as well as for various h_0^{+0} with fixed $h_0/s = 1$ and $Ca = 40$ in figures 3.10 (*b*) and (*c*).

In contrast, the magnitude of the streamwise vorticity fluctuations is discernible by h_0/s, as shown in figure 3.10 (*b*). A monotonic decreases in the streamwise vorticity fluctuation appears with increasing h_0/s at $10 \lesssim z^+ \lesssim 30$. This can also be expected by the trends of the turbulent intensity. With increasing h_0/s, a similar monotonic decrease in the magnitude of turbulent intensities was observed in figure figures 3.9 (*b*). As expected, the decrease in the spanwise and wall-normal velocity fluctuation components contributes to the streamwise vorticity fluctuation less than that obtained from the base turbulent channel flow.

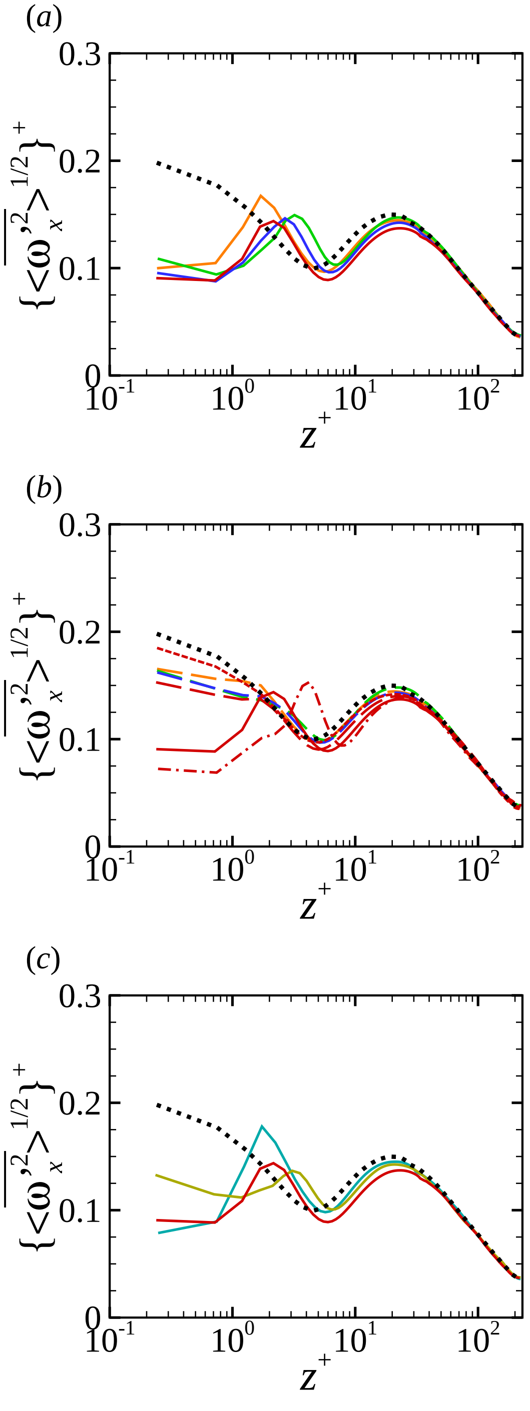

Figure 3.10: The wall-normal distribution of the streamwise vorticity fluctuations for (*a*) various Ca with $h_0/s = 1$, $h_0 \approx 8$, $\rho_r = 700$; (*b*) various Ca with $h_0/s = 1/2$, $h_0 \approx 8$, $\rho_r = 700$, and various $h_0/s = 1/4, 1/2, 1, 2$ with Ca$=$ 40, $h_0 \approx 8$, $\rho_r = 700$; (*c*) various h_0 with Ca$=$ 40, $h_0/s = 1$, $\rho_r = 700$. Line types as in Table 3.1.

CHAPTER 4

Mechanism of Skin-friction DR with Hairy Surfaces

4.1 Modulation of Intercomponent Energy Transfer

In wall-bounded turbulent flows, the viscous force directly influences the mean shear near the wall, leading to the production of turbulent kinetic energy. The turbulent energy is mostly produced in the streamwise conponent and then distributed into the cross-streamwise components (e.g. spanwise and wall-normal components) through intercomponent energy transfer, which is governed by the pressure-strain correlation. The pressure-strain correlation plays an important role on the spatial configurations of the coherent structures (Jeong & Hussain, 1995; Hwang & Sung, 2017) and the regeneration of the quasi-streamwise vortices in the self-sustaining near-wall cycle (Cho *et al.*, 2018), upholding the characteristics of near-wall turbulence. It can be conjectured that an appropriate disturbance of the pressure-strain correlation could be an effective pathway to suppress the quasi-streamwise vortices. Accordingly, the suppression of the quasi-streamwise vortices mitigates wall turbulence and thus leads to the reduction in skin-friction drag, as observed in the previous studies (Kravchenko *et al.*, 1993; Choi *et al.*, 1994; Orlandi & Jimenez, 1994). Thus, the attenuation of the pressure-strain correlation serves to limit the impact of quasi-streamwise vortices on the generation of skin-friction and thus lead to its suppression. A growing body of evidence indicated that various flow control techniques achieved the skin-friction DR via effective suppression of pressure-strain correlation (Xu & Huang, 2004; Moosaie & Manhart, 2016; Fujimura *et al.*, 2017; Ma *et al.*, 2022; Umair *et al.*, 2022). Hence, suppressing the pressure-strain correlation can be deemed as an effective pathway to achieve the skin-friction DR.

In addition, the exploration of the intercomponent energy transfer and its modulation with the presence of hairy filaments would offer valuable insights into the underlying mechanism of skin-friction DR with hairy surfaces. In this study, the budgets for the component of the Reynolds stress tensor, $\langle u_i' u_j' \rangle$, are computed. Each budget term is analyzed to assess its influence on the transport of the Reynolds stresses. Of particular interest is the pressure-strain correlation term, which is the focal point of analysis. To gain a better understanding of how intercomponent energy transfer is modulated, a comparison is made between the pressure-strain correlation in the presence of hairy filaments and that in the base turbulent flow. To facilitate this analysis, the 'nominal' case of D700Ca40h8s8 (as described in Table 3.1) is selected regarding the result that the given DR falls into the uppermost range ($5.3-5.4\%$). By focusing on this specific case and comparing it to the base turbulent channel flow, the modulation of intercomponent energy transfer can be clearly elucidated, without a need for the exploration of all the individual cases.

4.1.1 Budgets of Reynolds Stress Tensor

The analysis in the budget terms of the Reynolds stresses enables a detailed examination of their distinct contributions to gain/loss of the Reynolds stresses. The transport equations for the Reynolds stresses are derived through a systematic process averaging of the Navier-Stokes equations, followed by the derivation of equations specifically addressing the fluctuating stresses. Subsequently, these derived equations are averaged over the periodic pattern of the filamentous surface and time to obtain the final form of the budget equations for the Reynolds stresses. This methodical approach ensures a comprehensive understanding of the role of each budget term in terms of the transport of the Reynolds stresses in turbulent flows. For incompressible turbulent flow, the budget equation for the Reynolds stresses is written as

$$B_{ij} = \frac{D}{Dt}\overline{u_i'u_j'} = P_{ij}^R + D_{ij}^R + T_{ij}^R + \Pi_{ij}^R + F_{ij}^R. \tag{4.1}$$

In this equation, the terms on the right-hand side represent the contributions from various physical processes, which are defined as

$$P_{ij}^R = -\overline{u_i'u_k'}\frac{\partial \bar{U}_j}{\partial x_k} - \overline{u_j'u_k'}\frac{\partial \bar{U}_i}{\partial x_k}, \tag{4.2}$$

$$D_{ij}^R = -2\nu\overline{\frac{\partial u_i'}{\partial x_k}\frac{\partial u_j'}{\partial x_k}}, \tag{4.3}$$

$$T_{ij}^R = -\frac{\partial}{\partial x_k}\overline{u_i'u_j'u_k'} - \frac{1}{\rho}\frac{\partial}{\partial x_k}\left[\overline{p'u_i'}\delta_{jk} + \overline{p'u_j'}\delta_{ik}\right] + \nu\frac{\partial^2}{\partial x_k^2}\overline{u_i'u_j'}, \tag{4.4}$$

$$\Pi_{ij}^R = \overline{p'\left(\frac{\partial u_i'}{\partial x_j} + \frac{\partial u_j'}{\partial x_i}\right)}, \tag{4.5}$$

$$F_{ij}^R = \frac{1}{\rho}\left(\overline{f_{ib,i}'u_j'} + \overline{f_{ib,j}'u_i'}\right). \tag{4.6}$$

where δ_{ij} is Kronecker's delta in this budget equation. To be specific, the shear production term (P_{ij}^R) accounts for the generation of the Reynolds stresses due to velocity gradients. The viscous dissipation term (D_{ij}^R) represents the dissipation of energy within the turbulent flow due to viscous effects. The transport term (T_{ij}^R) encompasses the turbulent transport, pressure transport, and viscous transport components, which collectively contribute to the transport of the Reynolds stresses. The pressure-strain correlation term (Π_{ij}^R) characterizes the interaction between the fluctuating pressure field and the fluctuating velocity gradients, in charge of the redistribution of Reynolds stresses from the streamwise to the cross-streamwise components. Finally, the transport by the hairy filaments (F_{ij}^R) captures the transport of the Reynolds stresses associated with the presence of filaments within the turbulent flow.

Figures 4.1 (*a*)–(*d*) show the wall-normal distribution of the budget terms for the Reynolds normal and shear stresses. The budgets are normalized by the fluid viscosity and the friction velocity of the base turbulent channel flow, for the quantitative comparison to the base turbulent channel flow. The production of turbulence only appears in the streamwise direction among the Reynolds normal stresses due to the mean shear dominantly existing in the streamwise direction. In figure 4.1 (*a*), it can be observed that there is a notable decrease in the magnitude of turbulence production within the near-wall region, which is a prominent signature of the reduction in skin-friction drag. Figures 4.1 (*a*)–(*c*) illustrate the reduction in all normal components of $\langle \Pi_{ii}^{R} \rangle^{+0}$. This indicates that the presence of the filaments impedes the distribution of the streamwise Reynolds normal stress into its cross-straemwise components. Consequently, the mechanism responsible for sustaining the cross-streamwise Reynolds normal stresses is also diminished. Therefore, less effective distribution of the intercomponent transfer weakens the source that would have maintained the cross-streamwise Reynolds normal stresses. Accordingly, this explains that turbulence intensities are piled up in the streamwise component and reduced in the cross-streamwise components as shown in figure 3.9.

Next, one can pose a question on why the modulation of turbulence is remarkable within the near-wall region and less in the outer region. One plausible answer is that at low friction Reynolds number, the intercomponent energy transfer primarily takes place in the near-wall region where the energy-containing eddies are predominantly existing at low friction Reynolds numbers (Hwang, 2013). Smits *et al.* (2011) noted that the main contribution to turbulence production comes from the near-wall region at low Reynolds number ($Re_\tau \lesssim 4200$). Accordingly, the friction Reynolds number set to $Re_\tau \approx 221$ in this study is considered a relatively low Reynolds number where the energy-containing eddies involving the quasi-streamwise vortices, in charge of the skin-friction generation, are dominantly residing in the near-wall region (Choi *et al.*, 1993, 1994; Orlandi & Jimenez, 1994; Hwang, 2013; deGiovanetti *et al.*, 2016). In figures 4.1 (*a*)–(*c*), the modulation of $\langle \Pi_{ii}^{R} \rangle^{+0}$ is predominantly observed within the near-wall region. This observation suggests that the presence of hairy filaments hinders the intercomponent energy transfer between energy-containing eddies by disrupting the correlation between pressure fluctuations and fluctuating velocity gradients in the near-wall region. Consequently,

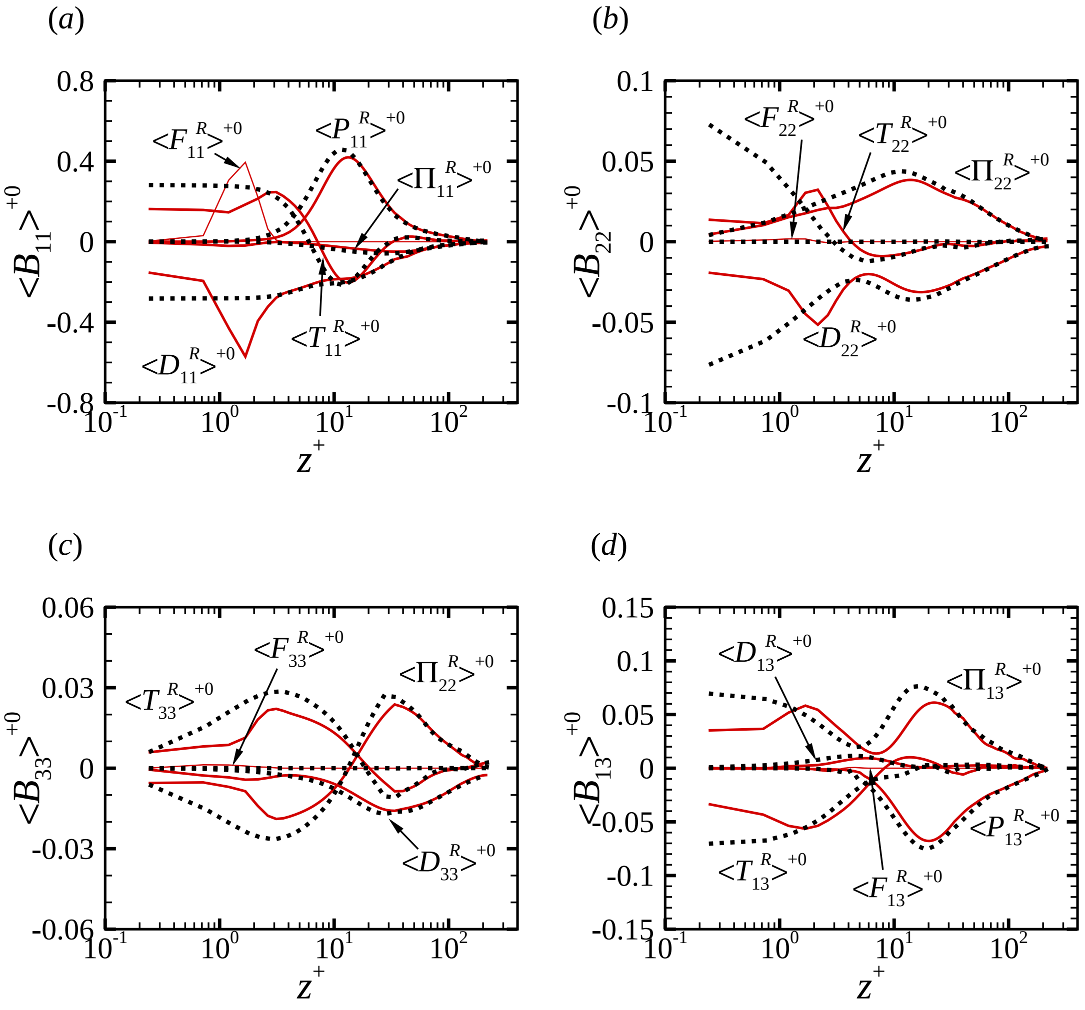

Figure 4.1: The wall-normal distribution of the Reynolds stress budgets, (*a*) B_{11}, (*b*) B_{22}, (*c*) B_{33}, and B_{13} for a hairy surface corresponding to the case of D700Ca40h8s8. For comparison, the same quantities are plotted for the base turbulent channel flow. The red solid line (——) and black dashed line (......) denote the results from D700Ca40h8s8 and the base turbulent channel flow with no-slip, smooth walls, respectively.

the weakened intercomponent energy transfer barely sustains the cross-streamwise turbulence. With the diminishing cross-streamwise turbulence, the influence of quasi-streamwise vortices decreases, and the skin-friction drag is reduced.

The transport of the Reynolds normal stresses by the hairy filaments, $\langle F_{ii}^{R} \rangle^{+0}$, becomes significant at $z \lesssim z_{eff}$ only in the streamwise direction but marginal in the spanwise and wall-normal directions, as shown in figures 4.1 (*a*)–(*c*). Figure 4.1 (*a*) shows that $\langle F_{11}^{R} \rangle^{+0}$ adds the Reynolds stress into the fluid flow. Note that the magnitude of viscous dissipation, $\langle D_{11} \rangle^{+0}$, abruptly increases in the region where $\langle F_{11}^{R} \rangle^{+0}$ is dominant, indicating that the Reynolds stresses transported by the hairy filaments are directly dissipated by the fluid viscosity at $z \lesssim z_{eff}$.

In figure 4.1 (*d*), the Reynolds shear stress budgets, represented as B_{13}, exhibit similar characteristics to those demonstrated by the Reynolds normal stresses. The production of Reynolds shear stress is suppressed within the near-wall region, consistent with the suppression of Reynolds shear stress observed in the near-wall region in Figure 3.8 (*a*). The pressure-strain correlation, represented by $\langle \Pi_{13} \rangle^{+0}$, is primarily balanced out by turbulence production, $\langle P_{13} \rangle^{+0}$, above $z^{+} \approx 8$, and by the transport term, $\langle T_{13} \rangle^{+0}$, below $z^{+} \approx 8$, respectively.

Within the vicinity of the interface between the overlying flow and the filamentous layer, specifically within the range of $1.5 \lesssim z^{+} \lesssim 5$, the values of $\langle \Pi_{13} \rangle^{+0}$ and $\langle T_{13} \rangle^{+0}$ obtained with the presence of hairy filaments surpass those obtained in the base turbulent channel flow. This observation suggests that the presence of hairy filaments enhances turbulence in this specific region, which might be attributed to the influence of shear instability such as Kelvin-Helmholtz instability. Shear instability typically emerges at the interface between the overlying flow and the filamentous layer (Raupach *et al.*, 1996; Nepf, 2012). Near the interface, the momentum flux, flowing from the overlying flow to the filamentous layer and vice versa, is accelerated by the shear instability, enhancing turbulence.

However, the enhanced turbulence is localized near the interface due to the mitigating effect of the wall in close proximity. The presence of the wall directly suppresses shear instability, as observed in previous studies involving short filamentous layers (Sharma & Garcia-Mayoral, 2020*a*,*b*). Consequently, the increase in $\langle \Pi_{13} \rangle^{+0}$ and $\langle T_{13} \rangle^{+0}$ is limited to the vicinity of the interface and is reduced near the wall due to the influence of the wall effect.

4.2 Modulation of Interscale Energy Transfer

The Richardson-Kolmogorov energy cascade theory (Kolmogorov, 1941*a*,*b*) is universally acknowledged as the well-established theoretical framework elucidating the multi-scale dynamics of turbulent energy transfer in incompressible, homogeneous, isotropic turbulence. According to this theory, turbulent kinetic energy originating from the integral length scale undergoes subsequent transport to smaller scales, ultimately being dissipated by the fluid viscosity at the dissipative scale. In the presence of walls, the viscous forces directly impacts the mean shear in the vicinity of the wall, inducing the production of turbulent kinetic energy. As a result of the turbulence production, energy-containing motions (e.g. coherent structures) manifest across various length scales, and the turbulent kinetic energy is transferred across the eddies in different scales, effectively demonstrating the interscale energy transfer.

Finnigan (2000) highlighted that the presence of canopy elements (e.g. vegetative elements in terrestrial or aquatic environments) disrupts the energy cascade process. When the mean flow undergoes the drag exerted by the canopy, the kinetic energy of the mean flow is converted into both heat and fine-scale turbulence within the wake scale of the canopy elements. This phenomenon, in which large-scale energy circumvents the energy cascade and is directly transferred to secondary flows, is referred to as the 'spectral shortcut' (Brunet *et al.*, 1994). Consequently, instead of entering the inertial subrange, the mean kinetic energy is redeposited into turbulent kinetic energy within the wake scales via the energy transport by canopy elements. The wake kinetic energy then generates the turbulent kinetic energy at smaller scales. The energy contained in the eddies of dissipative scales is dissipated in the canopy layer, where an abundant source of viscous dissipation from the intense shear layer exist along the canopy elements.

Considering the arguments from the earlier studies above, it is reasonable to hypothesize that the presence of hairy filaments in turbulent channels may exhibit the characteristics akin to the spectral shortcut, disrupting the energy cascade and thus reducing turbulence. Moreover, the movements of drag-reducing hairy filaments are primarily concentrated within the viscous sublayer, which is characterized by a significant amount of viscous dissipation. This observation provides valuable insights into the mechanism of skin-friction drag reduction, suggesting that the large-scale energy transferred to small scales through the hairy filaments is dissipated by fluid viscosity within the viscous sublayer. To comprehend the interscale energy transfer in the presence of hairy filaments, the wall-normal distribution of the budgets of mean kinetic energy and turbulent kinetic energy were examined. In addition, spectral analysis was performed to further investigate which scales are responsible for modulating the interscale energy transfer in the presence of the hairy filaments.

4.2.1 Budgets of Mean and Turbulent Kinetic Energy (MKE and TKE)

The analysis of the budget terms of the mean kinetic energy (MKE), $K^M = \frac{D}{Dt}\bar{U}_i\bar{U}_i$, and turbulent kinetic energy (TKE), $K^T = \frac{D}{Dt}\overline{u_i'u_i'}$, enables a detailed examination of their distinct contributions to gain/loss of the kinetic energy that appears in the mean flow and turbulence. The budget equations for MKE and TKE are derived through a systematic process involving ensemble averaging of the Navier-Stokes equations. For incompressible turbulent flow, the budget equation for MKE is written as

$$K^M = \frac{D}{Dt}\bar{U}_i\bar{U}_i = P^M + D^M + T^M + F^M. \tag{4.7}$$

where

$$P^M = \overline{u_i'u_j'}\frac{\partial \bar{U}_i}{\partial x_j}, \tag{4.8}$$

$$D^M = -2\nu\bar{S}_{ij}\frac{\partial \bar{U}_i}{\partial x_j}, \tag{4.9}$$

$$T^M = -\frac{\partial}{\partial x_j}\overline{u_i'u_j'}\bar{U}_i - \frac{1}{\rho}\frac{\partial}{\partial x_i}\bar{P}\bar{U}_i + 2\nu\frac{\partial}{\partial x_i}\bar{U}_j\bar{S}_{ij}, \tag{4.10}$$

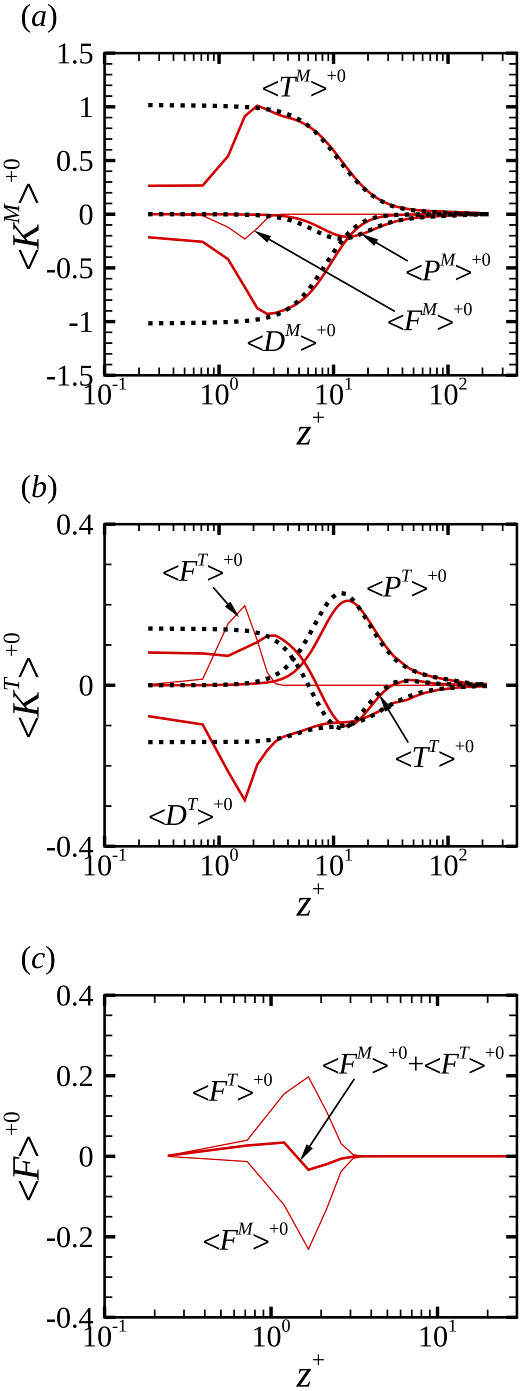

Figure 4.2: The wall-normal distribution of (*a*) MKE budgets, (*b*) TKE budgets, and (*c*) the transports of MKE and TKE by the hairy filaments and their sum for the case of D700Ca40h8s8. For comparison, the same quantities are plotted for the base turbulent channel flow. The red solid line (——) and black dashed line (......) denote the results from D700Ca40h8s8 and the base turbulent channel flow with no-slip, smooth walls, respectively.

$$F^M = \frac{1}{\rho}\bar{F}_{ib,i}\bar{U}_i, \tag{4.11}$$

where $\bar{S}_{ij} = \frac{1}{2}\left(\partial\bar{U}_i/\partial x_j + \partial\bar{U}_j/\partial x_i\right)$. The terms on the right-hand side represent the MKE production (P^M), viscous dissipation of MKE (D^M), MKE transport (T^M) which encompasses the transports by turbulence, mean pressure, fluid viscosity, and the MKE transport by the hairy filaments (F^M). Similarly, the budget equation for TKE can be written as

$$K^T = \frac{D}{Dt}\overline{u_i'u_i'} = P^T + D^T + T^T + F^T. \tag{4.12}$$

The terms on the right-hand side represent the TKE production (P^T) which has the same form but opposite sign ($P^T = -P^M$), viscous dissipation of TKE (D^T), TKE transport (T^T) which encompasses the transports by turbulence, mean pressure, fluid viscosity, and the TKE transport by the hairy filaments (F^T), which are expressed by

$$P^T = -\overline{u_i'u_j'}\frac{\partial\bar{U}_i}{\partial x_j}, \tag{4.13}$$

$$D^T = -2\nu\overline{s_{ij}'\frac{\partial u_i'}{\partial x_j}}, \tag{4.14}$$

$$T^T = -\frac{1}{2}\frac{\partial}{\partial x_j}\overline{u_i'u_i'u_j'} - \frac{1}{\rho}\frac{\partial}{\partial x_i}\overline{p'u_i'} + 2\nu\frac{\partial}{\partial x_i}\overline{u_j's_{ij}'}, \tag{4.15}$$

$$F^T = \frac{1}{\rho}\overline{f_{ib,i}'u_i'}, \tag{4.16}$$

where $s_{ij}' = \frac{1}{2}\left(\partial u_i'/\partial x_j + \partial u_j'/\partial x_i\right)$. The pressure-strain correlation terms for both MKE and TKE are eliminated due to the continuity $\left(\bar{U}_i/\partial x_i = 0, u_i'/\partial x_i = 0\right)$.

Figure 4.2 shows the wall-normal distribution of the MKE, TKE, and energy transport by the hairy filaments. The budgets are normalized by the fluid viscosity and the friction velocity of the base turbulent channel flow, for the quantitative comparison with the base turbulent channel flow. As per Tennekes & Lumley (1972), vortex stretching occurs due to the conservation of angular momentum. This stretching results in positive work done by the strain rate on the vortex, leading to the transfer of energy into smaller scales. This transfer is evident from the production of MKE in the MKE budget equation and the production of TKE in the TKE budget equation. These terms exhibit the same magnitude but opposite sign, indicating that turbulence receives energy from the mean flow through the strain rate, depleting an equivalent amount of MKE. This characteristic of interscale energy transfer persists even in the presence of the hairy filaments. In figures 4.2 (*a*) and (*b*), the production of MKE and TKE demonstrates the same magnitude but opposite signs. In addition, the production of TKE decreases in the buffer layer to the same extent as the depletion of MKE production. This observation suggests that the positive work done by the strain rate is not disrupted by the hairy filaments and is effectively utilized for the energy transfer from the mean flow to turbulence.

Figure 4.2 (*a*) shows that as the wall-normal distance decreases, the production term $\langle P^M \rangle^{+0}$ and the transport term $\langle T^M \rangle^{+0}$ in MKE budget reach their peaks at around $z \approx z_{eff}$. Below z_{eff}, the transport of MKE by the hairy filaments, represented by $\langle F^M \rangle^{+0}$, acts as a sink, and its magnitude becomes significant. As MKE is transported by the hairy filaments, the decaying rate of $\langle D^M \rangle^{+0}$ becomes steeper in the region where $\langle F^M \rangle^{+0}$ is substantial. This can be attributed to the fact that the MKE, which would have been dissipated by fluid viscosity, is instead absorbed by the hairy filaments and utilized to drive their motion. In figure 4.2 (*b*), the transport of TKE by the hairy filaments, denoted as $\langle F^T \rangle^{+0}$, acts as a source and its magnitude becomes substantial at $z \lesssim z_{eff}$. It is worth noting that the magnitude of viscous dissipation, $\langle D^T \rangle^{+0}$, abruptly increases in the region where $\langle F^T \rangle^{+0}$ is significant. This indicates that the energy transported by the hairy filaments from the mean flow to turbulence is directly dissipated by fluid viscosity at $z \lesssim z_{eff}$.

In figure 4.2 (*c*), it can be observed that the energy transport terms, $\langle F^M \rangle^{+0}$ and $\langle F^T \rangle^{+0}$, do not balance out locally with each other. However, when considering the sum of these terms along the wall-normal direction, it becomes evident that their contributions cancel out, resulting in a net balance of zero. This implies that their respective effects are observed in different regions. The sink peak $\left(\langle F^M\rangle^{+0}_{peak}\right)$ emerges just above the source peak $\left(\langle F^T\rangle^{+0}_{peak}\right)$, as also observed in a different wall-resolved LES study He *et al.* (2022). This indicates that the region where the MKE is extracted by the filaments is located above the region where the energy is redeposited into turbulence. It is also implied that the hairy filaments extract large scale energy from the overlying flow and transfer it to the turbulence of dissipative scales within the filamentous layer. Subsequently, the redeposited energy is dissipated within the viscous sublayer, as depicted in figure 4.2 (*b*).

In theory, the balance of all budget terms in the MKE and TKE transport equations should be zero, as it is governed by the conservation of energy. However, in numerical simulations, achieving a perfect balance might not be possible, and there could be a residual term resulting from various factors, such as spatial and temporal discretization schemes. In this study, the observed residual term is $O(10^-4) - O(10^-3)$ in wall units, which is considered acceptable within the numerical accuracy.

4.2.2 One-dimensional Energy Spectra

The modulation of interscale energy transfer by the hairy filaments can be examined through the one-dimensional energy spectra and comparing them to the reference data obtained from the base turbulent channel flow. The one-dimensional energy spectra with respect to the streamwise and spanwise wavenumbers (k_x and k_y) can be defined as follows:

$$E_{ii}(k_x, z) = \frac{2}{\pi}\langle\overline{\tilde{u_i'}\,(k_x, k_y, z)\,\tilde{u_i'}^{**}\,(k_x, k_y, z)}\rangle, \tag{4.17}$$

$$E_{ii}(k_y, z) = \frac{2}{\pi}\langle\overline{\tilde{u_i'}\,(k_x, k_y, z)\,\tilde{u_i'}^{**}\,(k_x, k_y, z)}\rangle, \tag{4.18}$$

where $\tilde{u_i'}\,(k_x, k_y, z)$ is the two-dimensional Fourier transform of $u_i'\,(k_x, k_y, z)$,

$$\tilde{u_i'}\,(k_x, k_y, z) = \int_{-\infty}^{\infty}\int_{-\infty}^{\infty} u_i'\,(x, y, z)\,exp\left[-2\pi\sqrt{-1}\,(k_x x + k_y y)\right] dxdy. \tag{4.19}$$

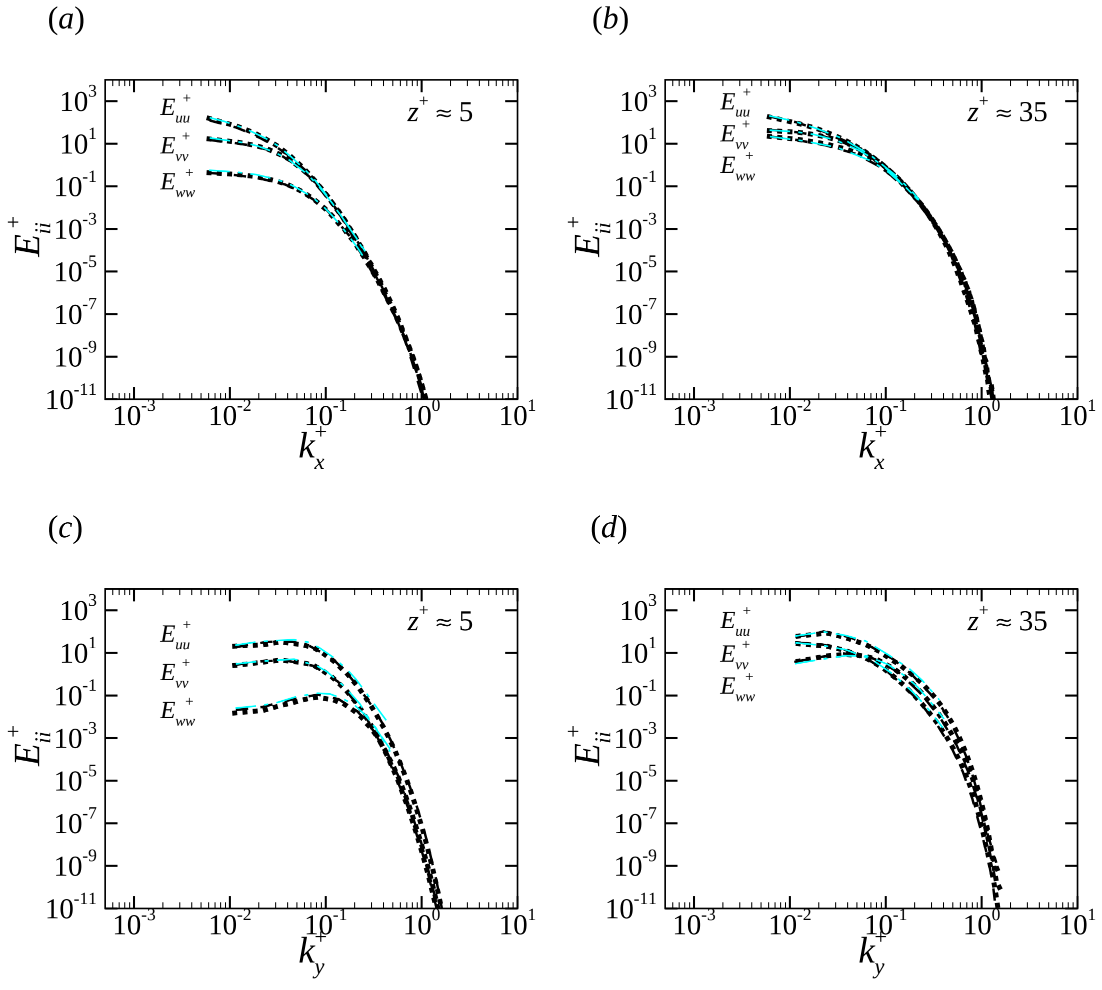

Figure 4.3: One-dimensional energy spectra with respect to (*a*), (*b*) the streamwise wavenumber, k_x, and (*c*), (*c*) the spanwise wavenumber, k_y. The spectra is present at the wall-normal positions included in (*a*), (*c*) the near-wall region ($z^+ \approx 5$) and (*b*), (*d*) the lower part of the log-layer ($z^+ \approx 35$). Line types: The present LB DNS simulation with $GR = 4$, …… the previous LB DNS with $GR = 4$, – –, the pseudo-spectral DNS, –·– The reference lines are obtained from the appendix of an earlier study (Rastegari & Akhavan, 2018).

The transform is obtained using a real-to-complex Fast Fourier Transform (FFT) method (Frigo & Johnson, 1998), and the superscript $**$ denotes complex conjugation.

Before analyzing the one-dimensional energy spectra obtained in the presence of the hairy filaments, it is necessary to verify the computation method for the one-dimensional energy spectra using DNS data from the base turbulence channel flow. Figure 4.3 presents the one-dimensional energy spectra of the base turbulent channel flow obtained from the present LB DNS with $GR = 4$, the previous LB DNS with $GR = 4$ and the pseudo-spectral DNS at $z^+ \approx 5$ and $z^+ \approx 35$. The two latter cases are found in the appendix of an earlier study (Rastegari & Akhavan, 2018). The difference between the present LB DNS and the previous LB DNS is the choice of the forcing function employed in the LB equation. While the previous LB DNS study utilized an outdated and less accurate forcing function, its result was still reasonable enough as a reference. Figure 4.3 shows that the one-dimensional energy spectra of the base turbulent channel flow obtained from the present study agree well with the reference data, indicating that the computation method of the one-dimensional energy spectra is verified.

Figure 4.4 illustrates the comparison of the one-dimensional energy spectra between the nominal case (D700Ca40h8s8) and the base turbulent channel flow with respect to k_x and k_y in friction wall units. In figure 4.4 (*a*) and (*c*), within the near-wall region, the energy primarily present in the integral length scale is depleted and becomes more prominent in small scales. The depletion of energy is significant for all components for the one-dimensional energy spectra with respect to the streamwise wavenumber, while it is minimal for the streamwise component and substantial only for the spanwise and wall-normal components for the one-dimensional energy spectra with respect to the spanwise wavenumber. This indicates that the modulation of the intercomponent energy transfer is due to the modulation of interscale energy transfer in the spanwise direction.

The energy transported by the hairy filaments tends to concentrate towards their wake scale, bypassing the inertial subrange via spectral shortcut (Brunet *et al.*, 1994; Finnigan, 2000), resulting in the appearance of the second peak at the wake scale in the energy spectra. In figure

4.4 (*a*) and (*c*), the second peak appears around $k_x^+ \approx 0.8$ and $k_y^+ \approx 0.8$, which corresponds to the spacing of the filaments. This indicates that the wake scale depends on the spacing of the hairy filaments. The wake scale energy is then further cascading towards smaller scale eddies of the dissipative scale.

The one-dimensional energy spectra at the outer layer, present in figure 4.4 (*b*) and (*d*), show different aspects compared to at the near-wall region. The one-dimensional energy spectra at $z/H \approx 0.8$ exhibit marginal difference between the cases with and without the presence of the filaments, as shown in figure 4.4 (*b*) and (*d*). This similarity upholds the concept of the outer-layer similarity, which is a characteristic commonly observed in rough surfaces (Hama, 1954; Townsend, 1976). The hairy filaments, deemed as ’flexible’ roughness elements, have a direct impact on the flow within the near-wall region but less disturbing the outer region. It was well known that the effects of rough surface generally extend up to $2-5$ roughness heights above the roughness crests, depending on how dense these surfaces are (Raupach *et al.*, 1991; Jimenez, 2004). Above this height, the turbulence is undisturbed and recovers outer-layer similarity. This is also confirmed with the hairy surfaces regarding the similarity of the one-dimensional energy spectra, as shown in figures 4.4 (*b*) and (*d*).

In order to gain a comprehensive understanding of energy transfer, this study analyzed the pre-multiplied one-dimensional energy spectra depicted in two-dimensional contours with respect to the wavelengths and the wall-normal location. Figures 4.5 and 4.6 illustrate the two-dimensional contours of the streamwise and spanwise one-dimensional energy spectra pre-multiplied by the streamwise and spanwise wavenumbers. In this context, λ_x and λ_y denote the streamwise and spanwise wavelengths, respectively. Figure 4.5 (*a*) shows that the peak of the pre-multiplied streamwise spectra appears at $(z^+,\, \lambda_x^+) \approx (15, 1000)$ for the base turbulent channel flow. This location is often called ‘inner site’, which corresponds to the characteristic scale of elongated high- and low-speed streaks (Kline *et al.*, 1967; Hutchins & Marusic, 2007). The wall-normal location situated in the inner region corresponds to a specific location where the turbulence production is concentrated. The streamwise wavelength aligned with the inner

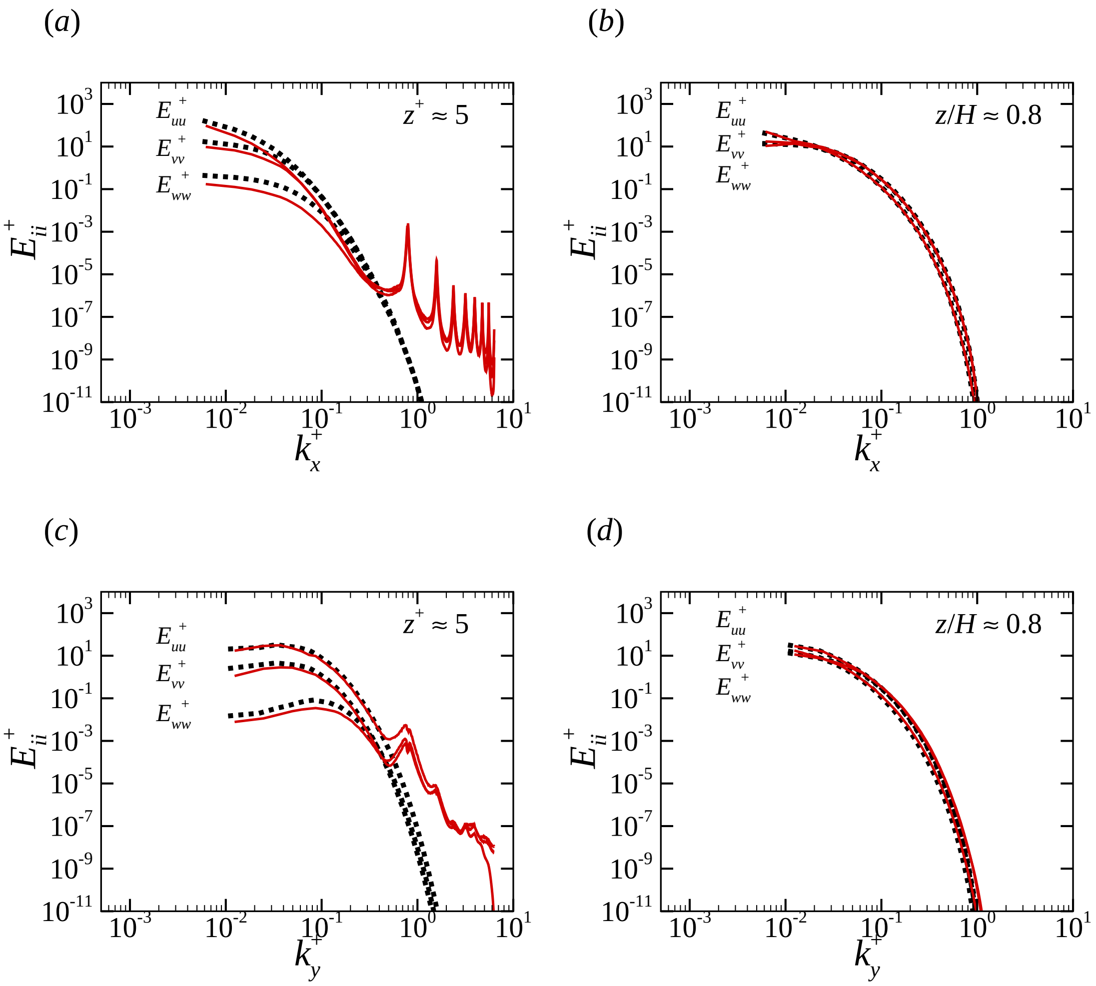

Figure 4.4: One-dimensional energy spectra for a hairy surface corresponding to the case of D700Ca40h8s8, plotted with respect to (*a*), (*b*) the streamwise wavenumber, k_x, and (*c*), (*c*) the spanwise wavenumber, k_y. The spectra is present at the wall-normal positions included in (*a*), (*c*) the near-wall region ($z^+ \approx 5$) and (*b*), (*d*) the outer-layer ($z/H \approx 0.8$). For comparison, the same quantities are plotted for the base turbulent channel flow. The red solid line (——) and black dashed line (......) denote the results from D700Ca40h8s8 and the base turbulent channel flow with no-slip, smooth walls, respectively.

site corresponds to the location where the most energetic signature of the near-wall structures appears. For the base turbulent channel flow, the peak of the spanwise one-dimensional energy spectra pre-multiplied by the spanwise wavenumber appears at $(z^+, \lambda_y^+) \approx (15, 100)$ in figure 4.6 (*a*). This viscous-scaled spanwise wavelength of 100 corresponds to the spanwise spacing of the near-wall streaks (Kline *et al.*, 1967), indicating that the most prominent energetic signature is determined by the spanwise gap of the near-wall streaks.

When hairy filaments are present, the peaks of the one-dimensional streamwise spectra pre-multiplied by the streamwise and spanwise wavenumbers, $k_x E_{u'u'}$ and $k_y E_{u'u'}$, are deviated from the inner site in figures 4.5 (*a*) and 4.6 (*a*). The z location corresponding to the peak shifts upward from that corresponding to the inner site, while λ_x^+ and λ_y^+ corresponding to the energetic signature exhibit minimal alterations from the wavelengths corresponding to the inner site. This observation suggests that the near-wall structures undergo marginal shift in the streamwise and spanwise directions but the structures notably shift towards higher z. The upward displacement of the near-wall structure is a characteristic associated with the decreased effectiveness of quasi-streamwise vortices and thus the decreased skin-friction drag (Choi *et al.*, 1993).

The contours show an expansion of the peak region for $k_x^+ E_{u'u'}^+$ and $k_y^+ E_{u'u'}^+$, but a contraction of the peak regions for the other components, as shown in figures 4.5 and 4.6. This can be attributed to the modulation of the intercomponent energy transfer by the hairy filaments. Due to the modulation of the pressure-strain correlation by the hairy filaments, the turbulence intensities is piled up in the streamwise component and reduced in the other components, as discussed in the Section 4.2. Moreover, in figures 4.5 (*a*) and 4.6 (*a*), the contours of $k_x^+ E_{u'u'}^+$ with respect to (z^+, λ_x^+) show a gradual decay, while the contours of $k_y^+ E_{u'u'}^+$ with respect to (z^+, λ_y^+) show a relatively marginal change within the near-wall region. This can be iteratively attributed to the modulation of intercomponent transfer, more prominently found in the spanwise direction.

It is worth noting that an additional peak becomes evident at $\lambda_x \approx 8$ and $\lambda_y \approx 8$, as depicted in figures 4.5 and 4.6. This observation suggests that a portion of the depleted energy is redirected towards the hairy filaments and subsequently deposited within the wake scale region through the spectral shortcut (Brunet *et al.*, 1994; Finnigan, 2000), where the wake scale corresponds to the filament spacings within the filamentous layer. Furthermore, the energy transported to the wake scale further cascades to smaller scale eddies within the filamentous layer, as evident from the gradual decay with decreasing the wavelength in the pre-multiplied energy spectra displayed in figures 4.5 and 4.6. The energy further transferred to the eddies characterized by dissipative length scales is ultimately dissipated within the viscous sublayer ($z^+ \lesssim 5$).

In conclusion, the drag reduction with hairy surfaces can be attributed to the modulation of intercomponent and interscale energy transfer. Specifically, the presence of hairy filaments leads to a decrease in the pressure-strain correlation, which causes an accumulation of turbulence intensities in the streamwise component while reducing them in the cross-streamwise components. Consequently, the energy that would have been distributed from the streamwise component to the spanwise and wall-normal components is redirected to the wake scale turbulence through the spectral shortcut, and that energy is eventually dissipated within the viscous sublayer. The resulting shear production and Reynolds shear stress associated with the v', w', and $u'w'$ then diminish, leading to a decrease in the streamwise vorticity fluctuation within the near-wall region and thus a reduction of skin-friction drag.

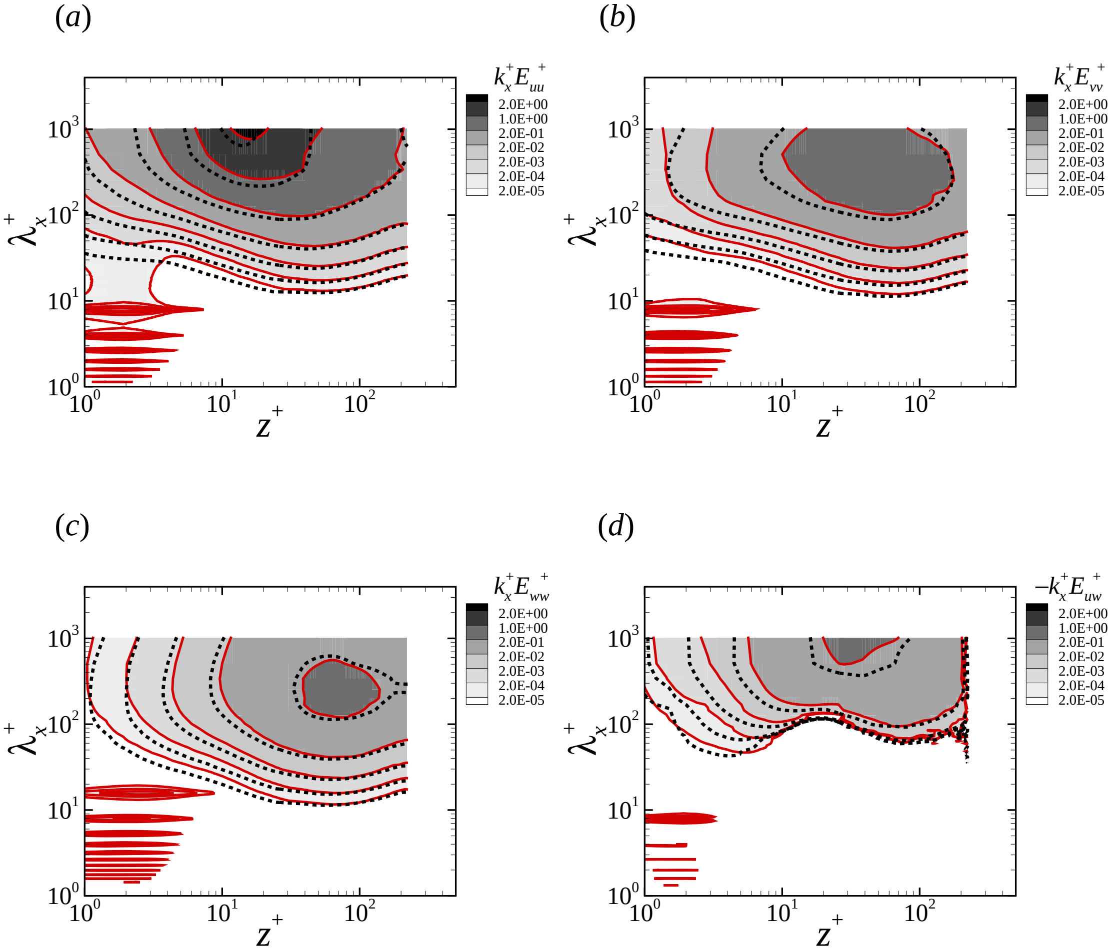

Figure 4.5: Two-dimensional contours of the pre-multiplied energy spectra for a hairy surface corresponding to the case of D700Ca40h8s8: (*a*) $k_x E_{u'u'}$, (*b*) $k_x E_{v'v'}$, (*c*) $k_x E_{w'w'}$, (*d*) $-k_x E_{u'w'}$ with respect to (z^+, λ_x). For comparison, the same quantities are plotted for the base turbulent channel flow. The red solid line (——) and black dashed line (.....) denote the results from D700Ca40h8s8 and the base turbulent channel flow with no-slip, smooth walls, respectively.

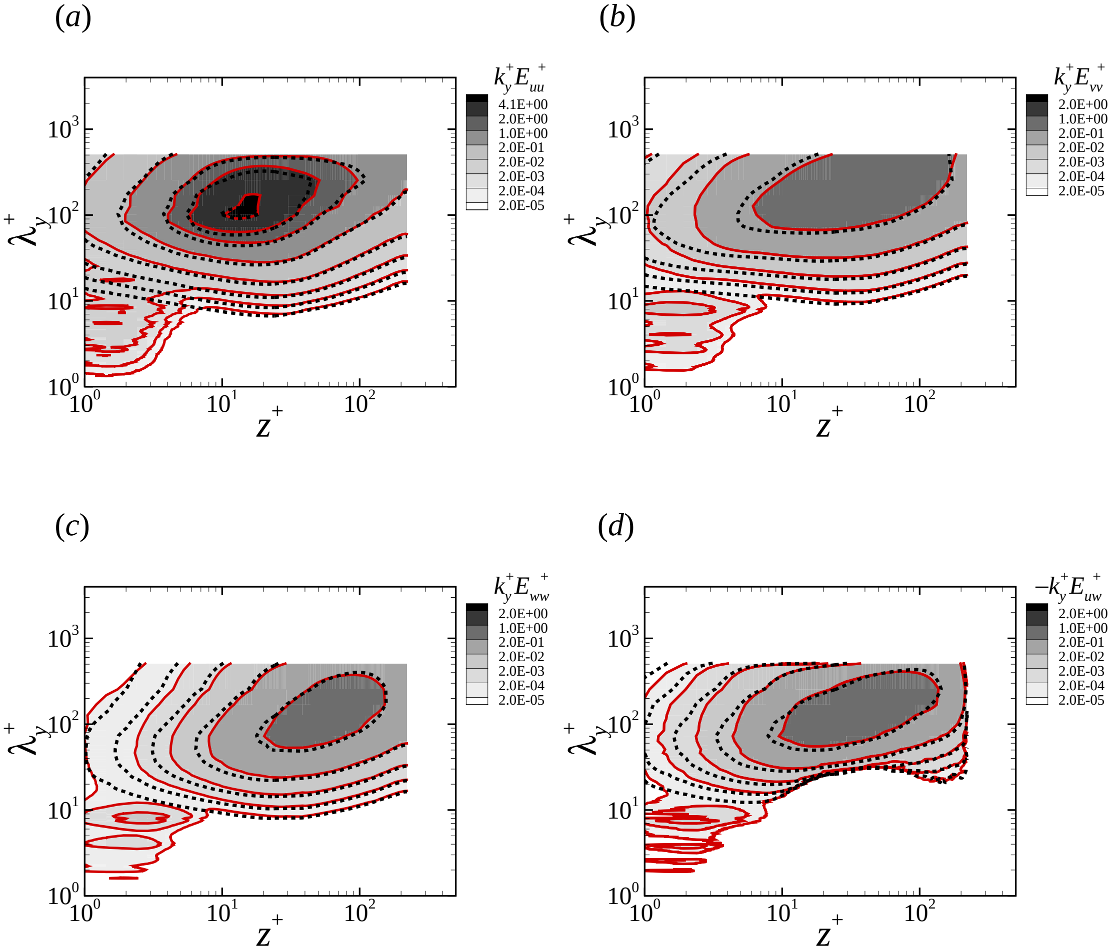

Figure 4.6: Two-dimensional contours of the pre-multiplied energy spectra for a hairy surface corresponding to the case of D700Ca40h8s8: (*a*) $k_y E_{u'u'}$, (*b*) $k_y E_{v'v'}$, (*c*) $k_y E_{w'w'}$, (*d*) $-k_y E_{u'w'}$ with respect to (z^+, λ_y). For comparison, the same quantities are plotted for the base turbulent channel flow. The red solid line (——) and black dashed line (.....) denote the results from D700Ca40h8s8 and the base turbulent channel flow with no-slip, smooth walls, respectively.

CHAPTER 5

Conclusions

5.1 Summary and Conclusions

Turbulent skin-friction drag reduction (DR) was investigated by employing direct numerical simulation (DNS) with an improved lattice Boltzmann, immersed boundary (LB-IB) method. The hairy filaments were uniformly distributed on both channel walls at bulk Reynolds number of $Re_b = 7200$, corresponding to a friction Reynolds number of $Re_\tau \approx 221$. The trend of skin-friction DR was not consistent with individual filament parameters, such as Cauchy numbers, filament height-to-spacing ratio, filament height, density ratio between the hairy filaments and fluids; however, it showed a consistent trend in terms of the characteristic time scale ratio, which was defined by the characteristic time scale of the hairy filaments to the characteristic time scale of the largest eddies in the base turbulent channel flow. DRs obtained in the parametric study collapsed into a single curve when plotted as a function of the characteristic time scale ratio. The maximum drag reduction of 5.4% was found for the characteristic time scale ratio of $1.4 - 1.5$. The resulting flow statistics at the upper near-wall region ($10 \lesssim z^+ \lesssim 30$) were consistent with the trends of DRs. The hairy filaments played a crucial role in modulating intercomponent/interscale energy transfer, leading to the skin-friction DR. In the presence of drag-reducing hairy surfaces, the energy that would have been distributed from the streamwise component to the spanwise and wall-normal components through the intercomponent transfer of turbulent energy was redirected to the filaments and transported to eddies within the wake scale via the spectral shortcut. The wake scale turbulent energy further cascades to smaller eddies of the dissipative scales and that energy was then dissipated within the viscous sublayer.

5.2 List of Achievements

- **Enhanced numerical accuracy with improved reciprocity of interpolation-spreading operations**:

  Within the framework of diffusive-direct-forcing IB scheme, a refined and rigorous approach has been proposed to improve the reciprocity of interpolation-spreading operations. This enhancement has led to significant advancements in numerical accuracy, stability, and robustness compared to previously proposed LB-IB schemes. Extensive verification and validation studies were conducted, demonstrating that the present LB-IB method maintained second-order accuracy and successfully reproduced experimental results, particularly in the case of wall-mounted flexible flaps subjected to oscillatory flow. Notably, when applied to the simulation of turbulent channel flow over hairy filaments, the present LB-IB method effectively mitigated slip-errors along the entire length of the filaments, limiting them to less than 2 percent, in stark contrast to the slip-errors on the order of $O(1000)$ observed in previous LB-IB schemes. The significant reduction in slip errors represents a notable accomplishment and demonstrates the advancements made in ensuring more accurate and reliable simulations.

- **Identification of distinct features in DR curves**:

  Distinct features were observed in the DR curves for various filament parameters. When plotting DR values against individual filament parameters such as Cauchy numbers, filament height-to-spacing ratio, filament height, and density ratio, no consistent trends were identified. However, when plotting DR values against the characteristic time scale ratio of the hairy filaments to the time scale of the largest eddies, denoted as $(T_{fil}u_\tau/H)$, DR values collapsed into a single curve. This finding suggests that the characteristic time scale ratio serves as the governing parameter for DR. The maximum DR value of approximately 5.3-5.4% was achieved at a characteristic time scale ratio of $T_{fil}u_\tau/H \approx 1.4-1.5$. These results could also provide valuable guidance for future research directions, enabling researchers to focus on investigating the influence of the characteristic time scale ratio and further exploring its implications for DR applications.

- **Physical mechanism of DR**:

  Revealing the underlying physical mechanism of DR with hairy surfaces

  This study represented a significant achievement as it successfully elucidated the underlying physical mechanism of DR with hairy surfaces. The mechanism was revealed through an investigation of the modulation of intercomponent and interscale energy transfer in the presence of hairy surfaces. Specifically, the presence of hairy filaments was found to induce a remarkable decrease in the pressure-strain correlation, resulting in an accumulation of turbulence intensity in the streamwise component while reducing them in the cross-streamwise components. This alteration in turbulence distribution had profound effects on the energy dynamics of the flow. Notably, the energy that would conventionally be distributed from the streamwise component to the spanwise and wall-normal components was redirected to the wake scale turbulence through the spectral shortcut. This redirection of energy resulted in its eventual dissipation within the viscous sublayer. As a consequence of this energy redistribution, the shear production and Reynolds shear stress associated with the cross-streamwise components (v', w', and $u'w'$) were significantly diminished. This decrease in shear production led to a notable reduction in streamwise vorticity fluctuation within the near-wall region, consequently resulting in a reduction of skin-friction drag.

  Different aspects from the mechanism of DR with rigid riblets

The most popular surface treatment for reducing skin-friction drag is deemed as using riblet surfaces to date. Riblets are small, streamwise-oriented grooves or ridges aligned with the flow direction on a surface. The key difference between the drag reduction mechanisms of riblet surfaces and hairy surfaces lies in their ability to directly transport turbulent energy. The mechanism of DR with hairy surfaces is due to intercomponent/interscale energy transfer as revealed in this study. Hairy filaments transport energy from the mean flow to turbulence and facilitate its dissipation within the viscous sublayer. The correlation of the fluctuating interaction force with the fluctuating fluid velocity, represented by the budget term of turbulent kinetic energy transport by the hairy filaments, plays a primary role in this process. This distinct mechanism makes hairy surfaces a unique and promising approach for DR in comparison to traditional riblet surfaces. The magnitude of the turbulent energy transport by rigid, stationary riblets is zero since the fluctuating velocity is zero at the riblet surfaces. Rather the mechanism of DR with riblet surfaces is related to their ability to rectify turbulent flow in the mean-flow direction by limiting cross-flow fluctuations. The net DR arises from the balance between the drag-reducing effects of streamwise slip and the drag-enhancing effects of spanwise slip (Bechert & Bartenwerfer, 1989; Luchini *et al.*, 1991; Bechert *et al.*, 1997a). The resulting quasi-streamwise vortices are lifted away from the wall, reducing their contact with the whole wall surface and weakening their effects on skin-friction generation at the wall (Bixler & Bhushan, 2013).

5.3 Suggestions for Future Research Directions

In this study, hairy surfaces with different governing parameters were applied to turbulent channel flows, and they demonstrated successful skin-friction DR. The underlying mechanism behind skin-friction DR has been elucidated. Building upon these findings, this chapter explores the potential applications of hairy surfaces in dynamically interacting with turbulent flows and provides recommendations for future research directions.

- Investigating the dynamics of hairy surfaces and their effects on skin-friction drag reduction at various Reynolds numbers can provide valuable insights into the Reynolds number dependence of drag-reducing capabilities of hairy surfaces. For example, compliant surfaces have shown varying drag-reducing capabilities with increasing Reynolds number. Fukagata *et al.* (2008) showed that an optimized compliant surface provided skin-friction drag reduction of approximately 8% at a friction Reynolds number of 110, but at higher friction Reynolds number of 180, the drag-reducing capability diminishes, and skin-friction increases (Rosti & Brandt, 2017). As Reynolds number increases, the wall compliance generates large-amplitude waves propagating downstream, leading to an increase in skin-friction drag rather than its reduction. Indeed, the observed scenario, where the drag-reducing capability diminishes with increasing Reynolds number for compliant surfaces, might also be relevant to hairy surfaces. Therefore, it becomes imperative to thoroughly investigate whether hairy surfaces retain their effectiveness at higher Reynolds numbers and their drag-reducing capability depends on Reynolds number. Such investigations will provide critical insights into the performance and suitability of hairy surfaces in various flow environments and pave the way for their practical implementation in engineering applications.

- Furthermore, in real engineering applications such as ship hulls, submarines, automobiles, and airplanes, the friction Reynolds numbers can range up to the order of $O(10^4)$ to $O(10^5)$. At these higher Reynolds numbers, the outer structures have a greater influence on skin-friction generation compared to the eddies residing in the inner layer, suggesting a promising pathway is to control the outer structures (Hutchins & Marusic, 2007; Smits *et al.*, 2011; Hwang, 2013, 2015; Marusic *et al.*, 2021). Therefore, it is conjectured that hairy surfaces may exhibit different aspects of interscale energy transfer modulation compared to the present study where Reynolds number was much lower, $Re_\tau \approx 221$.

Attenuating the characteristic time scale of the hairy filaments to the time scale of the outer structures would be a promising pathway to achieve higher DR at high Reynolds numbers.

- A hairy surface can be designed with filaments of different heights, density ratios, and Cauchy numbers. As the filaments implanted on the channel walls have different parameter values, each filament has a particular characteristic time scale different from neighbors' time scale. Then this surface would have multiple characteristic time scales rather than single characteristic time scale, allowing for disrupting a broader range of interscale transfer of turbulent energy. Moreover, the surface topology would not be uniform but uneven, gradient, or completely random so that the hairy filaments effectively interact with various length scales of turbulence. The presence of such 'multiscale' hairy surfaces could simultaneously absorb and deplete turbulent energy contained from the dissipative scale to the integral length scale, exhibiting distinct energy dynamics compared to surfaces with a single scale of uniform hairy surfaces. Then, the magnitude of skin-friction DR would be more comparable to that obtained from earlier experiments (Takata *et al.*, 1996; Itoh *et al.*, 2006). Therefore, it is worthy to explore whether the direction represented by the multiscale hairy surfaces is towards reducing or enhancing skin-friction drag.

- In this study, the probability density functions of the filament deflection in the streamwise, spanwise, and wall-normal directions showed the self-similarity feature for various filament heights while keeping the filament-spacing ratio, density ratio, and Cauchy numbers fixed. This observation suggests the possibility of formulating a mathematical model of filament deflection. For example of the spanwise filament deflection, the spanwise filament deflection could be modelled by attenuating the coefficients of a Gaussian function. As such, developing a well-established filament deflection model would greatly support predicting the behavior of real canopy elements, such as terrestrial and aquatic vegeta-

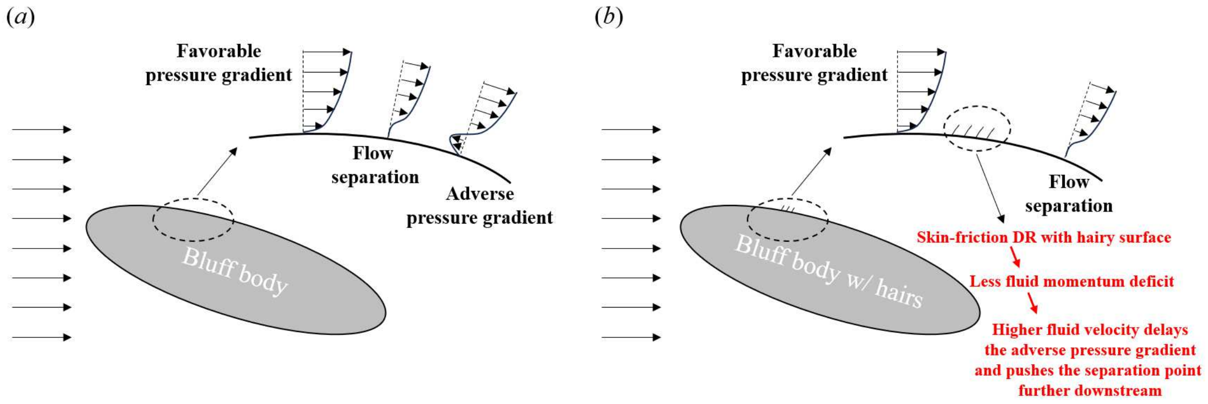

Figure 5.1: Schematics of an external flow over bluff body (*a*) without hairy surfaces and (*b*) with hairy surfaces.

tion, and their impacts on soil preservation and nutrition transport between the overlying flow and the inside the canopy, without requiring extensive numerical simulations and experiments.

- Another possible direction for future work is to investigate the performance of hairy surfaces in more complex flow configurations, beyond the channel flow considered in this study. This could involve examining the behavior of hairy surfaces in flows with curvature and its effects on the flow separation control. For instance, let us assume we have a bluff body subject to the free stream flow as shown in figure 5.1. Hairy surfaces reducing skin-friction drag can result in less fluid momentum deficit in the curved body where the flow separation would have occurred. As the fluid momentum deficit is reduced, higher fluid velocity delays the onset of the adverse pressure gradient and pushes the separation point further downstream, resulting in smaller separation region. As the separation region decreases, the pressure difference between the front and rear of the solid body could be reduced, bringing about the pressure drag reduction. Also, exploring the effects of different hairy surface configurations, such as varying filament heights, spacing ratios, and densities, could shed light on the optimal design parameters to reduce skin-friction drag as well as pressure drag.

- Apart from achieving skin-friction DRs, hairy surfaces can serve other functions in engineered applications. For example, they can be applied to airfoil surfaces found in wind turbine blades, aircraft wings, and urban/regional air mobility vehicles (UAM/RAM) to suppress separation regions and reduce aerodynamic noise. To fully explore the capabilities of hairy surfaces and their potential benefits in such engineering applications, comprehensive studies should be conducted. These studies should not only focus on skin-friction drag reduction but also simultaneously investigate other aspects such as separation control, noise reduction, their interactions, etc. By understanding the multifunctional nature of hairy surfaces and their performance in diverse engineering scenarios, the full potential of these surfaces can be harnessed to optimize the efficiency, performance, and sustainability of various engineered systems.

- The LB method does have limitations, particularly with regards to the pressure calculation. In this method, the pressure is directly computed using the equation of state, independent of the velocity fields. Consequently, there might be instances where the pressure field does not precisely correspond to the velocity field at the same time instant. Additionally, the LB method assumes an isothermal and incompressible flow, with the Mach number ideally below 0.3. However, when the flow speed exceeds a Mach number of 0.3, the standard LB method becomes inadequate and requires a suitable alternative to address this limitation. Therefore, it is essential to consider these limitations carefully when applying the LB method to specific flow scenarios and to explore alternative methods or modifications to overcome these constraints in higher-speed or compressible flow regimes.

- The hairy filaments in this study were assumed to mimic mammalian hairs (e.g., seal furs) or bird feather fibers. They were modeled as slender, elastic beams, neglecting transverse shear deformation and rotational bending. To describe the motion of these filaments, the Euler-Bernoulli beam equation was employed, as it provides a simpler solution compared to the more complicated Timoshenko–Ehrenfest beam theory. The adequacy of using the Euler-Bernoulli beam equation relies on satisfying certain assumptions made during its derivation. First, the length-to-thickness (or length-to-width) ratio of the beams should be large. Typically, the Euler-Bernoulli beam equation is valid for beams with length-to-thickness ratios greater than 10–15 (Aldraihem *et al.*, 1997). In this study, the length-to-thickness ratio of the hairy filaments ranged from 8 to 32, with filament heights of 4, 8, 10, 12, 16, and thickness of 0.5 in wall units, satisfying the criteria except for the shortest filament with a height of 4 in wall units. Another important assumption is that the beam deflection remains small enough, ensuring that the angle between the tangent to the neutral axis and the original beam axis stays small. However, the hairy filaments in this study exhibited large deflections up to approximately 90% of the filament length. This introduces challenges in identifying the governing load-deformation relations, particularly for large deflections, due to the inherent non-linearities caused by the beam's geometry, material, and the type and position of applied loading. Addressing these complexities and incorporating more accurate load-deformation relations may be necessary in future work to further understand and improve the accuracy of the model. By refining the model, a more precise representation of the hairy filaments' behavior can be achieved, enhancing the overall reliability of the simulation results.

BIBLIOGRAPHY

ADRIAN, R. J. 2007 Hairpin vortex organization in wall turbulence. *Phys. Fluids* **19**, 041301.

ALDRAIHEM, O., WETHERHOLD, R. C. & SINGH, T. 1997 Distributed control of laminated beams: Timoshenko theory vs.Euler-Bernoulli theory. *J. Intell. Mater. Syst. Struct.* **8**, 149–157.

BECHERT, D. W. & BARTENWERFER, M. 1989 The viscous flow on surfaces with longitudinal ribs. *J. Fluid Mech.* **206**, 105–129.

BECHERT, D. W., BRUSE, M. & HAGE, W. 2020 Experiments with three-dimensional riblets as an idealized model of shark skin. *Exp. Fluids* **28**, 403–412.

BECHERT, D. W., BRUSE, M., HAGE, W. & VAN DER HOEVAN, J. G. T. 1997a Experiments on drag-reducing surfaces and their optimization with adjustable geometry. *J. Fluid Mech.* **338**, 59–87.

BECHERT, D. W., BRUSE, M., HAGE, W. & MEYER, R. 1997b Biological surfaces and their technological application – laboratory and flight experiments on drag reduction and separation control. *AIAA paper no. 1997-1960* .

BENARD, N. & MOREAU, E. 2014 Electrical and mechanical characteristics of surface AC dielectric barrier discharge plasma actuators applied to airflow control. *Exp. Fluids* **55**, 1846.

BHATNAGAR, P.L., GROSS, E.P. & KROOK, M. 1954 A model for collision processes in gases. 1. Small amplitude processes in charged and neutral one-component systems. *Phys. Rev. E* **94**, 511–525.

BIXLER, G. D. & BHUSHAN, B. 2013 Shark skin inspired low-drag microstructured surfaces in closed channel flow. *J. Colloid Interface Sci.* **393**, 384–396.

BRÜCKER, C. 2011 Interaction of flexible surface hairs with near-wall turbulence. *J. Phys.: Condens. Matter* **23**, 184120.

BRÜCKER, C. & WEIDNER, C. 2014 Influence of self-adaptive hairy flaps on the stall delay of an airfoil in ramp-up motion. *J. Fluids Struct.* **47**, 31–40.

BRUNET, Y., FINNIGAN, J. J. & RAUPACH, M. R. 1994 A wind tunnel study of air flow in waving wheat: Single-point velocity statistics. *Boundary-Layer Meteorol.* **70**, 95–132.

BUICK, J. M. & GREATED, C. A. 2000 Gravity in a lattice Boltzmann model. *Phys. Rev. E* **61**, 5307.

BUSHNELL, D. M. 1998 Frontiers of the 'responsible imaginable' in (civilian) aeronautics. *The 1998 AIAA Dryden Lecture* pp. 1–20.

CECCIO, S. L. 2010 Friction Drag Reduction of External Flows with Bubble and Gas Injection. *Annu. Rev. Fluid Mech.* **42**, 183–203.

CHANDRASEKARAN, V., CAIN, A., NISHIDA, T., CATTAFESTA, L. N. & SHEPLAK, M. 2005 Dynamic calibration technique for thermal shear-stress sensors with mean flow. *Exp Fluids* **39**, 56–65.

CHECCO, A., OCKO, B. M., RAHMAN, A., BLACK, C. T., TASINKEVYCH, M., GIACOMELLO, A. & DIETRICH, S. 2014 Collapse and reversibility of the superhydrophobic state on nanotextured surfaces. *Phys. Rev. Lett.* **112(21)**, 216101.

CHEN, S. Y., WANG, Z., SHAN, X. W. & DOOLEN, G. D. 1992 Lattice Boltzmann computational fluid dynamics in three dimensions. *J. Stat. Phys.* **68**, 379–400.

CHEN, Y., YANG, J., LIU, Y. & SUNG, H.J. 2020 Heat transfer enhancement in a poiseuille channel flow by using multiple wall-mounted flexible flags. *Int. J. Heat Mass Transf.* **163**, 120447.

CHEN, Z., JIANG, C. & NEPF, H. 2013 low adjustment at the leading edge of a submerged aquatic canopy. *Water Resour. Res.* **49**, 5537–5551.

CHERNYSHOV, O. & ZAYETS, V. 1970 Some peculiarities of the structure of the skin of sharks, Hydrodynamic Problems of Bionics. *Hydrodynamic Problems of Bionics (in Russian)* **4**, 77–83.

CHO, M., HWANG, Y. & CHOI, H. 2018 Scale interactions and spectral energy transfer in turbulent channel flow. *J. Fluid Mech.* **854**, 474–504.

CHOI, H., MOIN, P. & KIM, J. 1993 Direct numerical simulation of turbulent flow over riblets. *J. Fluid Mech.* **255**, 503–509.

CHOI, H., MOIN, P. & KIM, J. 1994 Active turbulence control for drag reduction in wall-bounded flows. *J. Fluid Mech.* **262**, 75–110.

CHOI, K. S. 1989 Near-wall structure of turbulent boundary layer with riblets. *J. Fluid Mech.* **208**, 417–458.

CLARK, C. J. & JAWORSKI, J. W. 2020 Introduction to the symposium: Bio-inspiration of quiet flight of owls and other flying animals: Recent advances and unanswered questions. *Integr. Comp. Biol.* **60(5)**, 1025–1035.

CLAUSER, F. H. 1954 Turbulent boundary layers in adverse pressure gradients. *J. Aeronaut. Sci.* **21**, 91–108.

COCEAL, O., DOBRE, A., THOMAS, T. G. & BELCHER, S. E. 2007 Structure of turbulent flow over regular arrays of cubical roughness. *J. Fluid Mech.* **589**, 375–409.

DANIELLO, R. J., WATERHOUSE, N. E. & ROTHSTEIN, J. P. 2009 Drag reduction in turbulent flows over superhydrophobic surfaces. *Phys. Fluids* **21(8)**, 085103.

DEAN, R. B. 1978 Reynolds number dependence of skin friction and other bulk flow variables in two-dimensional rectangular duct flow. *Trans. ASME I: J. Fluids Engng.* **100**, 215.

DEGIOVANETTI, M., HWANG, Y. & CHOI, H. 2016 Skin-friction generation by attached eddies in turbulent channel flow. *J. Fluid Mech.* **808**, 511–538.

DIEZ, F. J. & DAHM, W. J. A. 2004 Design and fabrication of unsteady electrokinetic microactuator arrays for turbulent boundary layer control. *J. Micromech. Microeng.* **14**, 1307–1320.

DURBIN, P. A. 2023 Reflections on roughness modelling in turbulent flow. *J. Turbul.* **24**, 1–11.

EL-SAMNI, O. A., CHUN, H. H. & YOON, H. S. 2007 Drag reduction of turbulent flow over thin rectangular riblets. *Intl J. Engng Sci.* **45**, 436–454.

ENDRIKAT, S., MODESTI, D., MACDONALD, M., GARCIA-MAYORAL, R., HUTCHINS, N. & CHUNG, D. 2021 Direct Numerical Simulations of Turbulent Flow Over Various Riblet Shapes in Minimal-span channels. *Flow Turbul. Combust.* **107**, 1–29.

FANG, Z., GONG, C., REVELL, A., CHEN, G. & HARWOOD, A. 2019 Passive separation control of a NACA0012 airfoil via a flexible flap. *Phys. Fluids* **31**, 101904.

FAVIER, J., DAUPTAIN, A., BASSO, D. & BOTTARO, A. 2009 Passive separation control using a self-adaptive hairy coating. *J. Fluid Mech.* **627**, 451–483.

FAVIER, J., LI, C., KAMPS, L., REVELL, A., O'CONNOR, J. & BRÜCKER, C. 2017 The PELskin project – part I: fluid-structure interaction for a row of flexible flaps: a reference study in oscillating channel flow. *Meccanica* **52** (8), 1767–1780.

FAVIER, J., REVELL, A. & PINELLI, A. 2014 A Lattice Boltzmann–Immersed Boundary method to simulate the fluid interaction with moving and slender flexible objects. *J. Comput. Phys.* **261** (15), 145–161.

FEDLUN, E. A., VERZICCO, R., ORLANDI, P & MOHD-YUSOF, J. 2000 Combined immersed-boundary finite-difference methods for three-dimensional complex flows simulations. *J. Comput. Phys.* **161**, 35–60.

FELDER, W., DALE, G., CASH, C. & CHANG, M. 2017 Prospects for the application of practical drag reduction technologies to legacy transport aircraft. *AIAA SciTech Forum* **The** 55^{th} **AIAA Aero. Sci. Meeting, 9 - 13 January 2017, Grapevine, Texas**, 1–23.

FINNIGAN, J. 2000 Turbulence in plant canopies. *Annu. Rev. Fluid Mech.* **32**, 519–571.

FRIGO, M. & JOHNSON, S. G. 1998 FFTW: AN ADAPTIVE SOFTWARE ARCHITECTURE FOR THE FFT. *Proceedings of the 1998 IEEE International Conference on Acoustics, Speech and Signal Processing* pp. 1381–1384.

FRISCH, U., HASSLACHER, B. & Y., POMEAU 1986 Lattice-gas automata for the Navier-Stokes equation. *Phys. Rev. Lett.* **56**, 1505–1508.

FUJIMURA, M., ATSUMI, T., MAMORI, H., IWAMOTO, K., MURATA, A., MASUDA, M. & ANDO, H. 2017 Numerical simulation of drag-reducing channel flow by using bead-spring chain model. *Int. J. Heat Fluid Flow* **63**, 75–87.

FUKAGATA, K., KERN, S., CHATELAIN, P., KOUMOUTSAKOS, P. & KASAGI, N. 2008 Evolutionary optimization of an anisotropic compliant surface for turbulent friction drag reduction. *J. Turbul.* **9**, N35.

GARCIA-MAYORAL, R. & JIMENEZ, J. 2011 Hydrodynamic stability and breakdown of the viscous regime over riblets. *J. Fluid Mech.* **678**, 317–347.

GATTI, D. & QUADRIO, M 2016 Reynolds-number dependence of turbulent skin-friction drag reduction induced by spanwise forcing. *J. Fluid Mech.* **802**, 553–582.

GLOWINSKI, R., PAN, P.-W., HESLA, T.I. & JOSEPH, D.D. 1999 A distributed Lagrange multiplier/fctitious domain method for particulate flows. *Int. J. Multiphase Flow* **25**, 755–794.

GOLDSTEIN, D., HANDLER, R. & SIROVICH, L. 1993 Modeling a no-slip flow boundary with an external force field. *J. Comp. Phys.* **105**, 354–366.

GOLDSTEIN, H., POOLE, C. & SAFKO, J. 2002 Classical mechanics (3rd edition). *Pearson* .

GORB, S. N. 2009 Functional surfaces in Biology. *Springer* **1**.

GRAHAM, M. D. & FLORYAN, D. 2021 Exact coherent states and the nonlinear dynamics of wall-bounded turbulent flows. *Annu. Rev. Fluid Mech.* **53**, 227–253.

GSELL, S. & FAVIER, J. 2021 Direct-forcing immersed-boundary method: A simple correction preventing boundary slip error. *J. Comput. Phys.* **435**, 110265.

GUO, Z., ZHENG, C. & SHI, B. 2002 Discrete lattice effects on the forcing term in the lattice Boltzmann method. *Phys. Rev. E* **65** (4), 046308.

GAD-EL HAK, M. 2000 Flow Control. *Cambridge University Press* .

HAMA, F. R. 1954 Boundary-layer characteristics for smooth and rough surfaces. *Trans. SNAME* **62**, 333–358.

HAMILTON, J. M., KIM, J. & WALEFFE, F. 1995 Regeneration mechanisms of near-wall turbulence structures. *J. Fluid Mech.* **287**, 317–348.

HAN, J. & PESKIN, C. S. 2018 Spontaneous oscillation and fluid–structure. *Proc. Natl. Acad. Sci. U.S.A.* **115**, 4417–4422.

HASEGAWA, M., CHEN, Y.-C. & SAKAUE, H. 2022 Drag reduction study of a microfiber-coated cylinder. *Sci. Rep.* **66**, 15022.

HASEGAWA, M. & SAKAUE, H. 2021 Microfiber coating for drag reduction on a cylinder. *J Fluids Struct.* **103**, 103287.

HE, S., LIU, H. & SHEN, L. 2022 Simulation-based study of turbulent aquatic canopy flows with flexible stems. *J. Fluid Mech.* **947**, A33.

HE, X. Y. & LUO, L. S. 1997*a* A priori derivation of the lattice Boltzmann equation. *Phys. Rev. E* **55**, R6333.

HE, X. Y. & LUO, L. S. 1997*b* Theory of the lattice Boltzmann method: from the Boltzmann equation to the lattice Boltzmann equation. *Phys. Rev. E* **56**, 6811–6817.

HE, X. Y., ZHU, Q., LUO, L. S. & DEMBO, M. 1997 Analytic solutions of simple flows and analysis of nonslip boundary conditions for the lattice Boltzmann BGK model. *J. Stat. Phys.* **87**, 115–136.

HEFNER, J. N. 1988 Dragging down fuel costs. *Aerosp. Am.* **26**.

HUANG, W. X., SHIN, S. J. & SUNG, H. J. 2007 Simulation of flexible filaments in a uniform flow by the immersed boundary method. *J. Comput. Phys.* **226**, 2206–2228.

HUANG, W.-X. & SUNG, H. J. 2010 Three-dimensional simulation of a flapping flag in a uniform flow. *J. Fluid Mech.* **653**, 301–336.

HUTCHINS, N. & MARUSIC, I. 2007 Large-scale influences in near-wall turbulence. *Phil. Trans. R. Soc. Lond. A* **365**, 647–664.

HWANG, J. & SUNG, H. J. 2017 Influence of large-scale motions on the frictional drag in a turbulent boundary layer. *J. Fluid Mech.* **829**, 751–779.

HWANG, Y. 2013 Near-wall turbulnet fluctuations in the absence of wide outer motions. *J. Fluid Mech.* **723**, 264–288.

HWANG, Y. 2015 Statistical structure of self-sustaining attached eddies in turbulent channel flow. *J. Fluid Mech.* **767**, 254–289.

ITOH, M., TAMANO, S., IGUCHI, R., YOKOTA, K., AKINO, N., HINO, R. & KUBO, S. 2006 Turbulent drag reduction by the seal fur surface. *Phys. Fluids* **18**, 065102.

JAWORSKI, J. W. & PEAKE, N. 2013 Aerodynamic noise from a poroelastic edge with implications for the silent flight of owls. *J. Fluid Mech.* **723**, 456–479.

JEONG, J. & HUSSAIN, F. 1995 On the identification of a vortex. *J. Fluid Mech.* **285**, 69–94.

JIANG, M. & LIU, Z. 2019 A boundary thickening-based direct forcing immersed boundary method for fully resolved simulation of particle-laden flows. *J. Comput. Phys.* **390**, 203–231.

JIMENEZ, J. 2004 Turbulent flows over rough walls. *Annu. Rev. Fluid Mech.* **36**, 173–196.

JIMENEZ, J. 2018 Coherent structures in wall-bounded turbulence. *J. Fluid Mech.* **842**, P1.

JIMENEZ, J. & MOIN, P. 1991 The minimal flow unit in near-wall turbulence. *J. Fluid Mech.* **225**, 213–240.

JIMENEZ, J. & PINELLI, A. 1999 The autonomous cycle of near-wall turbulence. *J. Fluid Mech.* **389**, 335–359.

JUNG, W.-J, MANGIAVACCHI, N. & AKHAVAN, R. 1992 Suppression of turbulence in wall-bounded flows by high-frequency spanwise oscillations. *Phys. Fluids A: Fluid Dyn.* **4**, 1605–1607.

KANG, S. K. & HASSAN, Y. A. 2011 A comparative study of direct-forcing immersed boundary-lattice Boltzmann methods for stationary complex boundaries. *Int. J. Numer. Meth. Fluids* **66**, 1132–1158.

KEMPE, T. & FRÖHLICH, J. 2012 An improved immersed boundary method with direct forcing for the simulation of particle laden flows. *J. Comput. Phys.* **231**, 3663–3684.

KIM, E. & CHOI, H. 2014 Space–time characteristics of a compliant wall in a turbulent channel flow. *J. Fluid Mech.* **756**, 30–53.

KIM, H., KLINE, S. & REYNOLDS, W. 1971 The production of turbulence near a smooth wall in a turbulent boundary layer. *J. Fluid Mech.* **50(1)**, 133–160.

KIM, Y. & PESKIN, C. S. 2007 Penalty immersed boundary method for an elastic boundary with mass. *Phys. Fluids* **19**, 053103.

KLINE, S. J., REYNOLDS, W. C., SCHRAUB, F. A. & RUNSTADLER, P. W. 1967 The structure of turbulent boundary layers. *J. Fluid Mech.* **30**, 741–773.

KOLMOGOROV, A. N. 1941*a* The local structure of turbulence in incompressible viscous fluid for very large Reynolds number. *Dokl. Akad. Nauk SSSR* **30**, 209–303.

KOLMOGOROV, A. N. 1941*b* The local structure of turbulence in incompressible viscous fluid for very large Reynolds numbers. *Proc. R. Soc. Lond. A* **30**, 9–13.

KORNILOV, V. I. 2015 Current state and prospects of researches on the control of turbulent boundary layer by air blowing. *Prog. Aerosp. Sci.* **76**, 1–23.

KRAMER, M. O. 1960 Boundary-layer stabilization by distributed damping. *J. Aero. Sci.* **27(1)**, 69.

KRAMER, M. O. 1962 Boundary layer stabilization by distributed damping. *Naval Engrs J.* **74(2)**, 341–348.

KRAVCHENKO, A. G., CHOI, H. & MOIN, P. 1993 On the relation of near-wall streamwise vortices to wall skin friction in turbulent boundary layers. *Phys. Fluids* **A 5**, 3307–3309.

KRÜGER, T., KUSUMAATMAJA, H., KUZMIN, A., SHARDT, O., SILVA, G. & VIGGEN, E. 2017 The Lattice Boltzmann Method-Principles and Practice. *Springer* .

KUWATA, Y. & SUGA, K. 2016 Lattice Boltzmann direct numerical simulation of interface turbulence over porous and rough walls. *Int. J. Heat Fluid Flow* **61 (A)**, 145–157.

LADD, A. J. C. 1994 Numerical simulations of particulate suspensions via a discretized Boltzmann equation. Part 1. Theoretical foundation. *J. Fluid Mech.* **271**, 285–309.

LAGRAVA, D., MALASPINAS, O., LATT, J. & CHOPARD, B. 2012 Advances in multi-domain lattice Boltzmann grid refinement. *J. Comput. Phys.* **231** (14), 4808–4822.

LEE, J. B., PARK, S. G., KIM, B., RYU, J. & SUNG, H. J. 2017 Heat transfer enhancement by flexible flags clamped vertically in a Poiseuille channel flow. *Int. J. Heat Mass Transf.* **107**, 391–402.

LEE, J. B., PARK, S. G. & SUNG, H. J. 2018 Heat transfer enhancement by asymmetrically clamped flexible flags in a channel flow. *Int. J. Heat Mass Transf.* **116**, 1003–1015.

LEE, M. & MOSER, R. D. 2015 Direct numerical simulation of turbulent channel flow up to $Re_\tau \approx 5200$. *J. Fluid Mech.* **774**, 395–415.

LESCHZINER, M. A. 2020 Friction-drag reduction by transverse wall motion - a review. *J. Fluid Mech.* **36**, 649–663.

LI, Z., FAVIER, J., D'ORTONA, U. & PONCET, S. 2016 An immersed boundary-lattice Boltzmann method for single-and multi-component fluid flows. *J. Comput. Phys.* **304**, 424–440.

LIN, S. C., RESLER, E. L. & KANTROWITZ, A. 1955 Electrical conductivity of highly ionized argon produced by shock waves. *J. Appl. Phys.* **26**, 95–109.

LOISEAU, E., GSELL, S., NOMMICK, A., JOMARD, C., GRAS, D., CHANEZ, P., D'ORTONA, U., KODJABACHIAN, L., FAVIER, J. & VIALLAT, A. 2020 Active mucus–cilia hydrodynamic coupling drives self-organization of human bronchial epithelium. *Nat. Phys.* **16**, 1158–1164.

LUCHINI, P., MANZO, F. & POZZI, A. 1991 Resistance of a grooved surface to parallel flow and corss-flow. *J. Fluid Mech.* **228**, 87–109.

LUHAR, M. & NEPF, H. M. 2016 Wave-induceddynamicsof flexibleblades. *J Fluids Struct.* **61**, 20–41.

LUHAR, M., ROMINGER, J. & NEPF, H. 2008 Interaction between flow, transport and vegetation spatial structure. *Environ. Fluid Mech.* **8**, 423–439.

LUO, H., MITTAL, R., ZHENG, X, BIELAMOWICZ, S. A., WALSH, R. J. & HAHN, J. K. 2008 An immersed-boundary method for flow-structure interaction in biological systems with application to phonation. *J. Comput. Phys.* **227**, 9303–9332.

LUO, K., WANG, J. & CEN, K. 2007 Full-scale solutions to particle-laden flows: multidirect forcing and immersed boundary method. *Phys. Rev. E* **76**, 066709.

LUO, L. S. 1998 Unified Theory of Lattice Boltzmann Models for Nonideal Gases. *Phys. Rev. Lett.* **81**, 1618.

LUO, L. S. 2000 Theory of the lattice Boltzmann method: Lattice Boltzmann models for nonideal gases. *Phys. Rev. E* **62**, 4982.

MA, M. & HILL, R. M. 2014 Superhydrophobic surfaces. *Curr. Opin. Colloid Interface Sci.* **11(4)**, 193–202.

MA, R., GAO, Z.-H, LU, L.-S. & CHEN, S.-S. 2022 Skin-friction drag reduction by local porous uniform blowing in spatially developing compressible turbulent boundary layers. *Phys. Fluids* **34**, 125130.

MANGAVELLI, S. C., YUAN, J. & BRERETON, G. J. 2021 Effects of surface roughness topography in transient channel flows. *J. Turbul.* **22**, 434–460.

MAO, Q., ZHAO, J., LIU, Y. & SUNG, H.J. 2022 Drag reduction by a flexible hairy coating. *J. Fluid Mech.* **946**, A5.

MARTYS, N. S., SHAN, X. & CHEN, H. 1998 Evaluation of the external force term in the discrete Boltzmann equation. *Phys. Rev. E* **58**, 6855.

MARUSIC, I., CHANDRAN, D., ROUHI, A, FU, M. K., WINE, D., HOLLOWAY, B., CHUNG, D. & SMITS, A. J. 2021 An energy-efficient pathway to turbulent drag reduction. *Nat. Commun.* **12**, 12.

MARUSIC, I., MONTY, J. P., HULTMARK, M. & SMITS, A. J. 2013 On the logarithmic region in wall turbulence. *J. Fluid Mech.* **716**, R3.

MCKEON, B. J., SHARMA, A. S. & JACOBI, I. 2013 Experimental manipulation of wall turbulence: A systems approach. *Phys. Fluids* **25**, 031301.

MEI, R., SHYY, W., YU, D. & LUO, L.-S. 2000 Lattice Boltzmann method for 3-D flows with curved boundary. *J. Comp. Phys.* **161**, 680–699.

MEJIA-ALVAREZ, R. & CHRISTENSEN, K. T. 2013 Wall-parallel stereo particle-image velocimetry measurements in the roughness sublayer of turbulent flow overlying highly irregular roughness. *Phys. Fluids* **25**, 115109.

MILLIKAN, C. B. 1938 A critical discussion of turbulent fows in channels and circular tubes. *In Proc. 5th Int. Cong. Appl. Mech* pp. 386–392.

MITTAL, R., DONG, H., BOZKRUTTAS, M., NAJJAR, F. M., VARGAS, A. & VON-LOEBBECKE, A. 2008 A versatile sharp interface immersed boundary method for incompressible flows with complex boundaries. *J. Comput. Phys.* **227**, 4825–4852.

MITTAL, R. & ICCARINO, G. 2005 Immersed boundary methods. *Annu. Rev. Fluid Mech.* **37**, 239–261.

MOHD-YUSOF, J. 1997 Combined immersed boundaries/B-spline methods for simulations of flows in complex geometries. *CTR Annual Research Briefs, NASA Ames/Stanford University* pp. 317–327.

MONTI, A., OLIVIERI, S. & ROSTI, M. E. 2023 Collective dynamics of dense hairy surfaces in turbulent flow. *Sci. Rep.* **13**, 5184.

MONTI, A., OMIDYEGANEH, M., ECKHARDT, B. & PINELLI, A. 2020 On the genesis of diferent regimes in canopy flows: a numerical investigation. *J. Fluid Mech.* **891**, A9.

MONTI, A., OMIDYEGANEH, M. & PINELLI, A. 2019 Large-eddy simulation of an open-channel flow bounded by a semi-dense rigid filamentous canopy: Scaling and flow structure. *Phys. Fluids* **31**, 065108.

MOOSAIE, A. & MANHART, M. 2016 On the pressure-strain correlation in fibrous drag-reduced turbulent channel flow. *Phys. Fluids* **28**, 025101.

NEPF, H. M. 2012 Flow and transport in regions with aquatic vegetation. *Annu. Rev. Fluid Mech.* **44**, 123–142.

O'CONNOR, J. & REVELL, A. 2019 Dynamic interactions of multiple wall-mounted flexible flaps. *J. Fluid Mech.* **870**, 189–216.

OIKAWA, S. & MENG, Y. 1995 Turbulence characteristics and organized motion in a suburban roughness sublayer. *Bound.-Layer Meteorol.* **74**, 289–312.

ORLANDI, P. & JIMENEZ, J. 1994 On the generation of turbulent wall friction. *Phys. Fluids* **6**, 634–641.

PARK, H., SUN, G. & KIM, C. J. 2014 Superhydrophobic turbulent drag reduction as a function of surface grating parameters. *J. Fluid Mech.* **747**, 722–734.

PARK, S. G., KIM, B., RYU, J., CHANG, C. B. & SUNG, H.J. 2016 Enhancement of heat transfer by a self-oscillating inverted flag in a Poiseuille channel flow. *Int. J. Heat Mass Transf.* **96**, 362–370.

PESKIN, C. 1977 Numerical analysis of blood flow in the heart. *J. Comput. Phys.* **25**, 220–252.

PESKIN, C. S. 1972 Flow patterns around heart valves: a numerical method. *J. Comput. Phys.* **10**, 252–271.

PESKIN, C. S. 2002 The immersed boundary method. *Acta Numer.* **11**, 479–517.

PINELLI, A., NAQAVI, I. Z., PIOMELLI, U. & FAVIER, J. 2010 Immersed-boundary methods for general finite-difference and finite-volume Navier-Stokes solvers. *J. Comput. Phys.* **229**, 9073–9091.

POPE, S. B. 2000 Turbulent Flows. *Cambridge university press* .

RASTEGARI, A. & AKHAVAN, R. 2018 The common mechanism of turbulent skin-friction drag reduction with superhydrophobic longitudinal microgrooves and riblets. *J. Fluid Mech.* **838**, 68–104.

RATHNASINGHAM, R. & BREUER, K. S. 2003 Active control of turbulent boundary layers. *J. Fluid Mech.* **495**, 209–233.

RAUPACH, M. R. 1992 Drag and drag partition on rough surfaces. *Boundary-Layer Meteorol.* **60**, 375–395.

RAUPACH, M. R., ANTONIA, R. A. & RAJAGOPALAN, S. 1991 Rough-Wall Turbulent Boundary Layers. *Appl. Mech. Rev.* **44(1)**, 1–25.

RAUPACH, M. R., FINNIGAN, J. & BRUNET, Y. 1996 Coherent eddies and turbulence in vegetation canopies: The mixing-layer analogy. *Boundary-Layer Meteorol.* **78**, 79–90.

REDDY, N. & YANG, Y. 2007 Structure and properties of chicken feather barbs as natural protein fibers. *J Polym Environ* . **15**, 81–87.

RICCO, P., SKOTE, M. & LESCHZINER, M. A. 2021 A review of turbulent skin-friction drag reduction by near-wall transverse forcing. *Prog. Aerosp. Sci.* **123**, 100713.

ROBINSON, S. K. 1991 Coherent motions in the turbulent boundary layer. *Annu. Rev. Fluid Mech.* **23**, 601–639.

ROMA, A. M., PESKIN, C. S. & BERGER, M. J. 1999 An Adaptive version of the immersed boundary method. *J. Comput. Phys.* **153**, 509–534.

ROSTI, M. E. & BRANDT, L. 2017 Numerical simulation of turbulent channel flow over a viscous hyper-elastic wall. *J. Fluid Mech.* **830**, 708–735.

ROSTI, M. E. & BRANDT, L. 2020 Low Reynolds number turbulent flows over elastic walls. *Phys. Fluids* **32(8)**, 083109.

ROSTI, M. E., BRANT, L. & PINELLI, A. 2018 Turbulent channel flow over an anisotropic porous wall – drag increase and reduction. *J. Fluid Mech.* **842**, 381–394.

ROSTI, M. E., CORTELEZZI, L. & QUADRIO, M. 2015 Direct numerical simulation of turbulent channel flow over porous walls. *J. Fluid Mech.* **784**, 396–442.

RYU, J., PARK, S. G., KIM, B. & SUNG, H.J. 2015 Flapping dynamics of an inverted flag in a uniform flow. *J. Fluids Struct.* **57**, 159–169.

SAIKI, E. M. & BIRINGEN, S. 1996 Numerical simulation of a cylinder in uniform flow: Application of a virtual boundary method. *J. Comput. Phys.* **123**, 450–465.

SAMAHA, M. A., TAFRESHI, H. V. & GAD-EL HAK, M. 2012 Influence of Flow on Longevity of Superhydrophobic Coatings. *Langmuir* **28(25)**, 9759–9766.

GOMEZ-DE SEGURA, G. & GARCIA-MAYORAL, R. 2019 Turbulent drag reduction by anisotropic permeable substrates – analysis and direct numerical simulations. *J. Fluid Mech.* **875**, 124–172.

SEO, J. & MITTAL, R. 2011 A high-order immersed boundary method for acoustic wave scattering and low-Mach number flow-induced sound in complex geometries. *J. Comput. Phys.* **230**, 1000–1019.

SHAN, H., JIANG, L., LIU, C., LOVE, M. & MAINES, B. 2000 Numerical study of passive and active flow separation control over a NACA0012 airfoil. *Comput. Fluids* **37**, 975–992.

SHAN, X. & HE, X. 1998 Discretization of the velocity space in the solution of the Boltzmann equation. *Phys. Rev. Lett.* **80**, 65–68.

SHAN, X., YUAN, X. & CHEN, H. 2006 Kinetic theory representation of hydrodynamics: a way beyond the Navier–Stokes equation. *J. Fluid Mech.* **550**, 413–441.

SHAO, Y. & YANG, Y. 2005 A scheme for drag partition over rough surfaces. *Atmos. Environ.* **39**, 7351–7361.

SHARMA, A. & GARCIA-MAYORAL, R. 2020*a* Scaling and dynamics of turbulence over sparse canopies. *J. Fluid Mech.* **888**, A1.

SHARMA, A. & GARCIA-MAYORAL, R. 2020*b* Turbulent flows over dense filament canopies. *J. Fluid Mech.* **888**, A2.

SHIN, S. J., HUANG, W.-X. & SUNG, H. J. 2008 Assessment of regularized delta functions and feedback forcing schemes for an immersed boundary method. *Int. J. Numer. Meth. Fluids* **58**, 263–286.

SHOELE, K. & MITTAL, R. 2016 Energy harvesting by flow-induced flutter in a simple model of an inverted piezoelectric flag. *J. Fluid Mech.* **790**, 582–606.

SMITH, J. R. & METZLER, S. P. 1983 The characteristics of low-speed streaks in the near-wall region of a turbulent boundary layer. *J. Fluid Mech.* **129**, 27–54.

SMITS, A. J., MCKEON, B. J. & MARUSIC, I. 2011 High–Reynolds number wall turbulence. *Annu. Rev. Fluid Mech.* **43**, 353–375.

SPALART, P. R. & MCLEAN, J. D. 2011 Drag reduction: enticing turbulence, and then an industry. *Phil. Trans. R. Soc. Lond. A* **369**, 1556–1569.

STOCKIE, J. M. 1997 Analysis and computation of immersed boundaries, with application to pulp fibres. *PhD thesis, The University of British Columbia (Canada)* .

SUNDIN, J. & BAGHERI, S. 2019 Interaction between hairy surfaces and turbulence for different surface time scales. *J. Fluid Mech.* **861**, 556–584.

TAKATA, T., KYOGOKU, K. & NAKAHARA, T. 1996 Turbulent drag reduction: Effect of implanted fiber. *Trans. Jpn. Soc. Mech. Eng. B* **62**, 1383–1387.

TAO, J. & YO, X. B. 2012 Hair flow sensors: from bio-inspiration to bio-mimicking – a review. *Smart Mater. Struct* **21(11)**, 113001.

TENNEKES, H. & LUMLEY, J. L. 1972 A First Course in Turbulence. *The MIT press* .

TESFAYE, T., SITHOLE, B. & RAMJUGERNATH, D. 2018 Valorisation of chicken feather barbs: Utilisation in yarn production and technical textile applications. *Sustain. Chem. Pharm.* **8**, 38–49.

TIAN, F. B., LUO, H., ZHU, L, LIAO, J. C. & LU, X. Y 2011 An efficient immersed boundary-lattice Boltzmann method for the hydrodynamic interaction of elastic filaments. *J. Comput. Phys.* **230**, 7266–7283.

TOLOUI, M., ABRAHAM, A. & HONG, J. 2019 Experimental investigation of turbulent flow over surfaces of rigid and flexible roughness. *Exp. Therm. Fluid Sci.* **101**, 263–275.

TOMKINS, C. D. & ADRIAN, R. J. 2003 Spanwise structure and scale growth in turbulent boundary layers. *J. Fluid Mech.* **490**, 37–74.

TOMS, B. Q. 1949 Some observations on the flow of linear ploymer solutions through straight tubes at large Reynolds numbers. *In Proc. 1st Int. Congress on Rheology* **2**, 135–141.

TOWNSEND, A. 1976 The Structure of Turbulent Shear Flow. *Cambridge University Press* .

TRETHEWAY, D. C. & MEINHART, C. D. 2002 Apparent fluid slip at hydrophobic microchannel walls. *Phys. Fluids* **14**, L9.

TSCHISGALE, S., LÖHRER, B., MELLER, R. & FROÖHLICH, J. 2021 Large eddy simulation of the fluid-structure interaction in an abstracted aquatic canopy consisting of flexible blades. *J. Fluid Mech.* **916**, A43.

UHLMANN, M. 2005 An immersed boundary method with direct forcing for the simulation of particulate flows. *J. Comput. Phys.* **209**, 448–476.

UMAIR, M., TARDU, S. & DOCHE, O. 2022 Reynolds stresses transport in a turbulent channel flow subjected to streamwise traveling waves. *Phys. Rev. Fluids* **7**, 054601.

VUKOSLAVCEVIC, P., WALLACE, J. M. & BALINT, J. L. 1992 Viscous drag reduction using streamwise-aligned riblets. *AIAA J.* **30**, 1119–1122.

WALEFFE, F. 1997 On a self-sustaining process in shear flows. *Phys. Fluids* **9**, 883–900.

WALSH, M. J. 1982 Turbulent boundary layer drag reduction using riblets. *AIAA paper* pp. 82–0169.

WALSH, M. J. & LINDEMANN, A. M. 1984 Optimization and application of riblets for turbulent drag reduction. *AIAA paper* pp. 84–0347.

WU, J. & SHU, C. 2009 Implicit velocity correction-based immersed boundary-lattice Boltzmann method and its applications. *J. Comput. Phys.* **228**, 196–1979.

XIA, Q. J., HUANG, W. X. & XU, C. X. 2019 Direct numerical simulation of a turbulent boundary layer over an anisotropic compliant wall. *Acta Mech. Sin.* **35 (2)**, 384–400.

XU, C.-X. & HUANG, W.-X. 2004 Transient response of Reynolds stress transport to spanwise wall oscillation in a turbulent channel flow. *Phys. Fluids* **17**, 018101.

YANG, J., PREIDIKMAN, S. & BALARAS, E. 2008 A strongly coupled, embedded-boundary method for fluid-structure interactions of elastically mounted rigid bodies. *J. Fluids Struct.* **24**, 167–182.

YANG, J. & STERN, F. 2015 Non-iterative direct forcing immersed boundary method for strongly-coupled fluid-solid interactions. *J. Comput. Phys.* **295**, 779–804.

ZHENG, Q.-S., YU, Y. & ZHAO, Z.-H. 2009 Effects of hydraulic pressure on the stability and transition of wetting modes of superhydrophobic surfaces. *Langmuir* **21(26)**, 12207–12212.

ZHOU, J., ADRIAN, R. J., BALACHANDAR, S. & KENDALL, T. M. 1999 Mechanisms for generating coherent packets of hairpin vortices in channel flow. *J. Fluid Mech* **387**, 353–396.